Lagrangian description for the drift of large floating debris in rivers during floods

A Master's Thesis Submitted by

Damien Sansen

for the Department of Hydraulics in Environmental and Civil Engineering

as part requirement for the Master's degree "Engineering physics"

Advisor
Pr. B. Dewals (ULiège)
Co-advisor
C. Delhez (ULiège)

Jury
Pr. P. Archambeau (ULiège)
Pr. S. Erpicum (ULiège)
Pr. T. Gilet (ULiège)

University of Liège
Faculty of applied Sciences
Academic year 2022-2023

Remerciements

Je tiens à exprimer ma profonde gratitude envers toutes les personnes qui m'ont accompagné et soutenu tout au long de ce mémoire.

Tout d'abord, je souhaite remercier chaleureusement le Pr. Dewals pour m'avoir donné l'opportunité de travailler sur ce sujet. Son soutien, sa considération et sa disponibilité ont été d'une aide précieuse tout au long de cette aventure.

Je suis également reconnaissant envers Clément pour son précieux aiguillage qui aura contribué à la réussite de ce mémoire. Je tiens notamment à souligner sa patience et son écoute pour les débats répétitifs qui ont ponctué l'élaboration de ce travail.

Je souhaite exprimer ma profonde gratitude envers ma maman et Patrick pour leur soutien indéfectible tout au long de cette dernière étape de mon parcours, ainsi que durant l'intégralité de mes études. Leur présence constante, leurs encouragements inébranlables et leur attention soutenue ont été une source de motivation inestimable pour laquelle je leur suis infiniment reconnaissant.

Mes remerciements s'addressent également à Jérôme, à qui je suis extrêmement reconnaissant d'avoir eu la patience et la compréhension dont il a fait preuve.

Enfin, je tiens à mentionner Zakaria, ainsi que Tom et William, dont l'esprit collectif n'a fait qu'accroitre ma motivation.

Merci à vous tous et bonne lecture!

Abstract

This Master's Thesis presents a two-dimensionnal Lagrangian model of the drift of floating objects on rivers during flood events. Particular attention is paid to the prediction of bridge obstruction by such debris. It comprises three parts: (1) a literature review aiming to list relevant previous work, thus establishing the existing theoretical bases and identifying research areas in need of further investigation; (2) the development of the model used in this thesis, comprising a dynamic model and a collision model; (3) a validation stage with the aim of reproducing simulations and experiments from the literature, and also simulating real flows.

The literature review identified two main categories of model, one focusing on the fundamental dynamics of the floating object, the other on real-life applications. These two trends can also be distinguished in collision models. However, the literature provides neither obstacle nor detection models. On the other hand, the corrections to be made are often detailed.

A dynamic model and a collision model have been developed. The dynamic model is inspired by the literature, while the collision model is innovative in terms of obstacle representation and detection. In particular, the model consists of a rectangular representation of the obstacle. This enables a systematic study of the different types of collisions and detections existing on such a shape. An implementation has been carried out to model a single floating cylinder.

Two phases of simulations of floating cylinders were launched. The first was carried out under hypothetical flow conditions, to verify the basic cases of cylinder behavior. As for collisions, the typical cases identified by the model were verified, as well as more complex cases of multiple and simultaneous collisions. The model was then validated by comparison with results from the literature, and the simulation of collisions was tested on cases from the laboratory.

The study focused on predicting channel obstruction by blocking the cylinder between various obstacles. Experiments showed that the code was capable of such predictions, in a variety of situations. In addition to permanent obstructions, temporary obstructions were also observed in many configurations.

Finally, the limitations of both the model and the code were analyzed, and prospects for future work were proposed.

Résumé

Cette thèse de master propose un modèle Lagrangien bidimensionel de la dérive d'objets flottants sur des rivières durant des épisodes d'inondations. Une attention particulière est portée sur la prédiction d'obstruction de pont par ces débris. Elle comprend trois parties : (1) une revue de la littérature visant à recenser les travaux antérieurs pertinents, établissant ainsi les bases théoriques existantes et identifiant les lacunes de recherche à approfondir ; (2) le développement du modèle utilisé dans cette thèse, comprenant un modèle dynamique et un modèle de collision ; (3) une étape de validation ayant pour but de reproduire des simulations et expériences de la littérature et aussi de simuler des écoulements réels.

La revue de la littérature a identifié deux grandes familles de modèles, l'une proposant un modèle plus axé sur la dynamique fondamentale de l'objet flottant et l'autre plus axée sur une application en cas réel. Ces deux courants se distinguent aussi dans les modèles de collisions. Cependant, la littérature ne fournit ni modèle d'obstacle, ni modèle de détection. En revanche, les corrections à apporter sont souvent détaillées.

Un modèle dynamique et un modèle de collision ont ainsi été développés. Le modèle dynamique s'inspire de la littérature tandis que le modèle de collision est innovant en termes de représentation d'obstacles et de détection. En particulier, le modèle consiste en une représentation rectangulaire de l'obstacle. Cela permet une étude systématique de différents types de collisions et détections existantes sur une telle forme. Une implémentation a été menée, visant la modélisation d'un unique cylindre flottant.

Deux phases de simulations de cylindres flottants ont été lancées. Une première sous un écoulement hypothétique, permettant de vérifier les cas de base quant au comportement du cylindre. Quant aux collisions, les cas types identifiés par le modèle ont été vérifiés ainsi que des cas plus complexes de collisions multiples et simultanées. Ensuite, une confrontation avec les résultats de la littérature a permis de valider le modèle et de tester la simulation de collisions sur des cas de la laboratoires.

L'étude a été axée sur la prévision d'obstruction du canal par blocage du cylindre entre divers obstacles. Les résultats ontdémontré la capacité du code à prédire ce phénomène et ce, dans des situations variées. Outre des obstructions permanentes, des obstructions temporaires ont été remarquées dans diverses configurations.

Enfin, les limites du modèle ainsi que du code ont été analysées et des perspectives pour de futurs travaux ont été proposées.

Contents

List of Figures

List of Tables

Nomenclature

Acronyms

BBO	Basset–Boussinesq–Oseen
LW	large wood
RK22	Runge-Kutta order 2, 2 iterations

Indices

$\parallel$	tangential
$\perp$	perpendicular
am	added mass
c	cylinder
CM	center of mass
CP	center of pressure
d	drag
f	friction
g	gravity
n	subpart of the body
s	side
tot	total / resulting
w	water

Mathematical convention

$\cdot$	scalar product
$\hat{\mathbf{e}}$	unit vector
$\hat{\mathbf{n}}$	normal unit vector
$\times$	cross product
$\mathbf{q}$	vector quantity q
q	scalar quantity q

Physical quantities

α	angle of the channel bed with the direction of the channel	[°]
β	incidence angle of collision	[°]
ϵ	coefficient of restitution	[−]
η	dynamic viscosity	[kg/ms]
λ	wavelength	[m]
$\mathbf{a}$	acceleration	[m/s^2]
$\mathbf{F}$	force	[N]
$\mathbf{g}$	gravitational acceleration	[m/s^2]
$\mathbf{u}$	flow velocity	[m/s]
$\mathbf{v}$	debris velocity	[m/s]
ω	angular velocity	[°/s]
ρ	density	[kg/m^3]
θ_{uv}	angle between the cylinder's major axis and the flow velocity	[°]
θ_x	angle between the cylinder's major axis and the x-axis	[°]
C	coefficient	[−]
d	diameter	[m]
Fr	Froude number	[−]
h	water depth	[m]
I	momentum of inertia	[kgm^2]
J	Impulse momentum	[kgm/s]
l	length	[m]
N	Number of sub-parts of the cylinder	[−]
p	pressure	[Pa]
Re	Reynolds number	[−]
Re$_p$	particulate Reynold number	[−]
S$_p$	projection of cross-area of the trunk in the flow direction	[m^2]

Introduction

The World Meteorological Organization, a United Nations agency specialized in meteorology, recognizes floods as one of the most serious threats posed by natural disasters that affect many regions of the world every year. In recent decades, flood damage has increased at an exponentially alarming rate. This trend can be attributed to the increasing frequency of intense precipitation events, changes in upstream land use practices, and the steady increase in the population and valuable assets moving into flood-prone areas. Around 85% of floods are caused by flash floods, and they are also responsible for the highest mortality rate. They are among the world's deadliest natural disasters, causing over 5,000 deaths every year. In addition, inadequate flood planning and management practices often exacerbate these dangerous situations (World Meteorological Organization (WMO), 2023).

This is no exception in Western countries such as Belgium. Indeed, Kundzewicz et al. (2010) demonstrate a rapid increase in flood risks worldwide and in Europe in recent years. This escalation is mainly due to climate change. In the city of Liege (Belgium), there is a significant flood risk projected for the time horizon 2100. This risk is primarily attributed to the anticipated high values of future flood discharges, which are estimated to be approximately 30% higher compared to the current climate conditions (Dewals et al., 2015).

A particularly common phenomenon during floods is the drifting of floating debris. They often have the potential to create blockages in certain areas, particularly where it accumulates between bridge piers and obstructs river flow. This phenomenon can cause a localized alteration in flow velocity, resulting in erosion and additional damages. Moreover, if the condition for the collapse of the jam exists, the phenomenon can evolve into a dam break flow that results in an increase in downstream discharge (Macchione and Lombardo, 2021).

Flooding is an integral part of the natural river cycle. Consequently, flood management and prediction play a crucial role in protecting people and infrastructure from these devastating events.

Flood risk maps are crucial for flood risk prevention, but there is a need to take into account the additional risks and damage caused by clogging. Consequently, there is a growing need to enhance predictions of floating object behavior and the risk of bridge obstruction. Although numerical models of floating debris behavior exist for laboratory situations, they have not yet been tested on real cases, and the study of obstructions on bridges remains unclear.

The primary objective of this master's thesis is to enhance the comprehension of the movement of a floating debris (like a tree trunk) in a river in flood conditions. The ultimate aim is to develop an original two-dimensional numerical model of the dynamics of these objects. In particular, this model should be able to handle debris-structure collisions and thus predict bridge obstructions. The addition of physical parameters describing a terrain model should make it possible to approach more realistic scenarios than those found in laboratories. This algorithm could then be used to systematically study the behavior of floating debris.

This work is structured in 3 parts. In the first one, a literature review provides an overview of existing physical models. The second part deals with the model adopted for the algorithm. A confrontation with the established literature is then be discussed in Part 3.

Part I
State of the art

The motivation behind this section is to conduct a thorough review of existing literature on the physics of floating debris in order to provide a comprehensive understanding of the subject. In particular, this section is divied into two parts : a first one which strictly compares the framework of the different articles, and a second one that reviews the various mathematical and physical models of the problem.

1 General overview

In order to carry out a comparison of the literature articles most in agreement with this thesis of mater, tables are presented with the following convention :

■ the criterion is covered in the article;

the criterion is not covered in the article at all.

The reference articles chosen are the following. The indicated citation numbers are provided by Scopus.

- ▷ (Ghaffarian et al., 2020), cited 3 times
- ▷ (Ruiz-Villanueva et al., 2014), cited 104 times
- ▷ (Persi, 2015), cited 32 times

They were selected among others because they offer a representative study of floating debris: namely, the development of an analytical model, followed by a numerical implementation phase and experimental validation. In this work, these articles are referred to as 'reference articles' hereafter. However, other articles are referenced as complements.

(Ghaffarian et al., 2020) represents a study of floating spheres while the other study cylinders. Moreover, a dichotomy emerges between two distinct groups of models for floating debris. The first group involves models developed within the framework of (Yin et al., 2003) and (Mandø and Rosendahl, 2010), which are then subjected to simulation and laboratory experimentation by (Persi, 2015). In contrast, the second group centers around models established by (Haga et al., 2002) and (Magnaudet and Eames, 2000), followed by their simulation and laboratory examination by (Ruiz-Villanueva et al., 2014). As the two articles chosen reproduce the models as they stand from these latter articles, the tables enable a short and effective comparison of the two main models.

1.1 Flow hypothesis comparison

The columns represent:

- ▷ Turbulence model: presence or absence of a turbulence model;
- ▷ Unsteady: variation of fluid velocity with time;
- ▷ Uniform: no spatial dependence of the velocity field;
- ▷ Field: consideration of real-life situations in the simulations.

Models \ Flow hypothesis	Turbulence model	Unsteady	Field
Ghaffarian et al. (2020)			
Ruiz-Villanueva et al. (2014)			
Persi et al. (2017)			

Table 1: Flow hypothesis comparison.

1.2 Flumes comparison

A attention must be paid to the different channels used. As the channels not only condition the type of flow, but also imply additional physical phenomena such as collisions or clogging, it is therefore important to develop a numerical model for the study of clogging at bridge piers.

A schematic representation of the used channels is shown in Fig.(1). Few articles study clogging phenomena numerically. In fact only (Ruiz-Villanueva et al., 2014) provides two circular bridge pillars to explicitly study clogging and rising water levels upstream, in both experimental and numerical ways.

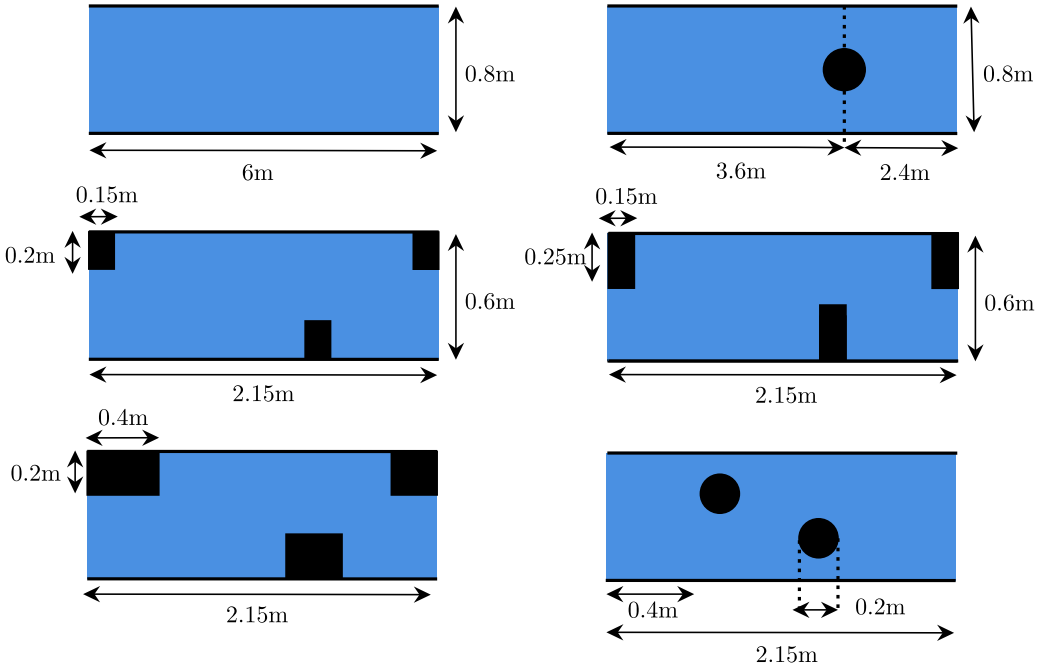

Figure 1: Schematic representation of the different flume configurations (not at scale, top view) and obstacles used in Ghaffarian et al. (2020), Ruiz-Villanueva et al. (2014) and Persi et al. (2017).

1.3 Type of floating debris comparisons

When it comes to large floating debris appearing on the ground during flooding events, the shapes vary from simple pieces of wood to cars and furniture. When it comes to modeling these objects, assumptions are made on their shape. These are fairly recurrent and similar between articles. Tab.(2) shows a comparison of the various drifting shapes studied.

Drifting shape / Models	Sphere		Disk		Cylinder	
Type of study	**num**	**exp**	**num**	**exp**	**num**	**exp**
Ghaffarian et al. (2020)	■			■		■
Ruiz-Villanueva et al. (2014)					■	■
Persi et al. (2017)	■	■			■	

Table 2: Drifting shapes studied numerically (noted *num*) and experimentally (noted *exp*).

First of all, it should be noted that the typical debris numerically and experimentally studied consists of an asymmetrical object, such as a cylinder. The use of this shape as a reference debris offers practical advantages in terms of understanding and comparability for the physical and numerical study of floating debris. Theoretically, it is a simple geometry that allows the study of their behavior analytically. Experimentally, it is a shape that can be easily reproduced Persi (2015).

In addition, the latter cylindrical shape is often referenced as large wooden debris, abbreviated LW, when it is longer than 1 [m] and with a diameter larger than 0.1 [m]. In other oterms, when its aspect ratio higher than 10. This convention appears for the first time in the article Keller and Swanson (1979) and is repeated implicitly in the articles that follow.

2 Existing mathematical model

This subsection of the literary review focuses on the physical and mathematical models used in the literature. This is where the physical problem of large floating objects is posed, by listing and defining the various physical aspects to be taken into account. The model used in this master's thesis is justified by the study of this subsection, and is presented in Part II called 'Existing mathematical model'.

2.1 Survey of the mathematical models

First, a general comparison table is given in Tab.(3), and in the following sections, the criteria are defined in more detail. Afterwards, the entrainment and the dynamics are briefly detailed. The columns correspond to:

- ▷ Rotation: whether the yaw rotation of the object is taken into account or not;
- ▷ Collisions: collisions between different objects;
- ▷ Clogging: prediction of dam formation;
- ▷ Added mass: added mass term has added to the equations;
- ▷ Density cases: whether different density cases have been treated (fully/partially submerged);
- ▷ Turbulence model[1]: a model of turbulence;
- ▷ Entrainment: the entrainment of a tree trunk (typical debris) initially hanging or present on the ground.

[1] Even if Tab.(1) already took a turbulence model comparison into account, this criterion is again taken into account here, to provide a general summary of the physics taken into account.

Articles \ Phenomena	Entrainment	Rotation	Collisions	Clogging	Added mass	Density cases	Turbulence model
Ghaffarian et al. (2020)							
Ruiz-Villanueva et al. (2014)							
Persi et al. (2017)							

Table 3: Physical aspects taken into account.

The entrainment study

In Tab.(3), the only article dealing with tree trunk entrainment is Persi et al. (2017). It is important to know under what conditions a tree trunk, initially at rest, is carried away by a flow. Into more details, the article follows the conclusion of two others :Bocchiola et al. (2006) and Braudrick (2000) which are summarized below.

The transport of solid entities is affected by various factors, such as their properties, dimensions, and orientation, particularly for asymmetric entities (Bocchiola et al., 2006). When the water level allows for buoyancy, wooden rigid bodies begin to float (Braudrick, 2000). Entrainment can occur through three primary mechanisms: flotation, rolling, and sliding. Flotation arises when the upward force exceeds the body's weight, while rolling and sliding manifest when the body is not fully buoyant. Specifically, elongated bodies begin to roll when perpendicular to the flow, whereas sliding happens when rotation is restricted, such as with flow-aligned cylinders.

Survey on the dynamic

As in the previous sections, a very general overview of the dynamics dealt with in the articles is offered as an introduction. The various models are then described in detail. To begin with, the definitions of global and local frames need to be clarified. The global reference frame is defined as the $(\mathbf{e}_x, \mathbf{e}_y)$ frame fixed to the channel. It belongs to the so-called horizontal plane. The local reference frame is denoted as $(\mathbf{e}_{x'}, \mathbf{e}_{y'})$. It is fixed to the object and $\mathbf{e}_{x'}$ is aligned with the relative velocity while $\mathbf{e}_{y'}$ is perpendicular to it These definitions are common to every used articles and are represented in Fig.(2), with a cylinder as the drifting shape.

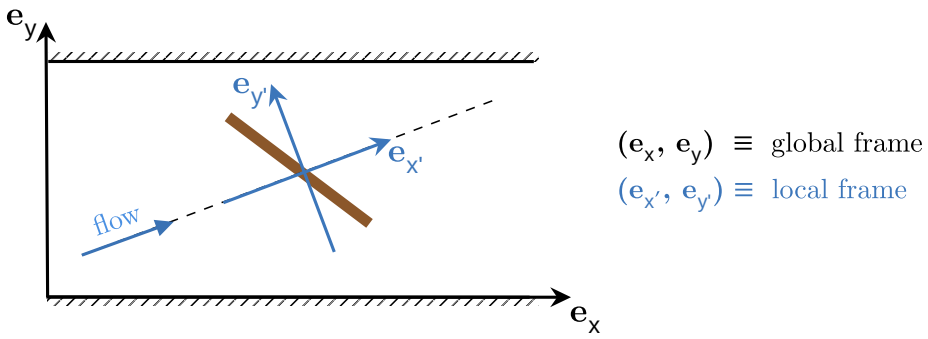

Figure 2: Global and local frames convention.

Then Tab.(4) is presented to examine the nature of motion explored in the articles. The only exception is the seminal work by (Ghaffarian et al., 2020), which excludes rotation from its study as it pertains specifically to spheres.

Models \ Mvmt type	translation	rotation
Ghaffarian et al. (2020)	■	
Ruiz-Villanueva et al. (2014)	■	■
Persi et al. (2017)	■	■

Table 4: Type of movement study in the different articles.

Afterwards, a survey of the forces appearing in the force balances of the various reference articles is carried out. To columns correspond to

- ▷ $\mathbf{F}_d$: component of the hydrodynamic in the direction of the relative velocity, called the drag force;
- ▷ $\mathbf{F}_s$: component of the hydrodynamic force in the perpendicular direction of the relative velocity, called the side force;
- ▷ $\mathbf{F}_g$: effective weight of the object in the downstream direction the weight, called the effective weight;
- ▷ $\mathbf{F}_f$: the friction force between the object and the flume's bed;
- ▷ $\mathbf{F}_p$: the force that the fluid would exert on the body if the presence of the body had not disturbed the flow called the Froude-Krylov force;
- ▷ $\mathbf{F}_{am}$: the force related to the additional inertia of the fluid surrounding the object, called the added mass force.

The Tab.(5) presents the forces comparison.

Models \ Forces	$\mathbf{F}_d$	$\mathbf{F}_s$	$\mathbf{F}_g$	$\mathbf{F}_f$	$\mathbf{F}_p$	$\mathbf{F}_{am}$
Ghaffarian et al. (2020)	■				■	■
Ruiz-Villanueva et al. (2014)	■		■	■		
Persi et al. (2017)	■	■			■	■

Table 5: Force taken into account in the dynamic models according to different articles.

Then, the objective is to present the complete path of model development, more or less common to the various model references. The transition from one model to another is often omitted in the literature, and this section aims also to clarify these omissions. To structure the study, the composition theorem of movements is recalled. It is stated as "All motion of a non-deformable body is decomposed into translational and rotational motion" (Batchelor, 1967). The motion of particles, regardless of their shape (spherical or non-spherical), can be explained by taking into account the conservation of both linear and angular momentum. In their differential form they write as follows

$$\begin{cases} \dfrac{d\mathbf{r}}{dt} = \mathbf{v}, \\ m\dfrac{d\mathbf{v}}{dt} = \sum_i \mathbf{F}_i. \end{cases} \tag{1}$$

$$\begin{cases} \dfrac{d\theta}{dt} = \boldsymbol{\omega}, \\ I\dfrac{d\boldsymbol{\omega}}{dt} = \sum_i \mathbf{T}_i. \end{cases} \tag{2}$$

where $\mathbf{r}$ is the position vector, $\mathbf{v}$ is the body linear velocity, m is the body mass, $\mathbf{F}$ the forces acting on the body, θ a measure of the orientation defined as the angle the principle axis of the body and the flow direction, $\boldsymbol{\omega}$ the body angular velocity, I the body moment of inertia and $\mathbf{T}$ the torque acting on it. The Eq.(1) gives the physics of the position and the linear velocity, while Eq.(2) allows the study of the orientation and angular velocity of the body.

The following subsections aim to explain, step by step, the development of models for a large floating object. Specifically, all notations are standardized according to the conventions used in this work, and the same applies to coordinate system notations (Cartesian coordinates).

2.2 Models for translation

Initially, the translation models for Eq.(1) are examined in this section. The study starts from the least general model and progressing towards the more comprehensive one. The writing conventions adopted are those clarified at the start of the work .

2.2.1 Starting point

Although there is no common reference model for writing the force balance acting on a floating (non-symmetric) object, every models of the articles are referred as the generalized Basset-Boussines-Oseen (BBO) model written as follows.

Model by Basset-Boussinesq-Oseen (Parmar et al., 2011)
By denoting $\mathbf{F}_s$ the side force, $\mathbf{F}_{am}$ the added mass force, $\mathbf{F}_B$ the Basset force, $\mathbf{F}_p$ the Froude-Krylov force and $\mathbf{F}_g$ all the other forces acting on the sphere as the gravity, the force balance writes

$$m_s \frac{d\mathbf{v}}{dt} = \mathbf{F}_s + \mathbf{F}_{am} + \mathbf{F}_B + \mathbf{F}_p + \mathbf{F}_g \tag{3}$$

$$\begin{aligned} \Longleftrightarrow m_s(1+C_{am})\frac{d\mathbf{v}}{dt} = 6\pi\eta r\,\mathbf{v} + C_{am} m_s \frac{d\mathbf{u}}{dt} + 6r^2\rho_w\sqrt{\pi\eta}\int_{t_0}^{t}\frac{1}{\sqrt{t-\tau}}\frac{d}{d\tau}\left(\mathbf{u}(\tau)-\mathbf{v}(\tau)\right)\mathrm{d}\tau \\ -\int\int_{S_w} p\mathbf{n}ds - \frac{4}{3}\pi r^3\boldsymbol{\nabla} p + 4\pi r^2\rho\mathbf{g}, \end{aligned} \tag{4}$$

with $\mathbf{v}$ the linear velocity of the sphere, $\mathbf{u}$ the flow velocity, ρ_w the fluid density, ρ the sphere density, S_w the wetted surface of the sphere, m_s the mass of the sphere, r the radius of the sphere, p the pressure, η the dynamic viscosity, C_{am} the added mass coefficient and $\mathbf{g}$ the gravitational acceleration.

The rest of the section describes the basic BBO model step by step. However, its generalization seems more arbitrary. The reference articles justify the use of their forces and expressions by associating their model as "a generalized BBO model". In the following, it is shown that some passages from the basic BBO model to the generalized model are often omitted while the working hypotheses are drastically different.

The BBO equations provide a mathematical framework to describe the Lagrangian acceleration of a spherical particle moving within an unsteady flow, where the Reynolds number is less than one (Parmar et al., 2011). A schematic representation is shown in Fig.(3).

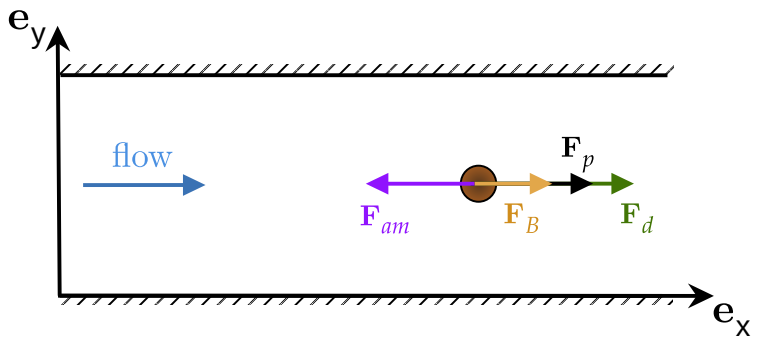

Figure 3: Forces acting on a particle in the horizontal plane (x,y) according to according to the Basset-Boussinesq-Oseen model (Parmar et al., 2011).

These equations consider that the second Newton's law of the particle is written as

$$m_s \frac{d\mathbf{v}}{dt} = \mathbf{F}_s + \mathbf{F}_{am} + \mathbf{F}_B + \mathbf{F}_p + \mathbf{F}_g, \tag{5}$$

where the forces are presented one by one using the nomenclature presented before. In particular, $\mathbf{u}$ denotes the flow velocity and $\mathbf{v}$ the sphere velocity.

$\mathbf{F}_s$ represents the Stoke's drag. This force of viscosity can be expressed as follows when it acts on a small sphere moving through a laminar, viscous and homogeneous fluid (Parmar et al., 2011):

$$\mathbf{F}_s = 6\pi\eta r\mathbf{v}, \tag{6}$$

with η the dynamic viscosity and r the radius of the sphere. Into more details, this empirical law provides an expression for the hydrodynamic force component acting in the direction of the relative velocity.

$\mathbf{F}_{am}$ represents the added mass (or virtual mass) force (Mandø and Rosendahl, 2010) due to inviscid effect. It allows to model the physics for the additional inertia of the fluid surrounding the particle. It is generally expressed as

$$\mathbf{F}_{am} = C_{am} m \frac{d}{dt}(\mathbf{u} - \mathbf{v}), \tag{7}$$

with C_{am} the added mass coefficient and m the mass of fluid displaced by the sphere. The added mass coefficient is a dimensionless parameter that quantifies the additional water volume accelerated when the body undergoes acceleration relative to the surrounding flow. It primarily depends on the body's shape and orientation ((Batchelor, 1967)). For a sphere, C_{am} equals 0.5.

$\mathbf{F}_B$ denotes the Basset force due to viscous-unsteady effects. This Basset history term is a nonlinear component of the equation (if the velocity field is space-dependent), arising from the delayed development of the boundary layer due to viscous-unsteady effects. It is the result of interactions between the body and the surrounding fluid, introducing a temporal aspect to the fluid dynamics. The expression presented by Basset-Boussinesq is

$$\mathbf{F}_B = 6r^2\rho_w\sqrt{\pi\eta}\int_{t_0}^{t} \frac{1}{\sqrt{t-\tau}} \frac{\mathrm{d}}{\mathrm{d}\tau}(\mathbf{u}(\tau) - \mathbf{v}(\tau))\,\mathrm{d}\tau. \tag{8}$$

The latter term is often neglected in rigid body models, due to its complexity. Nevertheless, given its significance in turbulent flows or scenarios involving bed-load transport, some approaches are proposed to incorporate the Basset history term in computations in (Michaelides, 1992) (Dorgan and Loth, 2007).

$\mathbf{F}_p$ accounts for the Froude-Krylov force. It is introduced by the unsteady pressure field generated by undisturbed waves. It is part of the total non-viscous forces acting on a floating body in regular waves due to the pressure gradient in the undisturbed flow

$$F_p = -\int\int_{S_w} p\mathbf{n}ds, \tag{9}$$

with S_w the wetted surface, and $\mathbf{n}$ the normal vector of the body pointing into the water. Assuming the sphere is sufficiently small By considering the body to be small enough that it does not significantly influence the pressure field caused by an incident wave, Soo (1990) gives

$$\mathbf{F}_p = -\frac{4}{3}\pi r^3 \boldsymbol{\nabla} p. \tag{10}$$

Its generalization is not straightforward and is discussed later.

Eventually, $\mathbf{F}_g$ encounters all the other forces acting on the sphere, often including gravity. The complete model is thus written as in Eq.(11).

$$\begin{aligned} m_s\frac{d\mathbf{v}}{dt} = 6\pi\eta r\,\mathbf{v} + C_{am}m_s\frac{d}{dt}(\mathbf{u}-\mathbf{v}) + 6r^2\rho_w\sqrt{\pi\eta}\int_{t_0}^{t}\frac{1}{\sqrt{t-\tau}}\frac{d}{d\tau}(\mathbf{u}(\tau)-\mathbf{v}(\tau))\,\mathrm{d}\tau \\ -\int\int_{S_w} p\mathbf{n}ds - \frac{4}{3}\pi r^3\boldsymbol{\nabla} p + 4\pi r^2\rho\mathbf{g}. \end{aligned} \tag{11}$$

By grouping the body acceleration term, the expression of the BBO of the beginning can be found back.

2.2.2 Extension to finite and low Reynolds number

This first extension is provided by Ghaffarian et al. (2020) whose model is written as follows.

Model by Ghaffarian et al. (2020)
By denoting $\mathbf{F}_{am}$ the added mass force and $\mathbf{F}_d$ the drag force, the force balance writes

$$m\frac{d\mathbf{v}}{dt} = \mathbf{F}_{am} + \mathbf{F}_d \tag{12}$$

$$\Longleftarrow m(1+C_{am})\frac{d\mathbf{v}}{dt} = m(1+C_{am})\frac{D\mathbf{u}}{Dt} + \frac{1}{2}\rho_w C_d S_p|\mathbf{u}-\mathbf{v}|(\mathbf{u}-\mathbf{v}), \tag{13}$$

with $\mathbf{v}$ the linear velocity, $\mathbf{u}$ the fluide velocity, m the mass of the floating object (equals to the mass of the displaced fluid), C_{am} the added mass coefficient, C_d the drag coefficient, S_p the projected area, ρ_w the fluid density and $\frac{D}{Dt}$ the convective derivative equal to $\frac{\partial}{\partial t} + \mathbf{u}\cdot\boldsymbol{\nabla}$.

The forces appearing in the model are represented in Fig.(4) and are described in detail below.

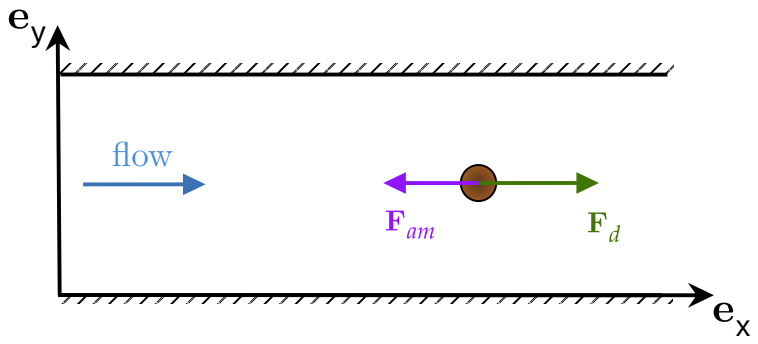

Figure 4: Force acting on a sphere according to Ghaffarian et al. (2020)'s model.

First, the model only studies the x, y) horizontal plane. Then, the assumption of a spherical body is retained, as shown in the preceding table Tab.(2). The considered floating object is supposed to be similar to the size of the wood in rivers. The latter implies that capillary effect can be neglected.

The next step is to generalize the previous model by assuming a low but finite Reynolds number. The first consequence is that the Stoke Force expressed in the BBO equations is no longer valid (it requires $Re \ll 1$). In this context, another expression of the hydrodynamic force is needed. Its name is reduced to drag force. A possible model consists in writing the force as a quadratic expression of the relative velocity. Ghaffarian et al. (2020) suggests the following formulation

$$F_d = \frac{1}{2}\rho_w C_d S_p |\mathbf{u}-\mathbf{v}|(\mathbf{u}-\mathbf{v}), \tag{14}$$

with C_d the drag coefficient and S_p the projection of cross-area of the cylinder in the flow direction. The writing proposed in the article suggests that these are constant quantities. This is the case only for S, calculated as $\frac{4}{3}\pi r^3$. For the drag coefficient, it depends on the particle Reynolds number Re_p defined as

$$Re_p = |\mathbf{u}-\mathbf{v}|\frac{d}{\eta} \tag{15}$$

with d a characteristic size of the object and η the kinematic viscosity (equal to 10^{-6} $[m^2/s]$ for water at 20°C). In a following a side note, it is explained that the coefficient also depends on the orientation of the object. As the sphere is perfectly symmetrical, there is no such dependence in this model. Writing the quadratic dependence in this way allows to take into account the orientation of the drag force via the term between absolute values.

The second consequence is the disappearance of the term Basset. In the BBO equations, the low Reynolds number for which the Stokes equations are linear enables a clear distinction to be made between the quasi-stationary drag force, the added mass contribution and the Basset force. The opposite is true at finite Reynold's numbers: the mechanisms for distinguishing between viscous effects (in the historical Basset term) and purely inertial effects (in the added-mass term) are coupled.

Indeed, in the BBO equations, the low Reynolds number for which the Stokes equations are linear allows a clear distinction between viscous effects (in the historical Basset term) and purely inertial effects (in the added mass term). This is why there is a distinction between the quasi-stationary drag force, the added mass contribution and the Basset force. The reverse is true at

finite Reynold's numbers. It is necessary to go back to the work of Mei and Adrian (1992) to understand that the long-time behavior of the Basset force is dictated by inertial effects. Thus, the Basset force is negligible for this model.

Regarding the weight, the force is not considered in this model, although it was present in the BBO equations. This can be explained as follows : the authors are studying the 2D motion of the particle on a flat bottom, which implies that there is no component of this force on the horizontal plane studied. This (implicit) assumption is very common in the literature.

The transition from BBO equations to models such as this may pose a problem for the reader. Indeed, the literature gives no explanation about that. A thorough search had to be carried out to find an explanation. A section "Froude-Krylov force" 2.2.2 is presented to get an overview of its different writings. In any case, the current model presents this force as "the force due to the pressure gradient and the added mass, both appearing in unsteady and/or non-uniform flows" and writes it as

$$F_p = m(1 + C_{am})\frac{D\mathbf{u}}{Dt}. \tag{16}$$

At this stage, the Ghaffarian et al. (2020) model, as presented in the article, is complete. Once this initial generalization has been made, the authors usually refer to these equations as the "generalized model of the BBO equations". As it does not reduce only to this formulation, the "generalized" word must be understood as "generalization to an object of macroscopic size in a finite Reynolds number flow". The final form of the model is the one presented in the beginning of this point in Eq.(13).

Froude-Krylov force

The rewriting of the Froude-Krylov force is delicate. The literature provides no explanation for the passage of this force from the BBO equations to one the generalized model, apart from the notion of using the "generalized model of the BBO equations", which itself provides no justification. To understand this, it is necessary to go back to the establishment of the expression of this force.

First, let ones recall how this force is defined in the different models. The formulation of F_p in the initial BBO model is

$$F_p = -\int\int_{S_w} p\mathbf{n}ds = -\frac{4}{3}\pi r^3 \nabla p, \tag{17}$$

remembering that the calculated surface in question is the one of a sphere. For this model, F_p is defined as the "force due to the pressure gradient in the undisturbed flow, with p(**x**,t) the undisturbed pressure field". The formulation in the other article is

$$F_p = m\frac{d\mathbf{u}}{dt}, \tag{18}$$

where $m = m_s(1 + C_{am})$ in Ghaffarian et al. (2020) and $m = m_c$ in Persi et al. (2017), while its definition varies according to the article :

- ▷ (Ghaffarian et al., 2020)"the force due to the pressure gradient and the added mass, both appearing in unsteady and/or non-uniform flows";
- ▷ (Persi et al., 2017) : named after the pressure force and is defined as the "force exerted on a volume of fluid equal to the body volume in the undisturbed flow".

A first observation is that the pressure gradient present in the BBO equations no longer exists in the generalized model. Moreover, the articles do mention the Froude-Krylov force as a pressure force. In addition, if the Tab.(5) is looked back, it can be seen that the model in Ruiz-Villanueva et al. (2014) does not include any F_p, but consider the weight. Thus, only flat-bottomed models make F_p explicit. In other words, either a weight component is taken into account, or the force F_p. Finally, these forces help to explain the motion of the fluid (in this case, the water). This observation may be enough to convince the reader that the form of force in the various models is then correct. However, as it is referred to the Froude-Kylov force, there is an uncertainty that can be seen as an inconsistency.

Then, to justify the different formulations of this force, it is necessary to go into a little more detail. Although it may seem counter-intuitive, it is useful to study the "diffraction theory" in hydromechanics Journée and Massie (2001). The following explanation is intended to be succinct and is not present the proof, which would require notions that is no longer be useful later on.

This theory includes the principle of "superposition of hydromechanical and wave loads", which is useful for the design and analysis of offshore structures and other floating or submerged structures subjected to ocean conditions. Hydromechanical loads refer to the forces and moments acting on a structure due to its interaction with the surrounding fluid (usually water). These loads can be caused by factors such as currents, tides, and flow. On the other hand, wave loads are caused by the action of waves on the structure, resulting in dynamic forces. In order to determine the weight of each component, theory has established regimes depending on the wave length and other flow characteristics. As the floating-object models considered are aimed at river applications, there is no such thing as a wave. Taking this into account, and studying the associated regime, theory indicates that inertial loads are dominant. However, there are two parts to these loads: the Froude-Krylov force and the added mass effect (Shyamcharan, 1979).

In this decomposition, the theory proposes a more rigorous definition of this force, which the literature discussed earlier does not specify. This definition would be "the force that the fluid would exert on the body if the presence of the body had not disturbed the flow". By considering all of this, it is trivial to obtain the expression of F_p. To do this, it is necessary to consider classical simplifications of the Navier-Stokes equation for higher Reynolds numbers. This means that

$$\mathrm{Re} = \frac{\|\mathbf{u}\nabla\mathbf{u}\|}{\|\eta\Delta\mathbf{u}\|} >> 1, \tag{19}$$

that implies that inertial advection terms are dominant over viscous diffusion terms. Taking this into account in the Navier-Stokes equations and considering an horizontal plane (xy), one simplifies them as

$$\rho\left(\frac{\partial\mathbf{u}}{\partial t} + \mathbf{u}\nabla\mathbf{u}\right) = \rho\cancel{\mathbf{g}_{xy}} - \nabla p + \cancel{\eta\Delta\mathbf{u}}. \tag{20}$$

In total, one finds back the simple expression

$$\nabla p = -\rho\frac{d\mathbf{u}}{dt}. \tag{21}$$

The presence of the added mass term in the Ghaffarian et al. (2020) model stems from the fact that the added mass effect arises due to the presence of the body, and disturbs locally the fluid by leading to heightened fluid accelerations.

In conclusion, realizing that this force F_p models represents a cause of the flow allows to understand the presence of this force in the models. However, the definition associated with it, as well as the name Froude-Krylov force, does not correspond to the situation that is desired to model. In order to put to rest the uncertainty that may be perceived as an inconsistency. This term is intended for the original force which, following reasoning on diffraction theory and considerations, leads to the expression involving the fluid's local acceleration. But this is not straightforward, and the lack of justification may lead the reader to believe that the force is badly defined.

2.2.3 Extension to non-spherical objects

Another aspect of the generalization of the previous model may concern the shape of the object. The new object of study is a cylinder. The simplification of the various forces presented above do not vary, since this section focuses on the shape and not the size of the object. However, the way the body deforms the flow is impacted. It is from the removal of this latter assumption that the final models for large floating objects are derived. However, the various formulations of these models differ from one article to another. As explained at the very beginning of this section, the analysis of the literature review resulted in two distinct groups of models. The outcome of these different models, in terms of numerical and laboratory simulations, are in fact presented in the two reference articles (Ruiz-Villanueva et al., 2014) and (Persi, 2015). This subsection is therefore divided into two parts.

Model of Persi (2015)

First, the model by Persi (2015) is presented. It represents the culmination of most floating object models. Other articles from the literature are referenced for the detailed explanations that require further investigation.

Model by Persi (2015)
By denoting $\mathbf{F}_d$ the drag force, $\mathbf{F}_s$ the side force and $\mathbf{F}_{am}$ the added mass force, the force balance write

$$m_c \frac{d\mathbf{v}}{dt} = \mathbf{F}_d + \mathbf{F}_s + \mathbf{F}_{am} \tag{22}$$

$$\begin{aligned} \Longleftrightarrow \left(m_c + \frac{1}{2} C_{am} m_w\right) \frac{d\mathbf{v}}{dt} &= \frac{1}{2}\rho_w C_d S_p \left(\mathbf{u}-\mathbf{v}\right)|\mathbf{u}-\mathbf{v}| \\ &+ \frac{1}{2}\rho_w C_s S_p \left[\left(\mathbf{u}-\mathbf{v}\right)|\mathbf{u}-\mathbf{v}|\right] \times \boldsymbol{n}_z \\ &+ \rho_w \left(1 + \frac{1}{2} C_{am}\right) V_c \frac{D\mathbf{u}}{Dt} \end{aligned} \tag{23}$$

with $\mathbf{v}$ the linear velocity of the cylinder, $\mathbf{u}$ the flow velocity, m_w the displaced fluid mass, m_c the cylinder mass, V_c its volume, S_p its projected area, ρ_w the fluid density C_d and C_s the drag and side coefficients, $\mathbf{n}_z$ the unit vector normal to the 2D flow plane and $\frac{D}{Dt}$ the convective derivative equal to $\frac{\partial}{\partial t} + \mathbf{u} \cdot \boldsymbol{\nabla}$.

The forces acting on the cylinder can be represented as in the Fig.(5) and are described in detail below.

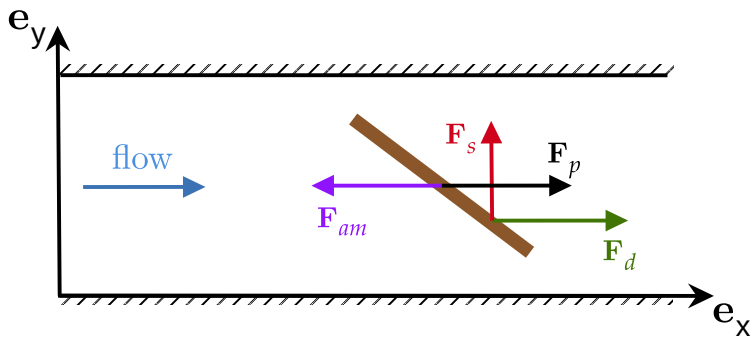

Figure 5: Forces acting on a cylinder in the horizontal plane (x,y) according to Persi (2015).

The main difference with the previous model is the appearance of a force called *side force*. Eliminating the assumption of a spherical object entails significant implications for the hydrodynamic forces. The reference rigid body takes the form of a cylinder. In the previous models,it was modeled with only one contribution called the *drag force* in the direction of the relative velocity.

The total hydrodynamic force exerted on this body must replicate the effect of flow deflection. In a first scenario where the cylinder is aligned or perpendicular to the flow, there is no flow deflection, resulting in a hydrodynamic force reduced to the drag force. Conversely, if a cylinder is neither aligned nor perpendicular to the flow, it asymmetrically diverts the streamlines, leading to an alteration in pressure distribution. This modification in pressure distribution generates a lateral component of the hydrodynamic force, known as the side force (Mandø and Rosendahl, 2010). Literature is divided on the expression of this force and a note on the side force is given below. In all cases, the total hydrodynamic force, F_h, is generally given by

$$\mathbf{F}_h = \mathbf{F}_s + \mathbf{F}_d, \tag{24}$$

with F_d the drag force which keeps the same expression as before and F_s expressed in this model as

$$\mathbf{F}_s = \frac{1}{2}\rho_w C_s S_p \left[(\mathbf{u}-\mathbf{v})\,|\mathbf{u}-\mathbf{v}|\right] \times \boldsymbol{n}_z. \tag{25}$$

where $\mathbf{n}_z$ is the unit vector normal to the 2D flow plane (x,z), allowing compact writing of the following expressions for the side force directed along $\mathbf{e}_y$, denoted $F_s^{\mathbf{e}_y}$, and that directed along $\mathbf{e}_x$, denoted $F_s^{\mathbf{e}_x}$, as

$$\mathbf{F}_s^{\mathbf{e}_x} = \frac{1}{2}\rho_w C_s S_p \left(\mathbf{u_y}-\mathbf{v_y}\right)\left|\mathbf{u_y}-\mathbf{v_y}\right| \tag{26}$$

$$\mathbf{F}_s^{\mathbf{e}_y} = \frac{1}{2}\rho_w C_s S_p \left(\mathbf{u_x}-\mathbf{v_x}\right)\left|\mathbf{u_x}-\mathbf{v_x}\right| \tag{27}$$

with subscripts x and y indicating the velocity components used.

The origin of these forces is the pressure distribution around the cylinder, necessitating special attention to the point of force application. When the cylinder symmetrically distorts the flow, their point of application corresponds to the object's center of mass. Conversely, when the pressure field is non-uniform, it is applied at a point known as the center of pressure. This point is where all the pressure on the cylinder would hypothetically be concentrated. A later section clarifies the concept and modelling of center of pressure in the rotation section, where it holds all its importance. Fig.(6) provides a qualitative illustration of how the hydrodynamic force components change based on the cylinder's orientation.

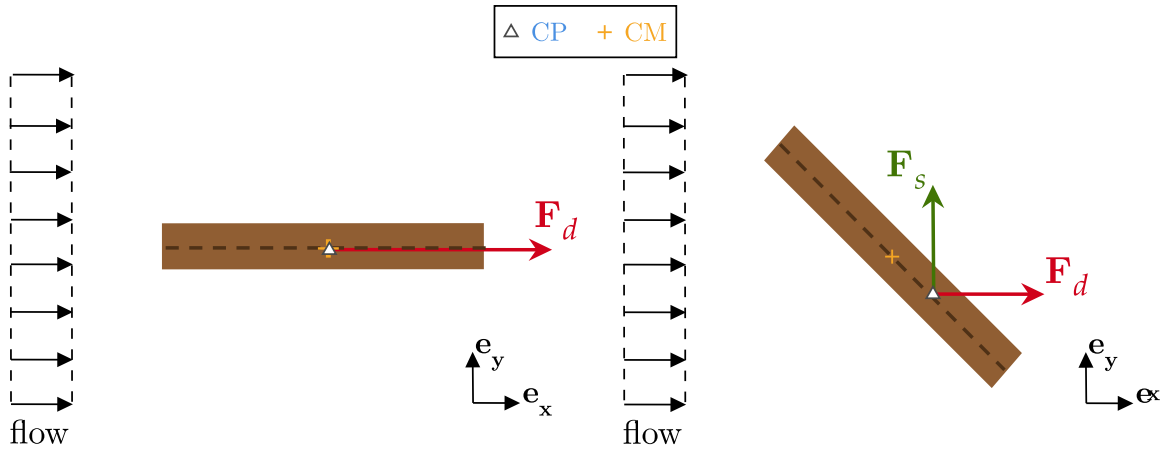

Figure 6: Components of the hydrodynamic force on a cylinder according to its orientation to the flow. *CM* stands for center of mass and *CP* for center of pressure.

Model of Ruiz-Villanueva et al. (2014)

Secondly, the model by Ruiz-Villanueva et al. (2014) is presented. A more precise ewplanation is presented below. Broadly speaking, the current model has been designed for on-field application.

Model by Ruiz-Villanueva et al. (2014) By denoting $\mathbf{F}_f$ the friction force, $\mathbf{F}_g$ the weight and $\mathbf{F}_d$ the drag force, the force balance writes

$$m_c \frac{d\mathbf{v}}{dt} = \mathbf{F}_f + \mathbf{F}_g + \mathbf{F}_d \tag{28}$$

$$\begin{aligned} \iff m_c \frac{d\mathbf{v}}{dt} = &-\Big(\mathbf{g}\rho_c S_c - \mathbf{g}\rho_w L_c S_{sub}\Big)\Big(\mu_{bed}\cos\alpha\Big) \\ &-\Big(\mathbf{g}\rho_w L_c S_{sub} - \mathbf{g}\rho_c S_c\Big)\Big(\sin\alpha\Big) \\ &+\frac{\mathbf{u}^2}{2}\rho_w C_d\Big(L_c \sin\theta + S_{sub}\cos\theta_{u-v}\Big), \end{aligned} \tag{29}$$

with $\mathbf{v}$ the linear velocity of the cylinder, $\mathbf{u}$ the fluid velocity, $\mathbf{g}$ the gravitational acceleration, m_c the cylinder's mass, ρ_c its density, S_c its surface, S_{sub} its submerged surface, ρ_w the fluid density, θ_{u-v} the angle bewteen the relative velocity and the major axis of the cylinder, α the angle of the channel bed in the direction of the flow and μ_{bed} the friction coefficient bewteen the cylinder and the bed.

First of all, one of the biggest difference with the previous model is the absence of side force, despite the cylinder shape of the object. In fact, they operate under the additional assumption of a very slightly submerged cylinder, making the side force negligible.

The forces acting on the cylinder can be represented as in the Fig.(7) and are described in detail below.

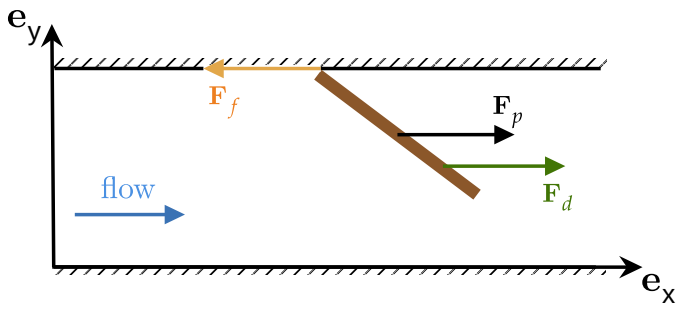

Figure 7: Forces acting on a cylinder in the horizontal plane (x,y) according to Ruiz-Villanueva et al. (2014)'s model.

Then, this model calculates the gravitational force $\mathbf{F}_g$, a choice substantiated by the representation of an uneven terrain. By denoting α the angle of the channel bed in the direction of the flow, the effective weight $\mathbf{F}_w$ is computed as

$$\mathbf{F}_g = \mathbf{F}_w \sin(\alpha). \tag{30}$$

By defining S_w the area of the cylinder perpendicular to the piece length L_c and S_{sub} the submerged area of the cylinder perpendicular to L_c, the previous force writes[2]

$$\mathbf{F}_g = \Big(\mathbf{g}\rho_c L_c - \mathbf{g}\rho_w L_c S_{sub}\Big)\sin(\alpha). \tag{31}$$

This model takes also into account the presence of frictional forces, $\mathbf{F}_f$. This force acts in the opposite direction to the flow is determined by the normal force, noted $\mathbf{F}_n$ exerted on the cylinder, multiplied by the coefficient of friction between the cylinder and the bed denoted μ_{bed} :

$$\mathbf{F}_f = \mathbf{F}_n \mu_{bed}. \tag{32}$$

Into more details, the article presents the normal force as equal to

$$\mathbf{F}_n = \mathbf{F}_w \cos(\alpha), \tag{33}$$

with α the angle of the channel bed in the direction of the flow. The final expression of the force is then

$$\mathbf{F}_f = \Big(\mathbf{g}\rho_c L_c S_c - \mathbf{g}\rho_w L_c S_{sub}\Big)\mu_{bed}\cos(\alpha). \tag{34}$$

Finally, the drag force $\mathbf{F}_d$, which is the only force in common between the two models presented, is written in this article as

$$\mathbf{F}_d = -\frac{1}{2}\rho_w C_d \Big(L_c h \sin(\theta_{u-v}) + S_{sub}\cos(\theta)\Big)(\mathbf{u}-\mathbf{v})^2, \tag{35}$$

with h the flow depth.

2.1.3.a Side force models

Literature is divided on the expression of this force. This note clarifies the problem. For the model of the side force, Mandø and Rosendahl (2010) suggests to write simply this force as the drag force, but with the corresponding projected surface S_p and coefficient C_s :

$$F_s = \frac{1}{2}\rho_w C_s S_p (\mathbf{u}-\mathbf{v})|\mathbf{u}-\mathbf{v}|. \tag{36}$$

[2]The article provides expressions for various surfaces. However, these expressions are not be reproduced here.

As a reminder, Persi (2015) suggests the following formulation

$$F_s = \frac{1}{2}\rho_w C_s S_p (\mathbf{u}-\mathbf{v})|(\mathbf{u}-\mathbf{v})| \times \mathbf{n_z}, \tag{37}$$

where $\mathbf{n}_z$ is the unit vector normal to the 2D flow plane (x,z), allowing the side force expression to be written as a y-component with only the x-components of the velocities and vice versa. Indeed, the study being purely plane, all z-components of the cross-product vanish. In the same idea, Yin et al. (2003) writes

$$F_s = \frac{1}{2}\rho_w C_s S_p \frac{\mathbf{e}_{y'} \cdot (\mathbf{u}-\mathbf{v})}{|\mathbf{u}-\mathbf{v}|}[\mathbf{e}_{y'} \times (\mathbf{u}-\mathbf{v})] \times (\mathbf{u}-\mathbf{v}), \tag{38}$$

where $e_{y'}$ is the axis of the local frame aligned with the cylinder's major axis.

These three formulations appear to describe differently the side force. Indeed, using the relative velocity norm as proposed in Eq.(36) or Eq.(38) seems appropriate to attribute a negative direction to the side force when the object is faster than the flow, contrary to the Eq.(37) for this force often found in the literature. In addition, the Eq.(37) and Eq.(38) have the advantage of being more rigorous in terms of the velocity components required for force calculation. The difference is the speeds taken in the norm. It would seem appropriate to use the expression of Eq.(38). This final expression, while seemingly intricate, effectively captures the underlying physics of the force. This formulation takes into account the fact that the side force is perpendicular to the relative velocity $(\mathbf{u}-\mathbf{v})$ and lies within the plane defined by the direction of the particle's major axis $(\mathbf{e}_{y'})$ and the relative velocity $(\mathbf{u}-\mathbf{v})$. Additionally, it ensures that the side remains unchanged when the particle's major axis $(\mathbf{e}_{y'})$ undergoes a 180-degree rotation and becomes null when the parameter the inclination angle θ_{u-v} equals 0 or 180[°].

Lastly, it is crucial to precise that the parameters notation in the three formulations can be confusing. In fact, these are not constant parameters. The projected surface S_p is influenced by the angle θ_{u-v} and similarly, the side coefficient depends on it, in addition to its correlation with the particulate Reynolds number.

2.1.3.b Projected areas models

The literature does not typically specify that the projected surface is dependent on the orientation of the cylinder. However, it is crucial to explicitly address this dependence. In the case of a cylinder that is not aligned with the flow, the projected area needs to be computed. According to Saucier (2016), the projected area $S_p(\theta_{u-v})$ is given by

$$S_p(\theta_{u-v}) = L_c d_c |\sin\theta_{u-v}| + \frac{\pi}{4} d_c^2 |\cos\theta_{u-v}| \tag{39}$$

where θ_{u-v} is the angle between the cylinder major axis and the relative velocity, L_c the cylinder's length and d_c its diameter. The two peculiar cases can be found back. Indeed, at 0[°], the projected area is that of the base of the cylinder, and at 90[°] that of the total lateral half-area.

Although such formulas do exist, they are not always used in practice. Indeed, the calibration of hydrodynamic coefficients, which is be the subject of the following section, is carried out based on the drag area defined as

$$S_d(\theta_{u-v}, \mathrm{Re}_p) = C_d(\theta_{u-v}, \mathrm{Re}_p) S_p \tag{40}$$

As a result, this kind of calibration is sufficient for accounting for the dependence of the projected area on the cylinder's orientation.

2.1.3.c Hydrodynamic coefficients models

Hydrodynamic coefficients provide insights into how a fluid exerts forces and torques on a cylinder. While these coefficients are well-established for simple shapes (e.g., spheres) or hypothetical cases (e.g., infinitely long cylinders), determining these hydrodynamic coefficients for a finite cylinder requires experimental approaches.

First of all, comprehending the parameters that influence these coefficients is crucial. Mandø and Rosendahl (2010) have addressed this challenge by attempting to establish correlations between known coefficients for spheres and those desired for cylinders. The article subsequently characterizes the drag coefficient, C_d, as a function of the particle Reynolds number and the sphericity ψ (used to quantify the shape), such as:

$$C_d = C_d(\mathrm{Re}_p, \psi), \tag{41}$$

with the particle Reynolds number defined as previously

$$Re_p = |\mathbf{u} - \mathbf{v}| \frac{d}{\eta} \tag{42}$$

with d a characteristic size of the object and η the kinematic viscosity. The characteristic curves of the drag coefficient as a function of Reynolds number exhibit three distinct regimes. Firstly, the Stokes regime where C_d can be approximated as

$$C_d = 24/\mathrm{Re}_p \tag{43}$$

Secondly, a Newtonian regime where the coefficient becomes constant with respect to Re_p, and finally, the drag crisis where the coefficient drops sharply, corresponding to the sudden detachment of the air boundary layer from a moving surface, leading to a drastic decrease in its value Rosendahl (2000a). Such curves are reported in Fig.(8).

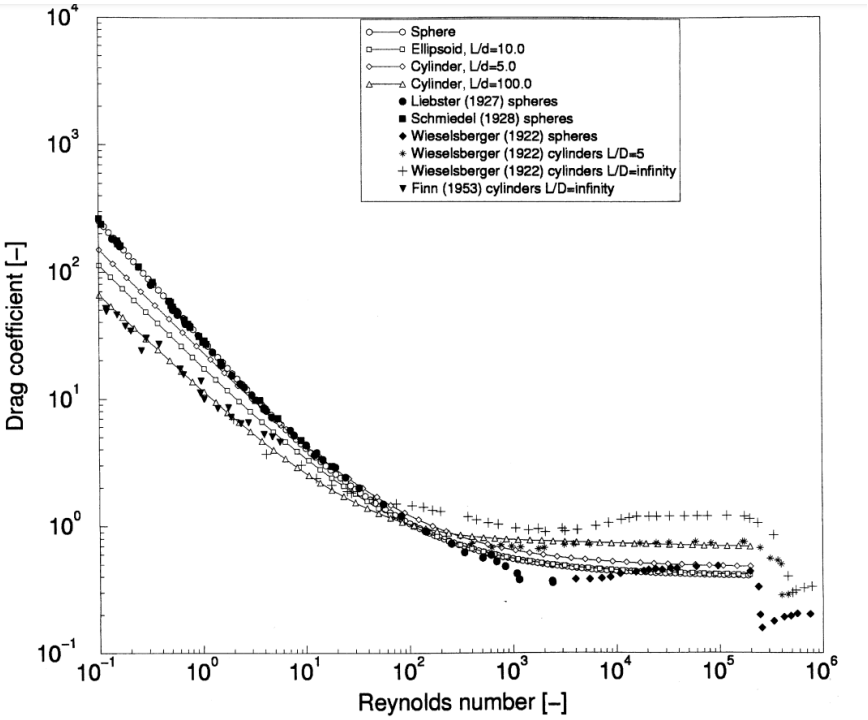

Figure 8: Drag coeffients of spheres, ellipsoids and cylinders of different aspect ratios (Rosendahl, 2000a).

Studies on the correlations in question are unsuccessful for cylinders. This is why Persi (2015) devotes part of his thesis to such a study. Specifically, their work involves the measurement of drag and side coefficients for cylinders, contributing essential data for integration into 2D numerical simulations of trunk transportation. The conclusions are that the coefficient also depends on the orientation of the cylinder such that

$$C_d = C_d(\mathrm{Re}_p, \theta_{u-v}). \tag{44}$$

Several scenarios are simulated in the laboratory. The data for the hydrodynamic coefficient calibrated on semi-submerged cylinders are shown in Fig. where a cubic interpolation has been processed.

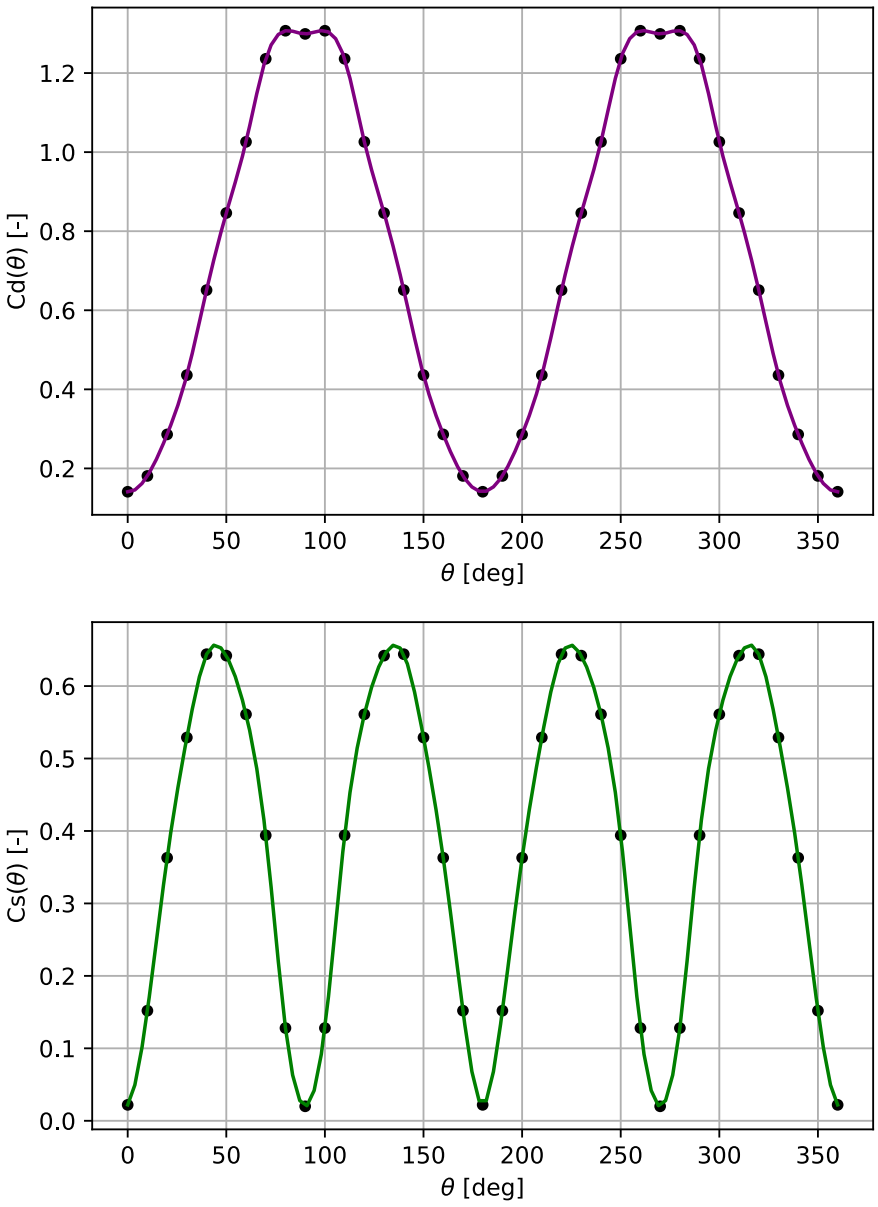

Figure 9: Cubic interpolation of the experimental data for semi-submerged cylinder, for the drag coefficient (left) and the side coefficient (right) (Persi, 2015).

Regarding drag, two maxima (1.122[-]) are observed at 90 and 180 degrees, angles at which drag is maximized. It can be noted that for the side coefficient, negligible values are present at multiples of 90 degrees (positions of stable and unstable equilibria), while more significant values occur in between. The side force is non-negligible in this semi-submerged case, as the coefficients rise up to 0.622[-].

2.3 Models for rotation

This new subsection focuses on the model of Eq. (2). The focus is on the rotation of the object. More specifically, the term *rotation* used hereafter exclusively refers to *yaw*. Indeed, there are various possible rotational movements for the body. The rotation about the axis extending from front to back is referred to as roll. Then, the rotation about the axis extending from side to side is termed pitch. Finally, rotation about the vertical axis is denoted as yaw. Fig.(10) represents them. For this type of rotation, (Ghaffarian et al., 2020) odes not study it, as is uses spherical objects (see Tab.(2)). Once again, this part is separated into two : one for each type of models.

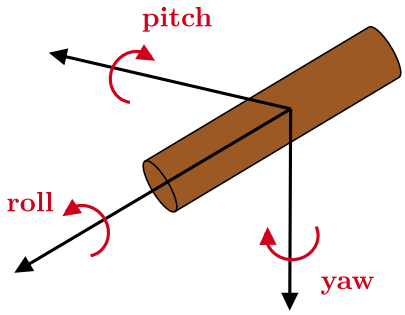

Figure 10: Yaw, pitch and roll representation with a cylinder.

2.3.1 First model

A first model of yaw rotation is presented below. Moire details are given afterwards.

Model by Persi (2015) By denoting $\mathbf{T}_{\text{offset}}$ the offset torque and $\mathbf{T}_{\text{resistance}}$ the resistance torque, the torque balance writes

$$
\begin{aligned}
& I_c \frac{d\omega_c}{dt} = \mathbf{T}_{\text{offset}} + \mathbf{T}_{\text{resistance}} \\
\iff & I_c \frac{d\omega_c}{dt} = \Big[- d_{\text{CP y}} \Big(\frac{1}{2} \rho_w C_d S_p (u_x - v_x) |\mathbf{u} - \mathbf{v}| + \frac{1}{2} \rho_w C_s S_p (u_y - v_y) |\mathbf{u} - \mathbf{v}| \\
& \quad + \rho_w \Big(1 + \frac{1}{2} C_{am} \Big) V_c \frac{D\mathbf{u_x}}{Dt} \Big) \\
& \quad + d_{\text{CP}x} \rho_w \Big(\frac{1}{2} C_d S_p (u_y - v_y) |\mathbf{u} - \mathbf{v}| + \frac{1}{2} C_s S_p (u_x - v_x) |\mathbf{u} - \mathbf{v}| \\
& \quad + \rho_w \Big(1 + \frac{1}{2} C_{am} \Big) V_c \frac{D\mathbf{u_x}}{Dt} \Big) \Big] \\
& \quad + \Big[\frac{1}{8} \rho_w C_{\text{res}} L_c^2 V (\boldsymbol{\omega}_w - \boldsymbol{\omega}_c) |\boldsymbol{\omega}_w - \boldsymbol{\omega}_c| \Big],
\end{aligned}
\tag{45}
$$

with $\boldsymbol{\omega_c}$ and $\boldsymbol{\omega_w}$ the angular velocity of the cylinder and the water, $\mathbf{v}$ linear velocity of the cylinder, I_c its momentum of inertia, S_p its projected area, L_c its length, V_c its volume, C_d, C_s, C_{res} and C_{am} the drag, side, resistance and added mass coefficients, d_{CP} the distance between the center of pressure and the center of mass of the cylinder, ρ_w the fluid density and the subscript x and y for the x-component and the y-component.

This model involves the computation of two torques: an offset torque and a resistance torque.

To grasp the concept of the offset torque, denoted as $\mathbf{T}_{\text{offset}}$, it is essential to recall the notion of the center of pressure. As briefly elucidated in the translation section, the inclination of a non-symmetric object in a flow leads to a displacement of the center of pressure due to a varied pressure distribution around the object. Since this point corresponds to the application point of hydrodynamic forces, it induces a torque. Indeed, a lever arm, d_{CP}, exists between the center of mass (center of rotation) and the center of pressure (point of force application). This is more detailed in 2.3.3. The most often used model for d_{CP} is the one proposed by Yin et al. (2003) that states

$$\frac{d_{CP}}{L_c} = \left| 0.25\cos^3(\theta_{u-v}) \right|. \tag{46}$$

Indeed, this expression allows for extrema (which consequently lead to equilibrium positions) for cylinders aligned or perpendicular to the flow. A specific section is provided below to elaborate on the center of pressure theory.

Regardless, the torque resulting from this displacement of the point of force application is the **T**offset. In light of the discussion about the drag and side force model, it is evident that if the components in the $\mathbf{e}x$ and $\mathbf{e}y$ directions of d_{CP} are designated as dCP x and dCP y, applying the torque definition to the translation equation Eq.(23) yields the expression stated in the model.

The second type of torque experienced by the cylinder is more subtle. The resistance torque, $\mathbf{T}_{\text{res}}$ is defined by Mandø and Rosendahl (2010) as the integral of the friction caused by the rotation itself between the cylinder and the water (over the length of the cylinder). Its definition is then

$$\mathbf{T}_{\text{res}} = 2\int_0^{L_C/2} \frac{1}{2}\mathbf{F}_{\text{res}}\, dl, \tag{47}$$

$$= 2\int_0^{L_C/2} \frac{1}{2}\rho_w C_d S_p(\boldsymbol{\omega_w} - \boldsymbol{\omega_c})|\boldsymbol{\omega_w} - \boldsymbol{\omega_c}| l^2\, dl, \tag{48}$$

where $\mathbf{F}_{\text{res}}$ denotes the resistance force, generated by the friction between the cylinder and the water.

The model by Persi (2015) aims to maintain simplicity and linearity. As an initial step, it an adjusted coefficient, C_{res}, requiring calibration. Its writing implies the use of the cylinder's volume V_c. It allows to write

$$\mathbf{T}_{\text{res}} = 2\int_0^{L_C/2} \frac{1}{2}\rho_w C_{\text{res}} V_c(\boldsymbol{\omega_w} - \boldsymbol{\omega_c})|\boldsymbol{\omega_w} - \boldsymbol{\omega_c}| l^2\, dl. \tag{49}$$

This requires to consider the resistance torque independent from the drag force. Carrying out the integral of the previous equation, it comes the final expression

$$\mathbf{T}_{\text{res}} = \frac{1}{8}\rho_w C_{\text{res}} V_c(\boldsymbol{\omega_w} - \boldsymbol{\omega_c})|\boldsymbol{\omega_w} - \boldsymbol{\omega_c}| L_c^2. \tag{50}$$

At this stage, the stated model is derivable. However, it would not be entirely accurate to rely solely on these explanations. Rigorously, a third type of torque exists, involving cross-terms in the calculation of angular moments and moments of inertia. Nevertheless, since only rotation around the $\mathbf{e}_z$ axis (given by the vector product of the vectors in the previously presented global frame) is considered, and cross angular velocities are assumed to be zero, this term can be disregarded.

2.3.2 Second model

Once again, the model proposed by Ruiz-Villanueva et al. (2014) stands in stark contrast to the one of Persi (2015).

Model by Ruiz-Villanueva et al. (2014)

If the relative position $\mathbf{r}$ of the cylinder edges (numeroted 1 and 2) writes $\mathbf{r}^{(1,2)} = (x^{(1,2)}, y^{(1,2)})$ (with respect to the cylinder center), the new value of the cylinder orientation is computed through

$$\theta'_{u-v} = \arctan\left(\frac{y'^{(2)} - y'^{(1)}}{x'^{(2)} - x'^{(1)}}\right) \tag{51}$$

with $\mathbf{r}'^{(1,2)} = \mathbf{r}^{(1,2)} + h\mathbf{u}^{1,2}$ where h is the time step and $\mathbf{u}^{1,2}$ the flow velocity at each ends, θ_{u-v} the angle bewteen the relative velocity and the major axis of the cylinder.

This model deviates from the mechanics of rotation. Indeed, it simply states that when one end of a cylinder moves faster than the other, it rotates to align more parallel with the flow. To model these changes, velocities at both edges of each cylinder are taken from the flow model. This implies an adiabatic rotation of the cylinder with respect to the flow (no resistance, no inertia).

2.3.3 Center of pressure and the equilibria

The center of pressure refers to the location where the cumulative effect of a pressure distribution on a body results in a net force being applied through that specific point. It is therefore of prime importance to model the distance between the center of mass and the center of pressure, noted d_{CP}. As a reminder, the cylinder is assumed to rotate around its center of mass. The distance d_{CP} then represents the lever arm required to calculate the torques. Reference articles choose Yin et al. (2003)'s formula, but this is not the only model available, although it is the least dated reference. In the following, θ_{u-v} must be expressed in degrees.

The most frequently cited laws are the following. One of the oldest models is the one of Rayleigh (1876), reported in Eq.(52). Initially, the model was computed for an infinite flat plate. It writes

$$\frac{d_{CP}}{L_c} = \left|\frac{0.75\sin(\theta_{u-v})}{4+\pi\cos(\theta_{u-v})}\right|. \tag{52}$$

Then, the work of Marchildon et al. (1964) consisted in approximating linearly the previous law to to predict the center of pressure of a cylinder Eq.(53). However, the authors have established the applicability of this statement for angles of inclination greater than $\theta_{u-v} = 15[^\circ]$, attributing its validity to the consistent uniformity of the pressure distribution beyond this specific angle. The equation writes

$$\frac{d_{CP}}{L_c} = \left|\frac{(90-\theta_{u-v})}{480}\right|. \tag{53}$$

Afterwards, Rosendahl (2000b) worked on the expression reported in Eq.(54).

$$\frac{d_{CP}}{L_c} = \left|0.25\left(1-\sin^3(\theta_{u-v})\right)\right|. \tag{54}$$

Finally, the one of Yin et al. (2003) is reminded and expressed as

$$\frac{d_{CP}}{L_c} = \left|0.25\cos^3(\theta_{u-v})\right|. \tag{55}$$

These equations are initially defined within the range of 0 to 90 degrees, and their extension to cover the entire range of 0 to 360 degrees involves replicating their patterns, as represented in Fig.(11).

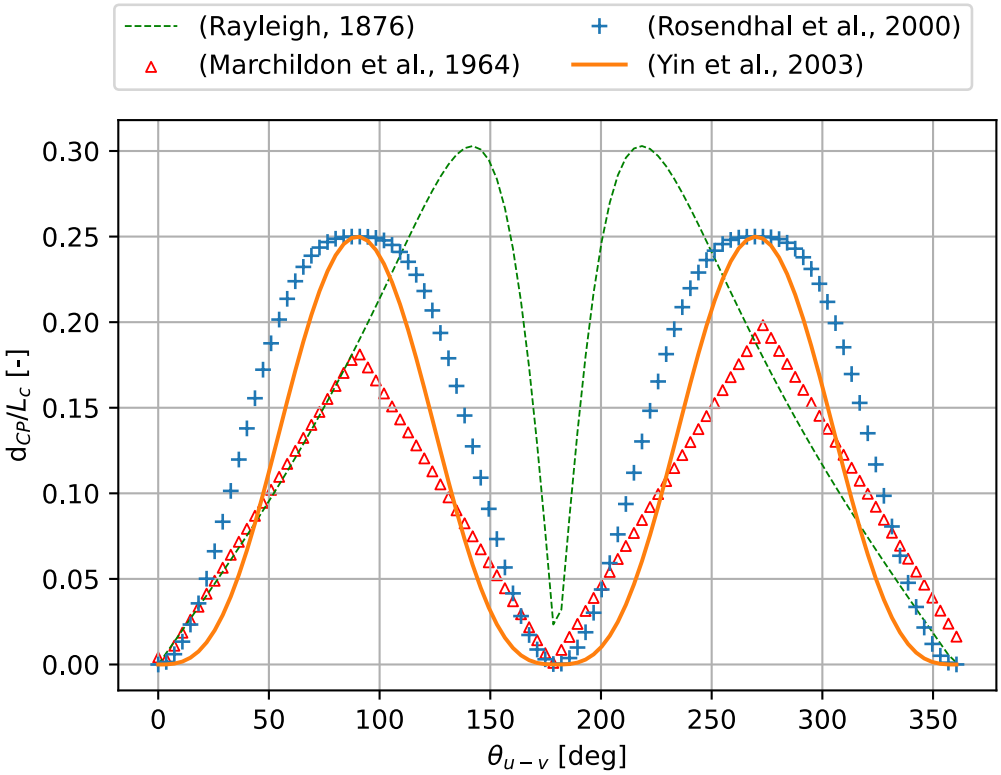

Figure 11: The different model of distance between the center of mass and the center of pressure (normalized with the cylinder's length).

The consideration of the sign remains a necessary step. Indeed, the expressions must remain stated in absolute values to represent a positively signed distance. This sign and the direction of the hydrodynamic forces as discussed in the translation section, result in a torque that force the cylinder to align itself with the flow direction. Fig.(12) illustrates the outcome of this sign analysis. A consistent trend is observed across all models regarding extrema. Experiments in the field of aeronautics have shown that the maximum of these functions occurs at a quarter of the total length of the studied object Mandø and Rosendahl (2010).

The laws of Rosendahl (2000b) and Yin et al. (2003) appear to be the most appropriate. Given the information from the previous paragraph and the fact that stable equilibrium is achieved at 0[°] and unstable at 90[°], it indeed seems prudent to favor the Yin et al. (2003)'s law. In this law, the maxima are encompassed by smaller angular intervals (the peaks of the maxima are "narrower") than those of the minima, in contrast to Rosendahl (2000b). The reverse reasoning holds true for the minima. Since stable equilibrium is at 180[°] ($\pm$180[°]), it can be advantageous to have small values of d_{CP} (which represents the lever arm) around these angles, aiming to minimize torque and prevent excessive rotation of the cylinder.

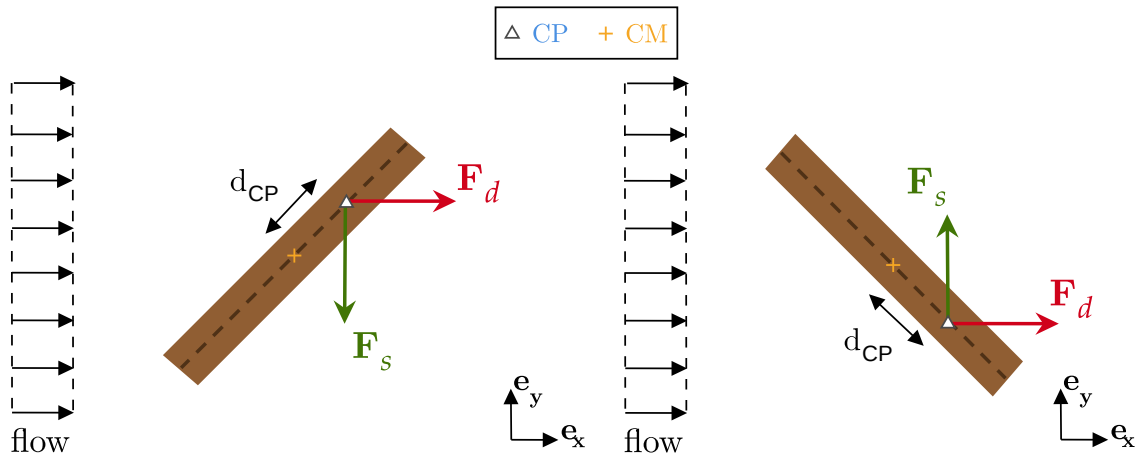

Figure 12: Illustration of the position of the center of pressure and the direction of hydrodynamic forces resulting in a torque forcing the cylinder to align itself with the flow.

As a final remark, the literature often reports the law without specifying the angle in question, which can lead to misinterpretation. Indeed, some articles such as Persi et al. (2020) and Mandø and Rosendahl (2010) refer to the θ_{uv} angle with a 90[°] shift. For these articles in particular, the angles shown in the laws are those measured in relation to the vertical y (corresponding to the width of the channel).

2.4 Collisions

The two models of the reference article are presented below. The study is divided into two parts: detection and correction.

2.4.1 First model

As before, the first model to be described is the model of Persi (2015).

Detection

The model gives no information on the practical aspects of detecting a collision between the cylinder and an obstacle. On the other hand, the model is well documented for collisions between two cylinders., although this is not relevant to the present work.

Correction

Persi (2015)'s collision model is based entirely on Hecker (1997)'s model. Even if this model is intended to be general, the latter is referenced to as a cylinder in view of the present context of application. The element on which the cylinder collides is defined as an *obstacle*.

Model by Hecker (1997)
Let denote by an apostrophe $(\cdot')$ the quantity corrected and ϵ the restitution coefficient. If a collision between the cylinder and an obstacle occurs, then

$$\begin{cases} \mathbf{v_x}' &= \mathbf{v_x} + J\dfrac{\mathbf{n_x}}{m_c}, \\ \mathbf{v_y}' &= \mathbf{v_y} + J\dfrac{\mathbf{n_y}}{m_c}, \\ \omega_c' &= \omega_c + J\dfrac{\mathbf{r}\times\mathbf{n}}{I_c}, \end{cases} \tag{56}$$

where J the impulse momentum [kg ms^{-1}] is computed as

$$J = -(1+\epsilon)\mathbf{v}\cdot\mathbf{n}\left(\frac{1}{m_c} + \frac{(\mathbf{r}\cdot\mathbf{n})^2}{I_c}\right)^{-1}, \tag{57}$$

with $\mathbf{n}$ the obstacle unit vector ($\mathbf{n} = (\mathbf{n_x}, \mathbf{n_y})$), $\mathbf{r}$ the vector from the center of mass of the cylinder and the point of impact, $\mathbf{v}$ the linear velocity of the cylinder, ω_c its angular velocity and I_c the moment of inertia of the cylinder.

To obtain the previous model, the hypothesis of rigid, infinitely heavy obstacle is made. As mentioned earlier, only object-obstacle collisions are considered. Afterwards, the "Newton's law of restitution for instantaneous collisions with no friction", detailed by (Hecker, 1997), is employed.

The notion of impulse must be introduced. In order to prevent the cylinder from penetrating the obstacle, it is essential to bring about an *immediate* alteration. As force cannot instantaneously change velocity due to the time it takes, this situation gives rise to the need of a concept: the impulse Hecker (1997). Introducing this notion leads to disruptions in both the linear and angular velocities of the object. In addition to the previously assumed hypothesis of an undeformable and unbreakable object, the assumption that there is no friction at the point of collision is made. This implies that the collision impulse is entirely normal, with no tangential component Hecker (1997).

The expression in Eq.(57) of the impulse J requires the definition of the restitution coefficient ϵ. The latter is defined as

$$\epsilon = \frac{|\mathbf{v_c'}|}{|\mathbf{v_c}|}, \tag{58}$$

where $\mathbf{v_c'}$ (resp. $\mathbf{v_c}$) is the cylinder's velocity after (resp. before) the collision. This non-dimensional number can vary between 0 (perfectly inelastic collision) and 1 (perfectly elastic collision). In a perfectly inelastic collision, the colliding objects remain together after the collision, whereas in a perfectly elastic collision, the objects rebound without any loss of kinetic energy. Persi (2015) studied the coefficient of restitution for wooden cylinders, neglecting friction, and found a value of 0.1 for them.

Howerver, Persi et al. (2017) writes the expression of J as in Eq.(59)

$$J = -(1+\epsilon)\mathbf{v}\cdot\mathbf{n}\left(\frac{1}{m_c} + \frac{(\mathbf{r}\times\mathbf{n})^2}{I_c}\right)^{-1}. \tag{59}$$

The difference between Eq.(57) and Eq.(59) is the nature of the product indicated in red. It may be a writing error. Indeed, as J must be a scalar to preserve the vectorial nature of the velocities in Eq.(56). Thus, the scalar product in Eq.(57) seems to be correct.

The calculations in Eq.(56) are fairly straightforward, except for the scalar product, which requires knowledge of the angle between **r** and the normals **n** in the preceding equations.

2.4.2 Second model

Now, Ruiz-Villanueva et al. (2014)'s model is described in terms of detection and corrections.

2.4.3 Detection

Unlike the previous model, this one has a specific collision detection capability. Firstly, collisions are classified. According to the model, there are three types: anchoring, sliding and bouncing. There are no criteria for anchoring, but the criteria for the other two cases are presented below.

Criterion for sliding and bouncing collisions

Let β define the incidence angle between the cylinder and obstacle.

If the object goes beyond the limits of the obstacle walls and β is less than β_{lim}, then the collision is of the sliding type.
If the object goes beyond the limits of the obstacle walls and β is greater than β_{lim}, then the collision is of the boucing type.

Unlike the previous model, this one has a specific collision detection capability. Firstly, collisions are classified. According to the model, there are three types: anchoring, sliding and bouncing.

Anchoring refers to the situation where the cylinder collides with the wall and remains attached. This is the case, for example, with tree trunks whose branches are stuck in a bush. In the scenario where the cylinder becomes anchored (as depicted in Fig.(13)), the driving forces diminish due to the reduction in submerged area. The so called effective driving force is therefore calculated as if it were acting on the part of the cylinder that does not exceed the wall limit. The initial motion conditions are recalculated based on these modified circumstances. However, the article does not give any criteria for determining whether a collision is of this type.

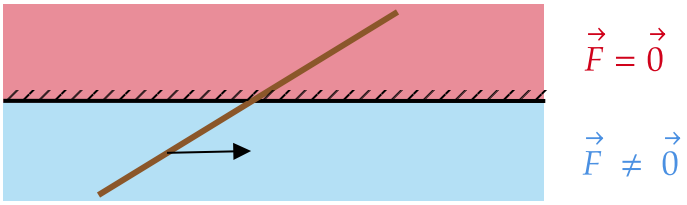

Figure 13: Anchoring case, with the identification of effective driving forces.

The remaining two scenarios refer to collisions as such. If the object does not fall within the aforementioned scenario, it can exhibit two behaviors upon encountering the obstacle: either sliding over it, referred to as *sliding*, or rebounding off it, defined as *bouncing*. The distinction between

the two cases is made via an angle β_{lim}. If the incidence angle is denotec β, then the model predicts that it will bounce beyond the limit angle and vice versa. This model proposes a limit angle of 45[°], based on observations from laboratory experiments. Fig.14) gives a visual summary of the distinction between the two cases, where the cylinder collides with a horizontal obstacle in bouncing way.

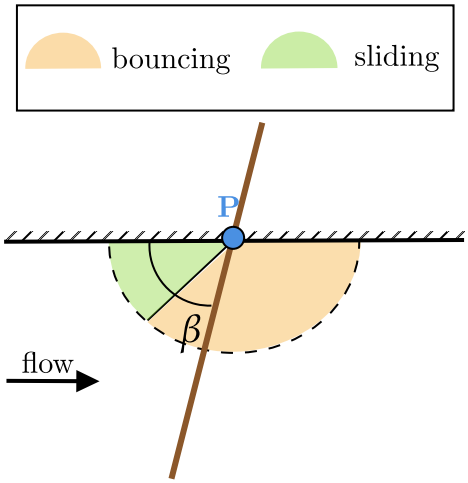

Figure 14: Distinction between sliding and bouncing for a 45[°] angle limit, with an example of a cylinder in a bouncing collision.

2.4.4 Corrections

In addition to detection, corrections must be made to respect the physics involved. To do this, this model proposes a two-stage correction: a purely geometric correction of the cylinder's orientation and position, and a correction of its velocities. Moreover, this model suggests correcting only the linear velocities as in Eq.(60).

Model by Ruiz-Villanueva et al. (2014)
Let denote by $\cdot'$ the quantity $\cdot$ corrected and ϵ the restitution coefficient. If a sliding or bouncing collision occurs between the cylinder and an obstacles, then

$$\mathbf{v_c'} = -\epsilon \mathbf{v_c}, \tag{60}$$

with $\mathbf{v_c}$ the linear velocity of the cylinder. In addition, geometrical corrections are brought.

In contrast to the previous model, the Newton's law of restitution is not applied. Instead of that, the correction applied is calculated as if the cylinder collided perpendicularly with the obstacle. In this model, elastic collisions are considered, so that $\epsilon = 1$. Moreover, no correction is directly brought to the angular velocity, nor the orientation of the cylinder. Instead of that, geometrical corrections are applied as explained below.

To closely simulate the sliding behavior, a geometric correction is employed by using the non-colliding edge of the cylinder as the pivot point for a rotation by an angle λ such that the final position of the colliding edge aligns with the wall. The purpose of Fig.(15) is presented to elucidate this process through a diagram. The pivot point is indicated in red, as well as the rotation.

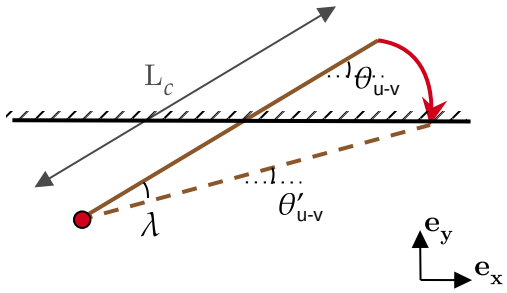

Figure 15: Geometrical sliding correction (in red).

The bouncing geometrical correction consists in a simple translation, in the normal direction of the obstacle, so that the colliding edge is brought back on the wall of the obstacle. In this way, the cylinder's integrity is preserved as depicted in Fig.(16).

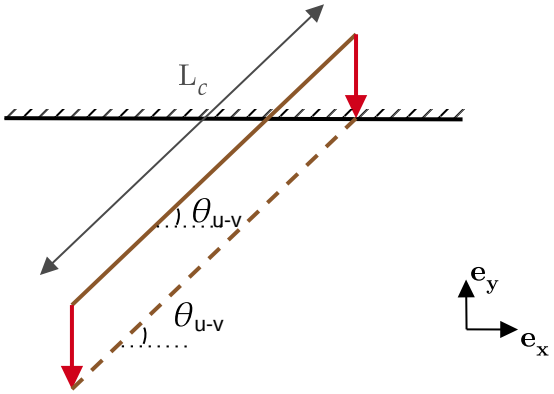

Figure 16: Geometrical bouncing correction (in red).

2.5 Subdivision procedure

The model by Persi (2015) suggest a rewriting to enable a more accurate assessment of forces through a method called subdivision. This model is presented below and subsequently described.

Model by Persi (2015) rewritten with subdivision

Translation model

$$\begin{aligned}\left(\rho_c V_c + C_{am}\rho_w V_w\right)\frac{d\mathbf{v}}{dt} &= \sum_{n=1}^{N}\frac{1}{2}\rho_w C_D S_p^{(n)}(\mathbf{u}^{(n)}-\mathbf{v}^{(n)})|\mathbf{u}-\mathbf{v}| \\ &+ \sum_{n=1}^{N}\frac{1}{2}\rho C_S S_p^{(n)}(\mathbf{u}^{(n)}-\mathbf{v}^{(n)})|\mathbf{u}-\mathbf{v}|\times\mathbf{n}_z \\ &+ \rho_w\left(1+\frac{1}{2}C_{am}\right)\sum_{n=i}^{N}\frac{D\mathbf{u}^{(n)}}{Dt}. \end{aligned} \tag{61}$$

Rotation model

$$\begin{aligned} I\frac{d\boldsymbol{\omega}_c}{dt} &= \Big[-\sum_{n=1}^{N} d_{\mathrm{CP\,y}}^{(n)}\Big(\frac{1}{2}\rho_w C_d^{(n)} S_p^{(n)}(u_x^{(n)}-v_x^{(n)})|\mathbf{u}^{(n)}-\mathbf{v}^{(n)}| \\ &+ \frac{1}{2}\rho_w C_s^{(n)} S_p^{(n)}(u_y^{(n)}-v_y^{(n)})|\mathbf{u}^{(n)}-\mathbf{v}^{(n)}|\Big) \\ &+ \sum_{n=1}^{N} d_{\mathrm{CP}x}\rho_w\Big(\frac{1}{2}C_D^{(n)} S_p^{(n)}(u_y^{(n)}-v_y^{(n)})|\mathbf{u}^{(n)}-\mathbf{v}^{(n)}| \\ &+ \frac{1}{2}C_s^{(n)} S_p^{(n)}(u_x^{(n)}-v_x^{(n)})|\mathbf{u}^{(n)}-\mathbf{v}^{(n)}|\Big)\Big] \\ &+ \Big[\frac{1}{8}\rho_w C_{\mathrm{res}} L_c^2 \sum_{n=1}^{N} V^{(n)}(\boldsymbol{\omega}_w-\boldsymbol{\omega}_c^{(n)})|\boldsymbol{\omega}_w-\boldsymbol{\omega}_c^{(n)}|\Big]. \end{aligned} \tag{62}$$

with N the number of subdivided parts, $\boldsymbol{\omega_c}$ and $\boldsymbol{\omega_w}$ the angular velocity of the cylinder and the water, $\mathbf{v}$ linear velocity of the cylinder, I_c its momentum of inertia, S_p its projected area, L_c its length, V_c its volume, C_d, C_s, C_{res} and C_{am} the drag, side, resistance and added mass coefficients, d_{CP} the distance between the center of pressure and the center of mass of the cylinder, ρ_w the fluid density and the subscript x and y for the x-component and the y-component.

When considering large objects, as the cylinders in this work, the evaluation of the force as a real challenge. Indeed, in scenarios involving non-uniform flow and a relatively larger object compared to flow fluctuations, discrepant velocities in distinct sections of the object can emerge. Calculating forces exclusively at the object's center of mass may inadequately represent the actual force distribution. As the Lagrangian approach is based on the force balance and that they depend on the flow velocity, it is of prime importance to find a model to evaluate the force precisely. To address this challenge, a proposed solution by Persi et al. (2017) involves implementing a subdivision procedure.

The proposed method involves dividing the cylinder N parts, as depicted in Fig.(17) for $N = 1, 3$ and 4.

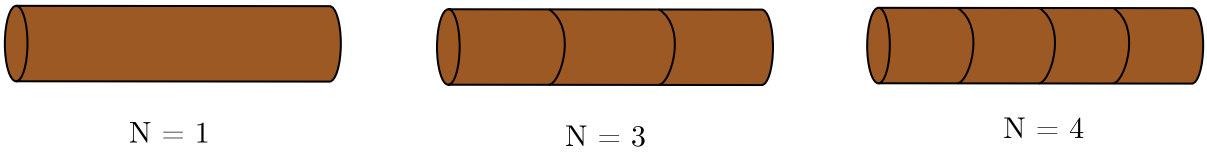

Figure 17: Subdivision of the cylinder for N=1,2 and 3.

The equivalent properties of the sub-cylinders are then computed. In each of these parts, the various forces are evaluated separately using the flow speed at the local center of mass. Then, the total force is evaluated by summing the sums of these different parts. Fig.(18) represents the two previous steps. The intensities are arbitrarily shown different for each sub-section to schematically show the impact that the fluid velocity field might have. On the left, the force evaluation locally and the on the right the total force computed and acting in the center of pressure of the whole body. Particularly for torques, they are evaluated via the local lever arm, i.e. the distance between the local center of mass and the local center of pressure. Finally, linear and angular acceleration are calculated as before.

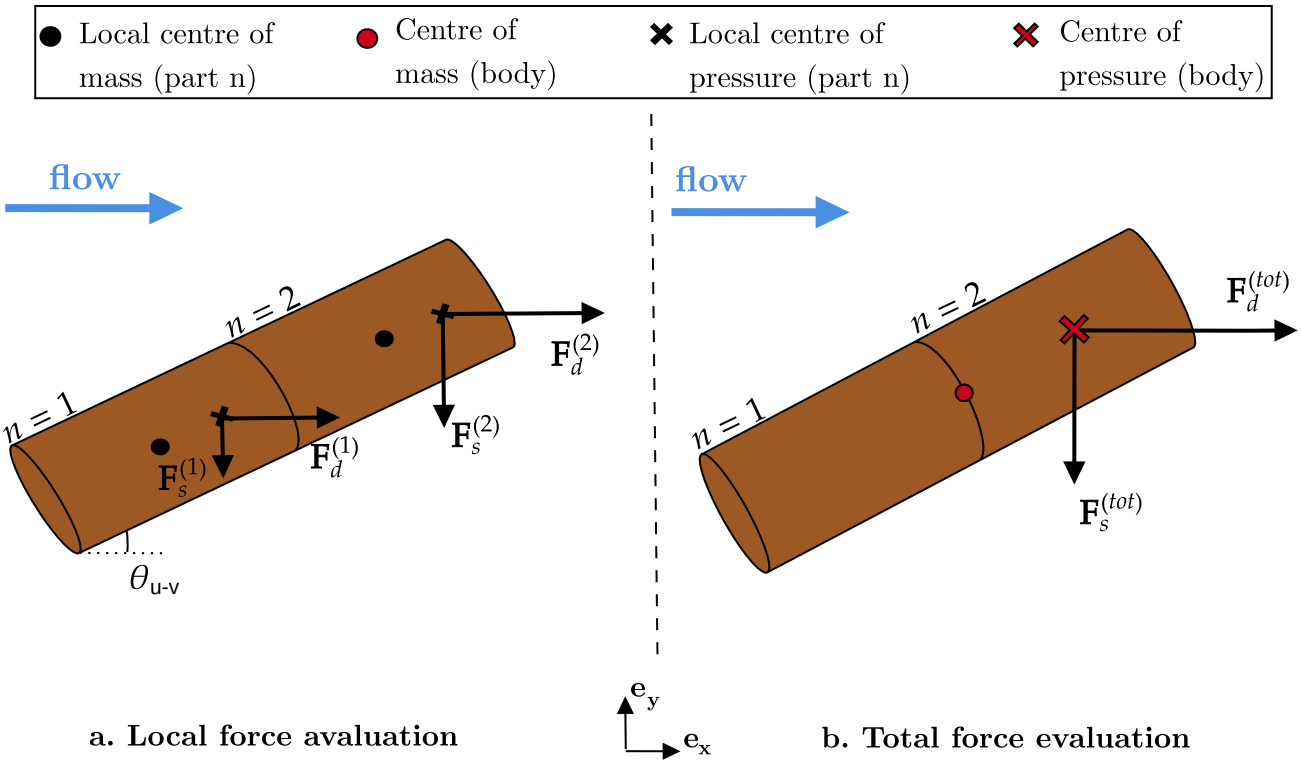

Figure 18: Evaluation of the total force through the subdivision procedure.

Part II
Developed physical model

The goal of Part II is to present the model developed in this thesis, which aims to capture the dynamics of floating objects, handle collisions, and be adaptable for laboratory scenarios, while remaining potentially applicable to real-world cases. This description is divided into two parts: the dynamic model and the collision model. Each part is elaborated both theoretically and numerically, providing a comprehensive understanding of the model's principles, its practical implementation and first results. In particular, the simulations that are presented are performed under the assumption of a uniform and stationary field. Indeed, the generation of more complex flows in line with reality requires an Eulerian study and is addressed in the following section.

1 Introduction to the model

1.1 Overall description of the model

As an introduction to the model, the overall structure of the implemented algorithm is outlined. The code development enables a hierarchical organization of necessary calculations and the progressive evolution of computations to predict the behavior of a floating object. This approach is chosen due to its ability to facilitate the prediction of floating object dynamics effectively. The Fig.(19) summarizes the general structure of the code.

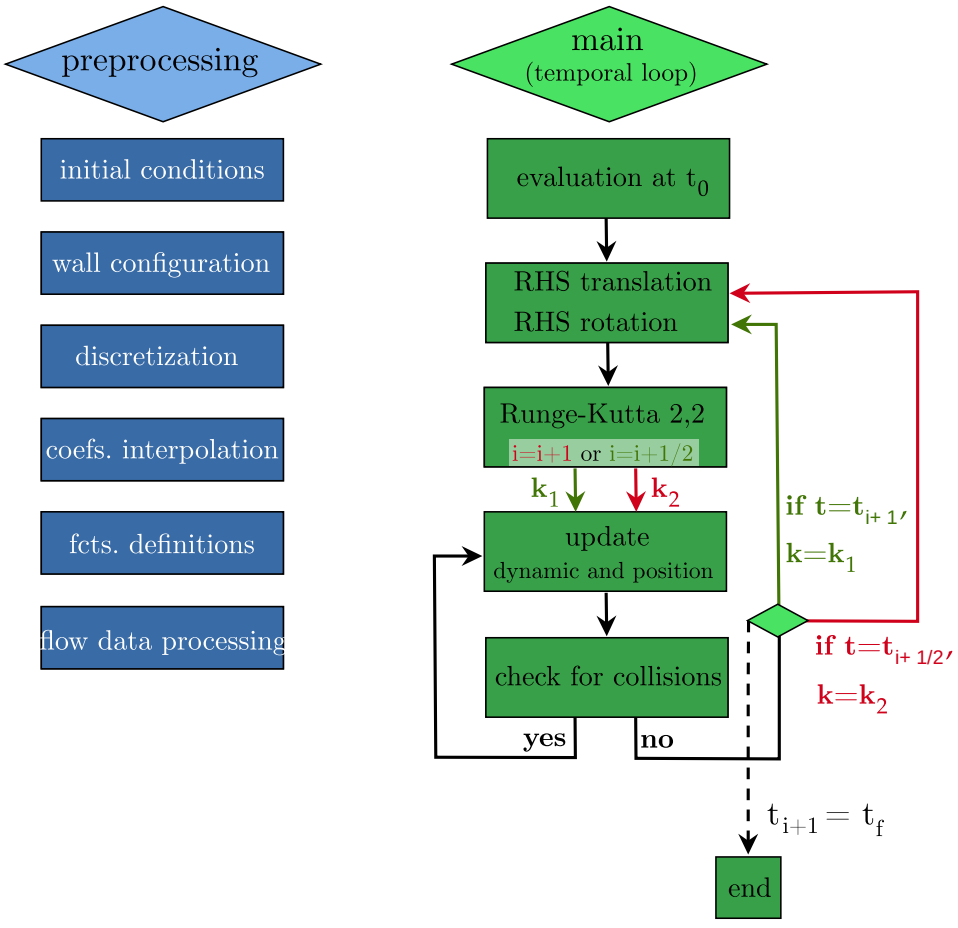

Figure 19: Diagram description of the Python algorithm.

Whether examined from a numerical or theoretical perspective, the modeling process requires a set of input data, such as terrain knowledge (***wall configuration***), calibration of ***coefficients***, and most importantly, ***initial conditions***. Once these aspects are defined, a unique solution can be computed from the equations. From a purely implementation point of view, the preprocessing needs the definitions of the ***functions*** needed, the treatment of the ***data flow*** and an ***interpolation*** of the hydrodynamics coefficients found in literature.

After establishing the ***initial state***, the formulation of equations governing the evolution of key variables, namely linear and angular velocity and the inclination angle, is conducted. These equations encompass the necessary forces for constructing force balances (fundamental dynamic's law). They must describe the object's dynamics in terms of both **rotation and translation**. Subsequently, this system of differential equations is resolved over time. To accomplish this, a second-order ***Runge-Kutta 22*** method (order 2, two iterations) is employed.

During the resolution process, ***collision*** detection and correction is studied at each sub-time step, in order to improve accuracy. Considering the simulation of a single wooden trunk, the model examines object-wall or object-obstacle collision scenarios. In the absence of detected collisions, the Runge-Kutta resolution continues without interruption. However, if a collision is detected, adjustments are made to closely approximate the underlying physics of the collision event. At the end of the second Runge-Kutta step, solutions for the next time step are derived, owing to the method's explicit nature. This loop persists until the final simulation time is reached. Upon completion, the linear and angular velocity and the object's orientation, enable the calculation of its trajectory and visualization within the studied configuration.

1.2 Comparison of the model with the literature

The points of comparison in Part 1 are applied to the current model, to highlight the differences and similarities that exist. As a reminder, the elements of comparison and sub-elements of comparison are explained below. The convention is similar to Part 1: blue means the criterion is covered and white the opposite.

Flow hypothesis

- ▷ **Turbulence model**: presence or absence of a turbulence model;
- ▷ **Unsteady**: variation of fluid velocity with time;
- ▷ **Uniform**: no spatial dependence of the velocity field;
- ▷ **Field**: consideration of real-life situations in the simulations.

Drifting shape

The simulated drifting object (spheres, disks or cylinders).

Data

The source of the data used (from experiments or simulations).

Phenomena

- ▷ **Added mass**: added mass term has added to the equations;
- ▷ **Density cases**: whether different density cases have been treated (fully/partially submerged);

▷ **Entrainment**: the entrainment of a tree trunk (typical debris) initially hanging or present on the ground.

Motion

Component of the motion (translation or yaw rotation) studied.

Forces

- ▷ $\mathbf{F}_d$: component of the hydrodynamic in the direction of the relative velocity, called the drag force;
- ▷ $\mathbf{F}_s$: component of the hydrodynamic force in the perpendicular direction of the relative velocity, called the side force;
- ▷ $\mathbf{F}_g$: effective weight of the object in the downstream direction the weight, called the effective weight;
- ▷ $\mathbf{F}_f$: the friction force between the object and the flume's bed;
- ▷ $\mathbf{F}_p$: the force that the fluid would exert on the body if the presence of the body had not disturbed the flow called the Froude-Krylov force;
- ▷ $\mathbf{F}_{am}$: the force related to the additional inertia of the fluid surrounding the object, called the added mass force.

Collision

- ▷ **detection** : detection model elaborated and available;
- ▷ **geometrical** correction : correction model based on geometrical correction;
- ▷ **dynamic correction** : correction model based on dynamic correction;
- ▷ **obstacle model** : debris representation model elaborated and available;
- ▷ **clogging prediction** : model able to simulate and detect clogging;
- ▷ **clogging experimental** : laboratory clogging experiment;
- ▷ **clogging simulation** : numerically simulated clogging event.

The comparative table is given in the Tab.(6). The main differences are as follows. The model developed is less general in terms of flow than the literature. Indeed, it is limited to hypothetical flows (uniform and unsteady) and real flows (unsteady). It represents the simplest shape closed to a tree trunk, typical debris in flood events. Experimental data from Ruiz-Villanueva et al. (2014) are be simulated, even if the experiments were not carried out as part of this work. About the phenomena, the presence of the debris is assumed and its density is fixed, allowing us to get rid of the different cases of density (e.g. in terms of coefficient). For the force model, Persi (2015)'s model is followed, with the addition of certain forces taken into account by Ruiz-Villanueva et al. (2014). The developed models brings new elements breaks new ground when it comes to collisions. It satisfies all the sub-components of the comparison except the clogging experiment, since this work is limited to simulation. All these choices are justified throughout this part 2.

Elements of comparison	Sub-elements of comparison	(Ghaffarian et al., 2020)	(Ruiz-Villanueva et al., 2014)	(Persi, 2015)	The developed model (Part II)
Flow hypothesis	turbulence model				
	unsteady				
	field				
Drifting shape	sphere				
	disk				
	cylinder				
Data	experimental				
	simulated				
Phenomena	entrainement				
	added mass				
	density cases				
Motion	translation				
	yaw rotation				
Forces	$\mathbf{F}_d$				
	$\mathbf{F}_s$				
	$\mathbf{F}_g$				
	$\mathbf{F}_f$				
	$\mathbf{F}_p$				
	$\mathbf{F}_{am}$				
Collision	detection				
	geometrical correction				
	dynamic correction				
	obstacle model				
	clogging prediction				
	clogging experimental				
	clogging simulation				

Table 6: General comparison between the literature and the developed model.

2 Dynamic model

A Lagrangian description studies the motion of a body by focusing on the individual trajectory of each particle making up that body. It offers a powerful approach to analyzing the behavior of floating debris in rivers, providing detailed information on its trajectory, velocity, acceleration and interaction with the surrounding fluid.

Adopting a Lagrangian perspective, each piece of floating debris is considered as a separate entity, and its evolution over time is tracked using coordinates relative to its own position and that of the surrounding fluid. The global and local frames are the same as the one defined in the literature, represented previously in Fig.(2).The adopted dynamic model is described below.

2.1 Floating object and flow hypothesis

The object of interest in this work are cylinders. Indeed, as studied in the literature review, the cylinder is the most studied object in the study of debris drift. In addition, the model operates under some **assumptions**. The cylinder is assumed to be perfectly rigid, homogeneous and unbreakable. In addition, ihe initiation of debris motion is extensively studied in litterature Persi (2015). As the model aims to be used during intense rainfall events, the necessary conditions to carry away debris are supposed met.

For all the simulations of this section, the geometric and physical characteristics shown in Tab.(7) have been applied. They have been implemented in the function `type_macro` in the algorithm. In particular, a semi-floating cylinder is simulated to closely adhere to the assumptions found in the literature, especially for the calibration of the drag and side coefficients Persi (2015).

r_c [m]	L_c [m]	ρ_c [kg/m^3]	ρ_w[kg/m^3]
0.25	3	500	1000

Table 7: Properties of the wooden cylinder utilized in the simulations of section II.

In terms of flow, only unsteady flows are considered. In the first simulation phase, uniform fields are used, and then non-uniform fields taken from literature experiments are simulated.

2.2 Movement equations

The basic model used is the one of Persi (2015) in Eq.(61). This choice is based on the desire to work with a model close to a classic mechanical description of the floating debris.

2.2.1 Translation

Under the hypothesis of this work, Eq.(61) rewrites as Eq.(63).

Developed model for translation, adapted from Persi (2015)

$$\begin{aligned}\left(\rho_c V_c + C_{am}\rho_w V_w\right)\frac{d\mathbf{v}}{dt} = &\sum_{n=1}^{N}\frac{1}{2}\rho_w C_D S_p^{(n)}(\mathbf{u}^{(n)}-\mathbf{v}^{(n)})|\mathbf{u}-\mathbf{v}| \\ &+\sum_{n=1}^{N}\frac{1}{2}\rho C_S S_p^{(n)}(\mathbf{u}^{(n)}-\mathbf{v}^{(n)})|\mathbf{u}-\mathbf{v}|\times\mathbf{n}_z \\ &+\rho_w\left(1+\frac{1}{2}C_{am}\right)\sum_{n=i}^{N}\frac{D\mathbf{u}^{(n)}}{Dt}. \end{aligned} \tag{63}$$

with N the number of subdivided parts, $\mathbf{v}$ the linear velocity of the cylinder, $\mathbf{u}$ the flow velocity, m_w the displaced fluid mass, m_c the cylinder mass, V_c its volume, S_p its projected area, ρ_w the fluid density C_d and C_s the drag and side coefficients, $\mathbf{n}_z$ the unit vector normal to the 2D flow plane and $\frac{D}{Dt}$ the convective derivative equal to $\frac{\partial}{\partial t}+\mathbf{u}\cdot\boldsymbol{\nabla}$.

The model with the subdivision was chosen, as one of the aims of this work is to develop an algorithm capable of handling real flow data. For this reason, the cylinder was previously assumed to be homogeneous.

The hydrodynamic coefficient used are the one presented in the sub-subsection 2.2.3, calibrated by Persi (2015). However, a model for its dependence in the particle Reynolds number must be developed. As a reminder, three regimes were identified : the Stokes', the Newtonian's and the drag crisis' regime.

The developed function is defined by part and is designed to take physical phenomena into account. Thus, for the Stokes Regime, the law proposed in the literature $24/Re_p$ is applied without modification. Then, in the Newtonian regime, experiments show that the coefficient depends only on theta, so the function becomes constant over this interval. It is in this regime that the coefficient is equal to the one experimented by Persi (2015) and previously represented in Fig.(9). Finally, the third regime represents the drag crisis, where the coefficient is again constant but with a much lower value of 0.01 Singh and Mittal (2005).

In addition to reflecting physical phenomena, the law is intended to be continuous. Thus, the transitions between regimes have been adjusted. To this end, the first transition between the Stokes and Newton regimes is calculated as an inverse function $1/Re_p$ that tends to the constant value of the Newtonian regime. For the second transition between the Newtonian regime and the drag crisis, a more rapidly decaying function was chosen. For this reason, a function as $1/Re_p^2$ is selected and adjusted to tend to the selected value of 0.01.

The developed model is presented in the graph of Fig.(20). The latter shows the experimental data of Rosendahl (2000a) which were presented in Fig.(8).

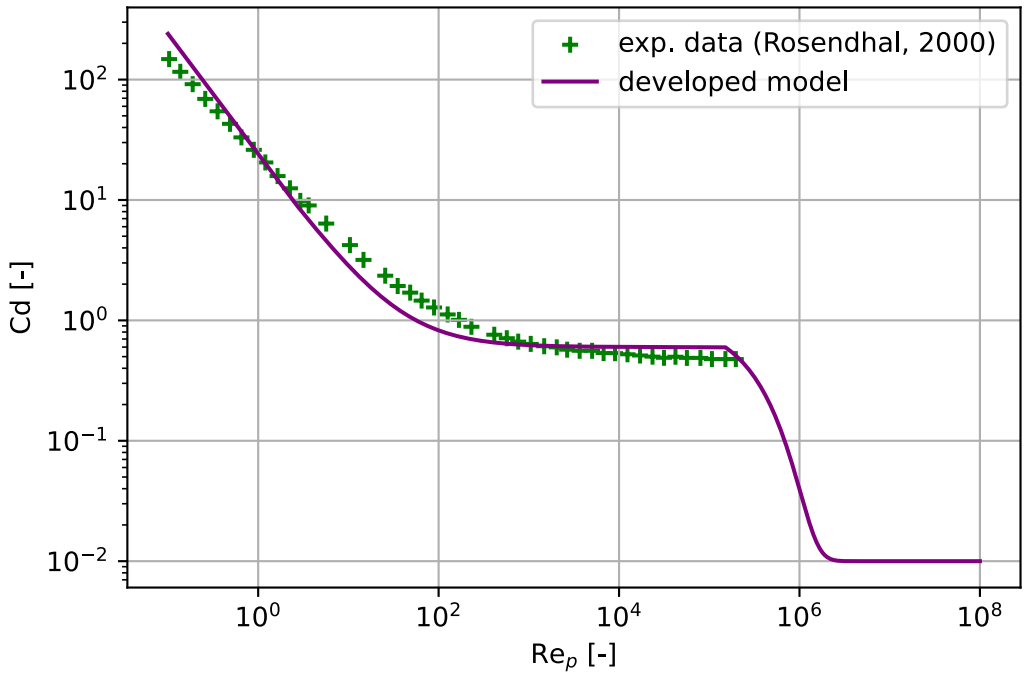

Figure 20: Comparaison of experimental data for the drag coefficient of a cylinder according to Rosendahl (2000a) and the developed model for $\theta = 90[^\circ]$. *exp* stand for experimental.

The Tab.(8) shows the selected intervals.

regimes / function	**Stokes regimes**	**Newtonian regime**	**Drag crisis**
chosen intervals	[0, 10[	[10, 1.5 1e5[	[1.5 1e5, ∞[
developed law	$\mathrm{Cd}(\theta_{u-v}, Re_p) = \mathrm{Cd}(Re_p)$ $\mathrm{Cd}(Re_p) = 24/Re_p$	$\mathrm{Cd}(\theta_{u-v}, Re_p) = \mathrm{Cd}(\theta)$ Persi (2015)	$\mathrm{Cd}(\theta_{u-v}, Re_p) = \mathrm{Cd}(\theta)$ $\mathrm{Cd}(\theta) = 0.01$

Table 8: Developed function for the drag coefficient i, function of Re_p.

An error analysis is performed to evaluate the accuracy of the approximation. To do so, the relative mean square error (RMSE) is used. It is defined as the square root of the average of the squares of differences between two sets of values a_i and b_i, so that

$$\mathrm{RMS} = \sqrt{\frac{1}{N_o}\sum_{i=1}^{N_o}(a_i - b_i)^2} \tag{64}$$

where N_o the number of data in a and b.

Analysis of this error for the approximation is given in the available data range (no in the drag crisis regime). The RMS error equals 30.27 for the Stokes regime. Since experimental coefficients are of the order of a hundred in this regime, the approximation is acceptable. In the transition between the latter regime and the Newtonian one, the RMS error equals 0.5. The level of approximation can be considered moderate since the experimental coefficients are roughly at the unit scale for this interval. Lastly, within the Newtonian regime, the RMS error becomes 0.11. The quality of approximation improves significantly here, given that the experimental coefficients remain constant at 0.6.

2.2.2 Rotation

Then, the model for the rotation is the one Persi (2015) given in Eq.(62) adapted with the hypothesis of the model.

Developed model for yaw rotation, adapted from Persi (2015)

$$
\begin{aligned}
I\frac{d\boldsymbol{\omega}_c}{dt} = \Big[&- \sum_{n=1}^{N} d_{\mathrm{CP\,y}}^{(n)} \Big(\frac{1}{2}\rho_w C_d^{(n)} S_p^{(n)} (u_x^{(n)} - v_x^{(n)}) |\mathbf{u}^{(n)} - \mathbf{v}^{(n)}| \\
&+ \frac{1}{2}\rho_w C_s^{(n)} S_p^{(n)} (u_y^{(n)} - v_y^{(n)}) |\mathbf{u}^{(n)} - \mathbf{v}^{(n)}| \Big) \\
&+ \sum_{n=1}^{N} d_{\mathrm{CP}x}\rho_w \Big(\frac{1}{2} C_D^{(n)} S_p^{(n)} (u_y^{(n)} - v_y^{(n)}) |\mathbf{u}^{(n)} - \mathbf{v}^{(n)}| \\
&+ \frac{1}{2} C_s^{(n)} S_p^{(n)} (u_x^{(n)} - v_x^{(n)}) |\mathbf{u}^{(n)} - \mathbf{v}^{(n)}| \Big) \Big] \\
&+ \Big[\frac{1}{8}\rho_w C_{\mathrm{res}} L_c^2 \sum_{n=1}^{N} V^{(n)} (\boldsymbol{\omega}_w - \boldsymbol{\omega}_c^{(n)}) |\boldsymbol{\omega}_w - \boldsymbol{\omega}_c^{(n)}| \Big]. \qquad (65)
\end{aligned}
$$

with N the number of subdivided parts, $\boldsymbol{\omega_c}$ and $\boldsymbol{\omega_w}$ the angular velocity of the cylinder and the water, $\mathbf{v}$ linear velocity of the cylinder, I_c its momentum of inertia, S_p its projected area, L_c its length, V_c its volume, C_d, C_s, C_{res} and C_{am} the drag, side, resistance and added mass coefficients, d_{CP} the distance between the center of pressure and the center of mass of the cylinder, ρ_w the fluid density and the subscript x and y for the x-component and the y-component.

The adopted model is applied under the following **hypothesis**. First, the cylinder's rotation is limited to the yaw, described earlier in Fig(10). Next, the cylinder's center of rotation is assumed to be its center of mass.

Among the various laws modelling the distance d_{CP} between the center of mass and the center of pressure, Yin et al. (2003)'s model is adopted in view of the reasoning made in the subsubsection 2.3.3.

2.2.3 Subdivision procedure justification

The chosen model are based on Persi (2015)'s models, rewritten under a subdivision model. Indeed, two phases of simulations are planned. The first phase involves a hypothetical unsteady uniform flow that does not require this procedure, and the second phase involves an unsteady and non-uniform real flow. In order capture the most representative flow velocity, this method is necessary to account for spatial variations in velocity along the cylinder. In practice, the spatial domain is discretized, and the flow velocity values at the center of mass of each sub-cylinder ($\mathbf{u}^{(n)}$) is bilinearly interpolated with the velocity values from the nearest cells. Appendix A.3 provides a detailed definition and implementation of this interpolation.

3 Validation for hypothetic flows

The ultimate objective of this section within this segment is the scrutiny of validation instances. To accomplish this, two test are performed : one to check the immobility of the cylinder and the other to verify the robustness of the simulations to flow orientation.

3.1 Temporal resolution and performance

The aim of this short subsection is to briefly explain the code's performance in terms of equation resolution. First of all, for solving the equations, a Runge-Kutta order 2, 2 iterations scheme has been chosen and described in Appendix A.2. Since the focus of this work is not centered around code optimization, but rather on modeling the object, analyzing its collisions, and so forth, this section is intended to be concise. Several simulations with different time steps were performed. These simulations give similar results for time steps of less than 0.01[s].The simulation of this subsection is conducted under the parameters given in Tab.(9).

flow [m/s]	$\mathbf{v_0}$ [m/s]	ω_0 [°/s]	θ_{u-v} [°]	(x_0, y_0) [m]	N [−]	t_{phys} [s]
uniform and stationary $\mathbf{u} = (\mathbf{2}, \mathbf{0})$	(0,0)	0	75	(2,7.5)	1	120

Table 9: Parameters used for the algorithm perfomance tests.

As the algorithm is not optimized, the computation time CT is quite bad, as shown in Fig.(21). What is more, this data is taken without any collision simulations, which slows down code execution even more, given the conditions to be checked. It decreases in an exponential way with the time step h. With this second reason, the value of h=0.01 seems to be a wise choice.

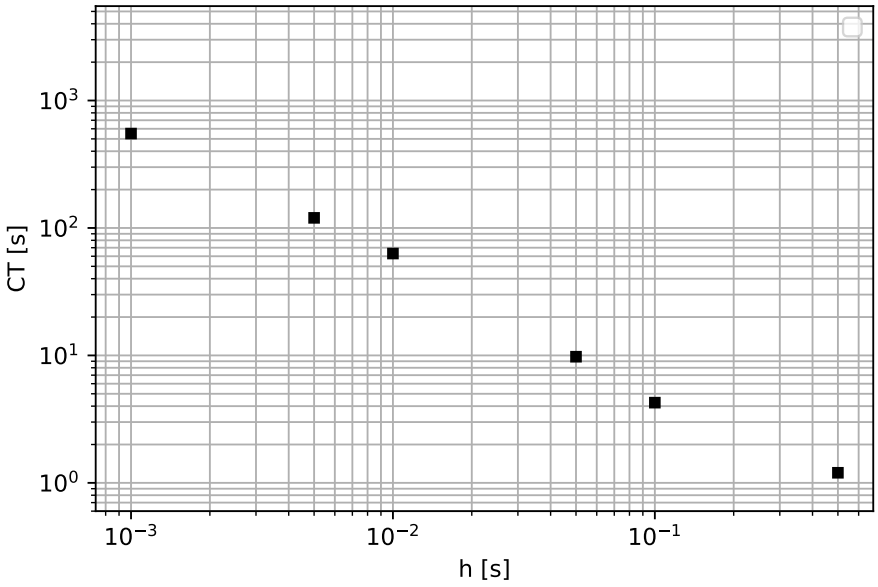

Figure 21: Computation time CT[s] in function of the time step h[s] for 120[s] of physical simulation.

3.2 Object immobility in an inert fluid

This rather straightforward test is of significant importance. It verifies the immobility of an object residing in an inert fluid. The objective here is the detection of any prospective numerical anomalies that might yet instigate movement in the object. The simulation parameters are given in Tab.(10).

flow [m/s]	$\mathbf{v_0}$ [m/s]	ω_0 [°/s]	θ_{u-v} [°]	(x_0, y_0) [m]	N [−]	h [s]	t_{phys} [s]
inert $\mathbf{u} = (\mathbf{0}, \mathbf{0})$	(0,0)	0	15	(2,7.5)	1	0.01	30

Table 10: Parameters used for the "immobility" validation test.

The results are shown in Fig.(22). The quantities remain fixed at their prescribed initial conditions throughout the simulation. This validates the test.

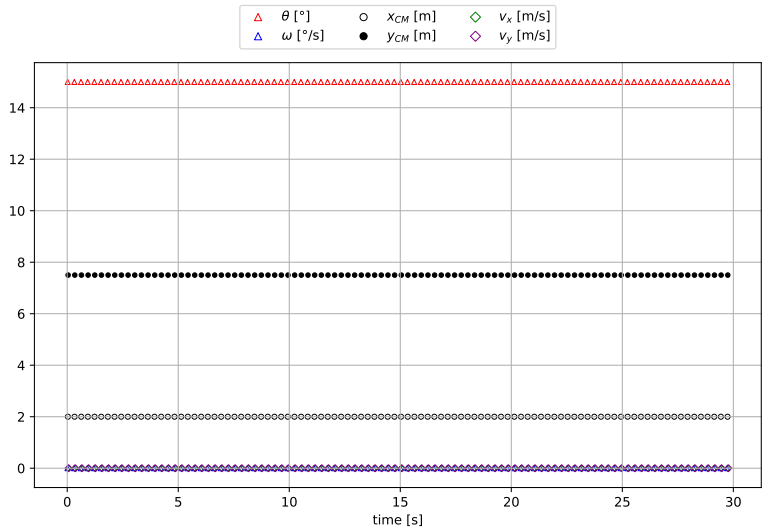

Figure 22: Test for the object immobility in an inert fluid.

3.3 "4-flumes" validation

The "4-flumes" numerical test is a crucial procedure in the verification of this type of simulation code. This methodology aims to guarantee the accuracy of the implementation by assessing the robustness of the model under different conditions. By simulating translation and rotation scenarios in a channel, this approach takes a close look at the object's reactions to hydrodynamic forces and flow-induced torques.

The 4-channel numerical test is developed by running 4 different simulations. For easy visualization of the test, the Fig.(23) shows the 4 possible global frame configurations. These configurations are : bottom-top, top-bottom, left-to-right and right-to-left. However, in the following, the graphs are given in the local frame. This process reveals any potential inconsistencies or sign errors in forces, angles and other parameters influencing the trajectory of the floating object. This test demonstrates the fidelity of the numerical model.

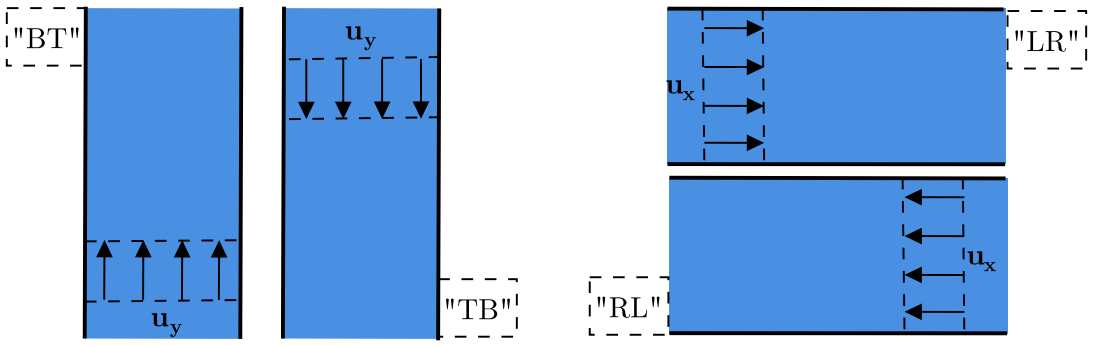

Figure 23: "4-flumes" test configurations in global frames, with uniform stationary flow. Used abbreviations : flow from top to bottom "TB", bottom to top "BT", right to left "RL" and left to right "LR".

In practice, this test is performed under the simulation parameters presented in Tab.(11), given in the local frame. As before, the number of sub-parts N in the cylinder equals 1, since the flow is uniform.

flow [m/s]	$\mathbf{v_0}$ [m/s]	$\boldsymbol{\omega_0}$ [°/s]	θ_{u-v} [°]	N [−]	h [s]	t_{phys} [s]
uniform and stationnary $\mathbf{u} = (\mathbf{2}, \mathbf{0})$	(0,0)	0	45	1	0.01	90

Table 11: Parameters used for the "4-flumes" validation test (local frame).

Graphs of the solutions ($\mathbf{v}$, ω_c and θ_{uv}) are presented in Figs.(24, 25), as well as the trajectory of the center of mass in Fig.(26).

Linear velocities

Linear velocity solutions are given in Fig.(24). One value out of 30 is plotted for greater visibility. This initial test is successful as the 4 different simulations give the same results in local frame.

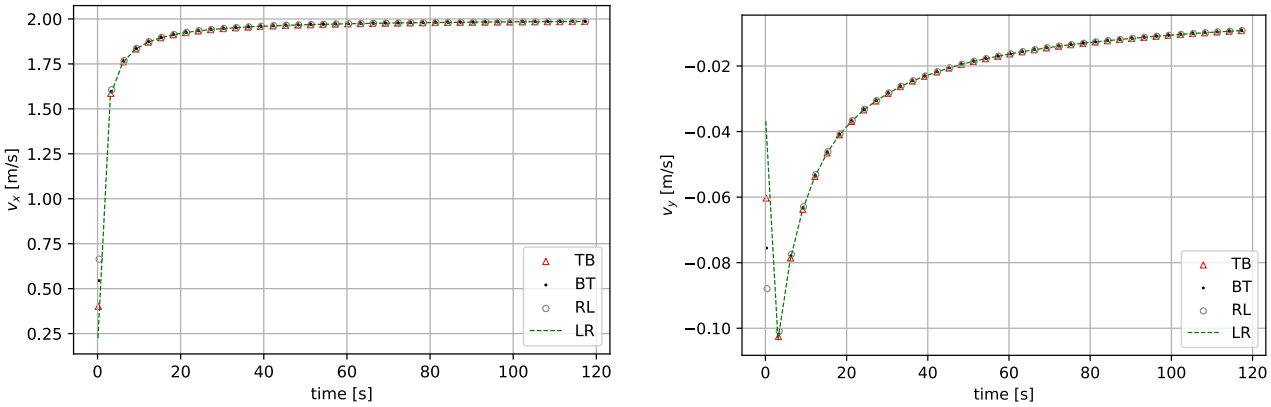

Figure 24: Linear velocity (x-component at the top and y-component at the bottom) of the cylinder versus time for the "4-flumes" test.

Angular velocities and orientation

The test concerning the angular velocity of the cylinder and he evolution of the angle between the major axis of the cylinder and the flow velocity (θ_{uv}) is plotted in Fig.(25). Similar to the previous graph, a value every 30 is plotted to enhance visibility. No data manipulation is performed for this test, as the same convention is employed throughout this work[3]. The curves align perfectly, indicating similar torque signs among the different simulations, as expected to pass the test.

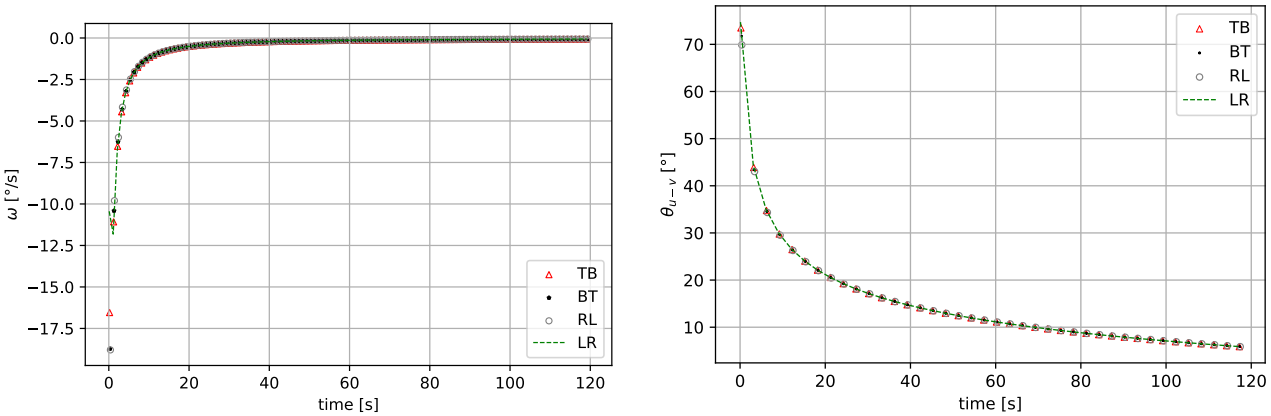

Figure 25: Angular velocity of the cylinder (left) and angle between the major axis of the cylinder and the flow velocity (θ_{uv}) (right) versus time for the "4-flumes" test.

Center of mass trajectory

Lastly, the ultimate test involves comparing the trajectory of the cylinder's center of mass. As translational and rotational motions are coupled through the dependence of forces on velocity and orientation, revealing that the curves exhibit a 'mirroring' effect. Thus, the test is deemed successful.

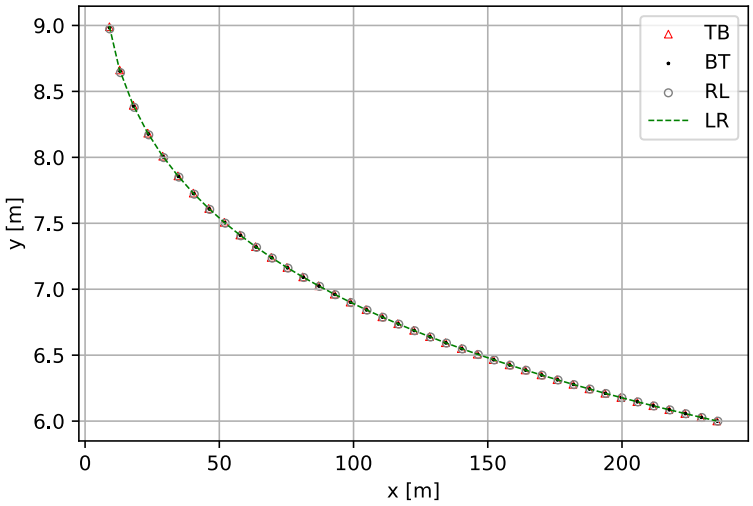

Figure 26: Trajectory comparison of the cylinder's center of mass for the "4-flumes" test.

Discussion

The tests conducted shows the code consistently predicts the dynamics of the floating cylinder across different configurations. This underscores the code's capacity to effectively handle such intricate manipulations, affirming its reliability.

[3] As a reminder, the angular velocity is positive in the trigonometric sense.

3.3.1 Equilibrium verification

The aim is to verify the cylinder's stable (aligned with the flow) and unstable (perpendicular to the flow) equilibrium. The simulations are performed under the parameters of Tab.(12).

flow [m/s]	$\mathbf{v_0}$ [m/s]	ω_0 [°/s]	(x_0, y_0) [m]	N [–]	h [s]	t_{phys} [s]
uniform and stationnary $\mathbf{u} = (\mathbf{2}, \mathbf{0})$	(9,9)	0	(9,9)	1	0.01	120

Table 12: Parameters used for the equilibrium validation test (local frame).

Four simulations are performed, with the initial angle set at 90[°], 95[°], 5[°] and 0[°] as variable parameters. Figs.(27) show the results of angle and angular velocity evolution, sufficient for this study. It can be seen that the angular velocity remains zero for the initial angles of 0[°] and 90[°], showing the character of equilibrium positions.

The hypothetical flow allows to visualize it even for the perpendicular case. This would be impossible with a real flow in which the cylinder undergoes orientation perturbations Mandø and Rosendahl (2010). To force this perturbation, the other two simulations are performed with initial angles equal to 5[°] and 95[°]. It can be seen that for 95[°], angular velocity has a peak at the beginning of the simulation. This is because the torque is maximum, given the position of the center of pressure and the forces acting on it. In fact, the coefficients shown in Fig.(9) combined with the Eq.(55) center-of-pressure law show that the cylinder undergoes maximum torque. This angular velocity tends towards 0 [°/s] as the angle tends towards 180 [°], demonstrating the nature of unstable equilibrium at 95[°] and stable equilibrium at 0[°]. The simulation with an initial angle of 5[°] is less explicit. Indeed, it seems to indicate a zero angular velocity and a constant evolution of theta. In practice, this is not the case. For performance reasons, the simulation stops after 150[s], but it would take longer for the cylinder to return to its equilibrium position. In fact, using Eq.(55) allows excessively low torque around 0[°], especially for 5[°].

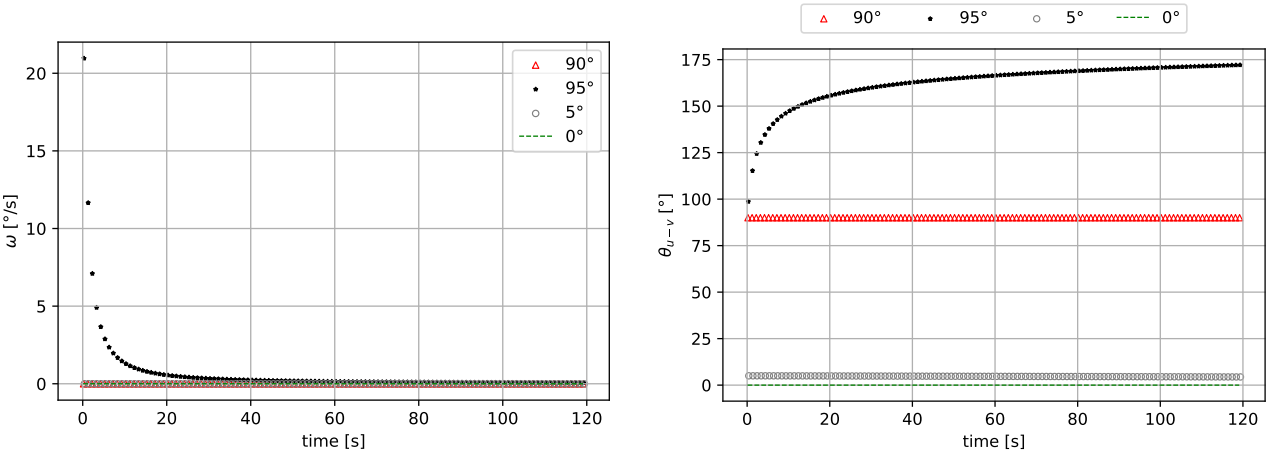

(a) Temporal evolution of ω_C (local frame).

(b) Temporal evolution of θ_{u-v} (local frame).

Figure 27: Evolution of the angular velocity ω_C and of the angle θ_{u-v} for different initial orientation (local frame).

3.3.2 Subdivision verification

Now that the basic dynamics of the floating object have been verified, it is of prime importance to verify that the subdivision has no impact on the object's dynamics for the hypothetical flow. In fact, the same parameters are used as before (Tab.(12)), in which a uniform, stationary flow is used. Thus, each sub-section of the cylinder is surrounded by a same value of the flow velocity. The subdivision and the resulting bilinear interpolation must keep this reality. To do so, the same simulation as before is performed for different number of subdivisions N (1, 2, 5 and 10). First, the Fig.(28) shows the evolution of the angular velocity and the relative angle θ_{uv}. The curves overlap perfectly

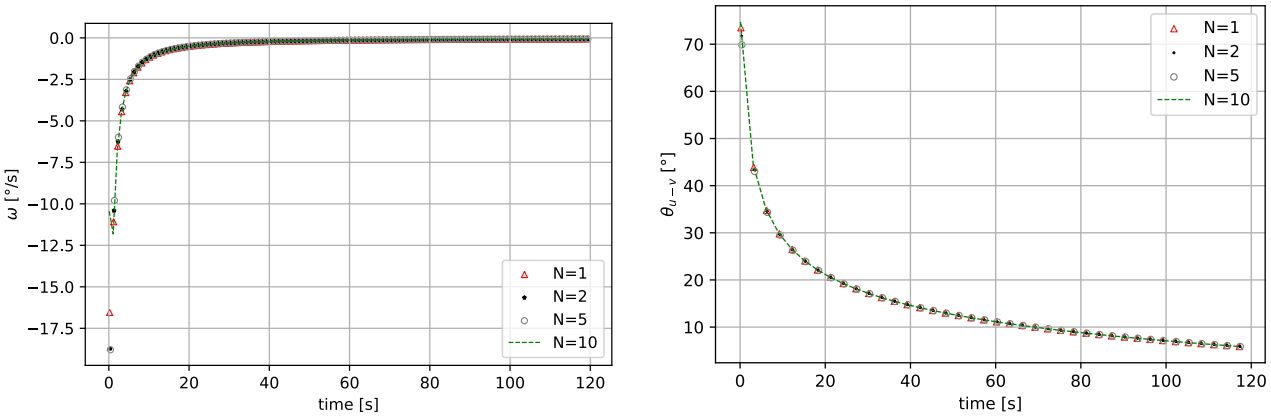

(a) Angular velocity ω_c.

(b) Relative angle θ_{u-v}.

Figure 28: Evolution of the angular velocity ω_C and of the angle θ_{u-v} for different number of sub-parts of the cylinder N.

Finally, the same analysis for the linear velocities are given in Fig.(29). Once again, the curves overlap.

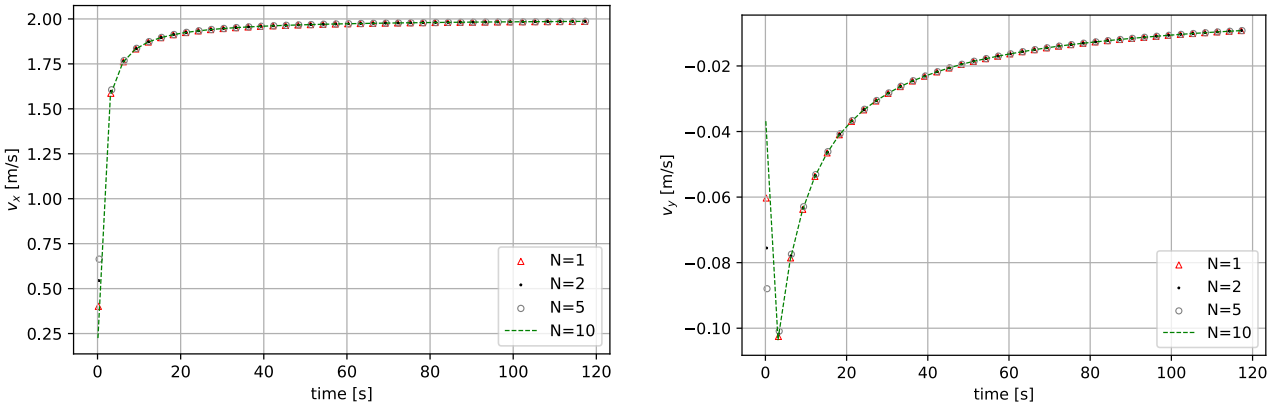

(a) x-component of the linear velocity.

(b) y-component of the linear velocity.

Figure 29: Evolution of the linear velocities $\mathbf{v}$ for different number of sub-parts of the cylinder N.

4 Collisions

Within the dynamic modeling of floating objects the incorporation of a collision model is an imperative necessity. The underlying objective is to accurately anticipate clogging phenomena, a major issue in water resource management.

In this section, the focus is on collision mechanics. These encompass the fundamental interactions between floating objects and their immediate environment, whether river walls or obstacles. The impact of these collisions on debris movement is of crucial importance in refining predictions. Through a rigorous analysis of these collisions, the aim is to enrich the global dynamics model.

In more detail, the section is structured as follows. First, particular attention is paid to the model description, highlighting obstacle modeling and the identification of various collision types. The focus then turns to the detection model, followed by an examination of the adjustments required in the event of collisions. The numerical implementation of the model is then detailed, paving the way for the first numerical simulations that incorporate a variety of obstacle and collision types. Emphasis is placed on the model's ability to predict and rectify collisions, while examining its limitations and opportunities for improvement.

4.1 Description

The objective is to build a general model capable of reflecting as much of the physics of collisions as possible. This requires a model for the obstacles themselves and for the collisions and their corrections. Additionally, the model must be capable of handling multiple collisions simultaneously to address cases of blockage. Finally, it is crucial for the model to be sufficiently versatile to align with real-world simulations and input datasets.

In the following explanations, an original model of detection is presented and the application of the "Newton's law of restitution for instantaneous collisions with no friction" (Hecker, 1997) is used.

4.1.1 Obstacles model and type of collisions

In order to determine 'collision types', it is first necessary to define a model for the obstacles. First, there are collisions with the flume walls. These are defined as *main walls*, *up* (resp. *down*) for the top (resp. bottom) wall[4]. When it comes to modeling other obstacles, such as chicanes, bridge piers or other obstacles of any shape in the channel, it has been decided to model them using rectangles. The walls that make up objects is defined as *sub-walls*. In obvious notation, there exist sub-walls *up, down, left* and *right*. Fig.(30) illustrates the various definitions.

[4] Please note that bottom refers to the lowest part of the obstacle in the global reference frame (x, y). This is not the floor of the channel, since the model only studies the horizontal.

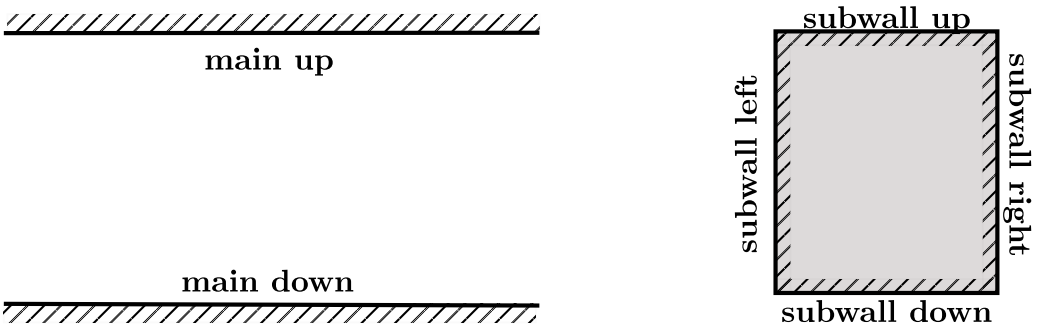

Figure 30: Collision models with the channel (main wall), on the left, or with rectangular obstacles (sub-wall), on the right.

In addition to the advantage of a straightforward implementation of obstacle geometry, this allows the program to take as input a mapping of channels defined as such. For example, the software WOLF (ULiège, HECE) is capable of generating such mappings. The ultimate aim is to discretize any shape into a set of cells, in order to apply the resulting model to more complex shapes, as represented for a circle in Fig.(31).

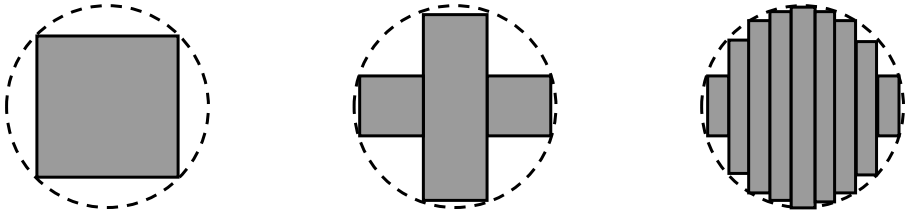

Figure 31: Discretization of a circular obstacle with the basic rectangles of the model, for a number of subdivisions equal (from left to right) to 1, 3 and 9.

The main advantage of this simple rectangle model is the ability to classify collisions into just 3 main types. The first type is a so-called *horizontal* collision, for collisions between the object and the *top* and *bottom* walls. The second is *vertical* collisions between the object and the *left* and *right* walls. The last case, never mentioned in the literature, is *corner*. This is a mixed case, between a vertical and horizontal collision when the object collides at the corner of the rectangle. These three types are all equally important and, for collisions with obstacles, are rarely of just one type.

4.1.2 Collision detection

Collision detection is trivially based on the position of the cylinder. It is very important to specifically define each part of the cylinder, the obstacle and the type of collision to successfully identify collisions and their hierarchy.

A **first** assumption is required. The domain in which the cylinder moves is assumed to be positive ($x > 0, y > 0$). A **second** assumption is to approximate the cylinder as a straight line with the same physical properties. This line is aligned with its major axis (the line that connects the two centers of the circular bases and is perpendicular to them). As a **third** assumption, the cylinder is considered rigid, undeformable and therefore unbreakable. Thus, its geometric properties (e.g. shape and size) and intrinsic physical properties (e.g. mass and coefficients) are preserved, whatever the collision it undergoes. The **fourth** assumption consists in considering the obstacle to be larger than the cylinder. By breaking down collisions into three types. Thus, it can be considered that horizontal and vertical collisions are caused by the edges of the cylinder only. The edge likely to collide have components denominated $(x_{\text{hit}}, y_{\text{hit}})$ and the other $(x_{\text{other}}, y_{\text{other}})$. On the other

hand, the determination of hit and other edges for collisions no longer makes sense, since this type of collision occur somewhere on the cylinder and not necessarily on an edge.

The key idea is to determine which extremity is the *hit* one and which is the *other* one. Instead of calculating distance, as suggested in the literature, it was decided to take advantage of knowledge of the configuration, and more specifically of the position of obstacles. Although it requires a comprehensive study of all possible cases and sub-cases, this step eventually enables a fairly effective detection model.

Horizontal collisions

A horizontal collision can appear on a vertical wall. The criterion defined in this model is as follows, and is presented in detail below.

Criterion for horizontal collisions

By using the subscript *sub-wall bottom* (resp.*sub-wall top)* to denote the coordinate of the bottom (resp. top) edge of the obstacle, the criteria write as follows.

Let the subscript *hit* denote the coordinates of the rightmost edge of the cylinder and *other* the one of the other edge. If $x_{\text{hit}} > x_{\text{vertical wall left}}$ and $y_{\text{hit}} \in [y_{\text{sub-wall bottom}}, y_{\text{sub-wall top}}]$, then there exists a horizontal collision with the vertical **left** sub-wall of the obstacle.

Let the subscript *hit* denote the coordinates of the leftmost edge of the cylinder and *other* the one of the other edge. If $x_{\text{hit}} < x_{\text{vertical wall left}}$ and $y_{\text{hit}} \in [y_{\text{sub-wall bottom}}, y_{\text{sub-wall top}}]$, then there exists a horizontal collision with the vertical **right** sub-wall of the obstacle.

For this kind of wall, two sub-cases are possible: right and left. For a left sub-wall, the right-hand edge is decisive, and vice versa. This situation is represented in Fig.(32).

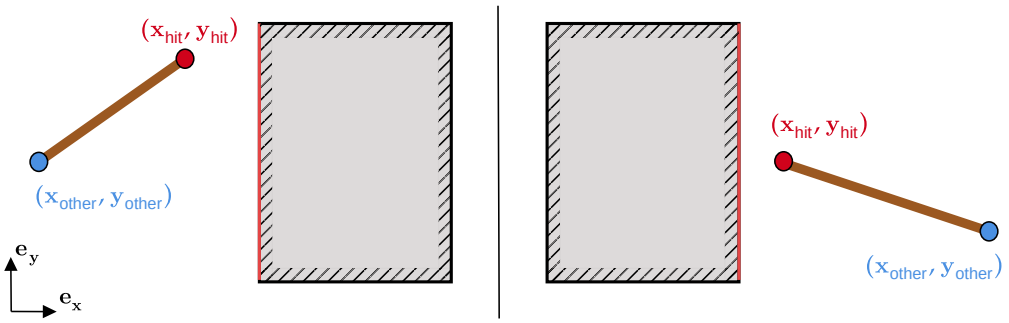

Figure 32: Determination of the *hit* and *other* edges for horizontal collision, with vertical left (depicted on the left) and right (depicted on the right) sub-walls.

Once the positions of the cylinder edges have been identified as hit and other, the next step is to check for collisions. For the hit edge, the criterion obviously checks whether its horizontal position (x_{hit}) goes over the wall or not, and whether the vertical position (y_{hit}) is in the interval where the wall exists. The subscript 'sub-wall' is used because the main wall is defined as horizontal, and any other wall refers to 'sub-walls'.

Finally, the Fig.(33) represents the criterion. The figures on the left (Fig.(33)a, 33)b)) refer to the criterion for collision with a left wall and the figures on the right (Fig.(33)c, 33)d)) refer to

the criterion for a collision with a right wall. It can be observed that in Figs.(33a) and (33c), the criterion is not filled while Figs.(33c) and (33d) show the contrary.

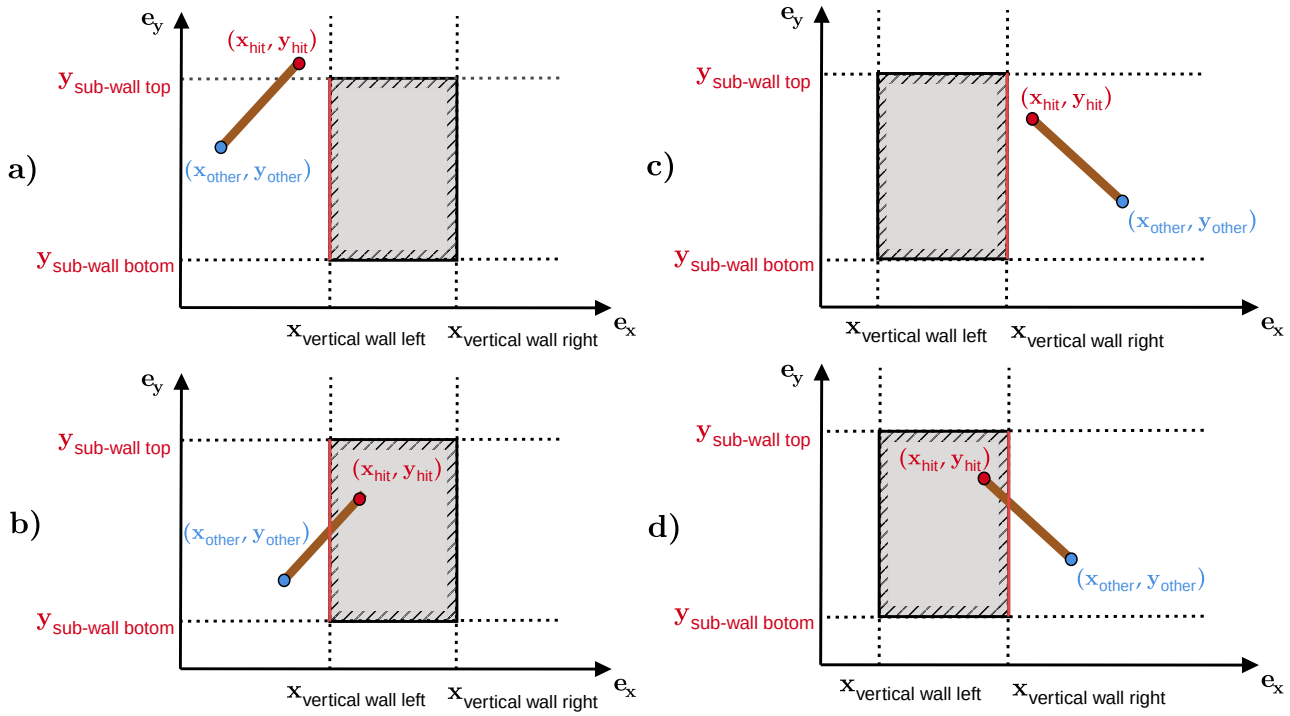

Figure 33: Determination of the collision condition for horizontal collision with vertical walls.

Vertical collisions

A vertical collision can appear on a horizontal wall. The criterion defined in this model is as follows, and is presented in detail below.

Criterion for vertical collisions

By denoting the left (resp. right) coordinates of the obstacle by the subscript *left* (resp. *right*), the criteria write as follows.

Let the subscript *hit* denote the coordinates of the bottommostst edge of the cylinder and *other* the one of the other edge. If $y_{\text{hit}} < y_{\text{vertical wall top}}$ and $x_{\text{hit}} \in [x_{\text{left}}, x_{\text{right}}]$, then there exists a vertical collision with the horizontal **top** sub-wall of the obstacle.

Let the subscript *hit* denote the coordinates of the top-most edge of the cylinder and *other* the one of the other edge. If $y_{\text{hit}} > y_{\text{vertical wall bottom}}$ and $x_{\text{hit}} \in [x_{\text{left}}, x_{\text{right}}]$, then there exists a vertical collision with the horizontal **bottom** sub-wall of the obstacle.

For this kind of wall, two sub-cases are possible: top and down. For a wall up, the lowest edge is decisive, and vice versa. This situation is represented in Fig.(34).

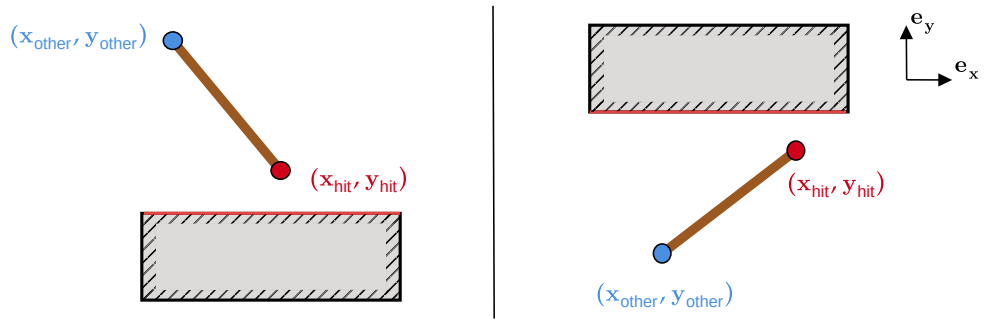

Figure 34: Determination of the *hit* and *other* edges for vertical collision, with horizontal top (depicted on the left) and bottom (depicted on the right) sub-walls.

The next step is to check for collisions. For the hit edge, the criterion obviously checks whether its vertical position (y_{hit}) goes over the wall or not, and whether the horizontal position (x_{hit}) is in the interval where the wall exists. The following red box summarizes the criterion's for vertical collisions. The Fig.(35) represents this criterion. In particular, figures on the left (Figs.(35a,35b)) represent the criterion for a collision with the top sub-wall, while figures on the right (Figs.(35c,35d)) represent it for a sub-wall. The criterion is fullfilled for Figs.(35b,35d).

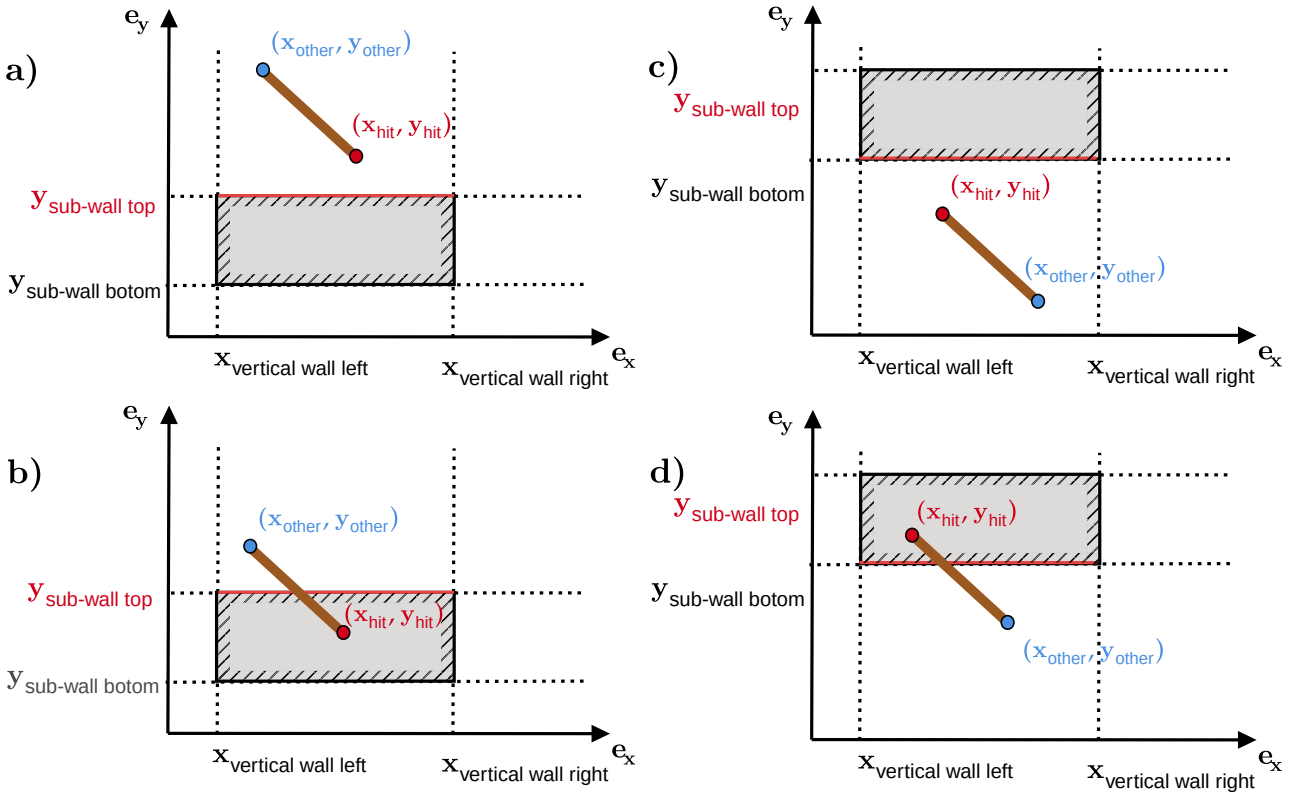

Figure 35: Determination of the collision condition for vertical collision with horizontal walls.

Corner collisions

A corner collision occurs when part of the object passes both a vertical and horizontal subwall, i.e. one of the obstacle's corners. The criterion defined in this model is as follows, and is presented in detail below.

Criterion for corner collision

By denoting $y_c(x_c)$ as the Cartesian function of the major axis of the cylinder and using the subscript *left* (resp. *right*) for the left (resp. right) vertical wall of the obstacle, the criteria write as follows.

Let the subscript *hit* denote the coordinates of the rightmost edge of the cylinder, *other* the one of the other edge and (x_P, y_P) be the coordinates of the corner up left. If $x_{\text{hit}} \in [x_{\text{left}}, x_{\text{right}}]$ and $x_{\text{other}} < x_{\text{left}}$ and if $y_P > y_c(x_c)$, then there exists a collision with the **corner up left**.

Let the subscript *hit* denote the coordinates of the rightmost edge of the cylinder, *other* the one of the other edge and (x_P, y_P) be the coordinates of the corner down left. If $x_{\text{hit}} \in [x_{\text{left}}, x_{\text{right}}]$ and $x_{\text{other}} < x_{\text{left}}$ and if $y_P < y_c(x_c)$, then there exists a collision with the **corner down left**.

Let the subscript *hit* denote the coordinates of the leftmost edge of the cylinder, *other* the one of the other edge and (x_P, y_P) be the coordinates of the corner up right. If $x_{\text{hit}} \in [x_{\text{left}}, x_{\text{right}}]$ and $x_{\text{other}} > x_{\text{right}}$ and if $y_P > y_c(x_c)$, then there exists a collision with the **corner up right**.

Let the subscript *hit* denote the coordinates of the leftmost edge of the cylinder, *other* the one of the other edge and (x_P, y_P) be the coordinates of the corner down right. If $x_{\text{hit}} \in [x_{\text{left}}, x_{\text{right}}]$ and $x_{\text{other}} > x_{\text{right}}$ and if $y_P < y_c(x_c)$, then there exists a collision with the **corner down right**.

As already mentioned, this collision does not always take place on the *hit* edge, but somewhere along the cylinder. However, the names *hit* and *other* are kept to distinguish the two ends of the cylinder.

There are four sub-cases here, since a rectangle has four corners: up left, up right, down left and down right. Each of these has a different collision criterion. For the up and down corners on the left, the edge hit is defined as the rightmost edge and vice versa. This consideration is represented in Fig.(36). The up left corner is depicted on the top left, the up right corner on the top right, the down left corner on the bottom left and the down right corner on the bottom right.

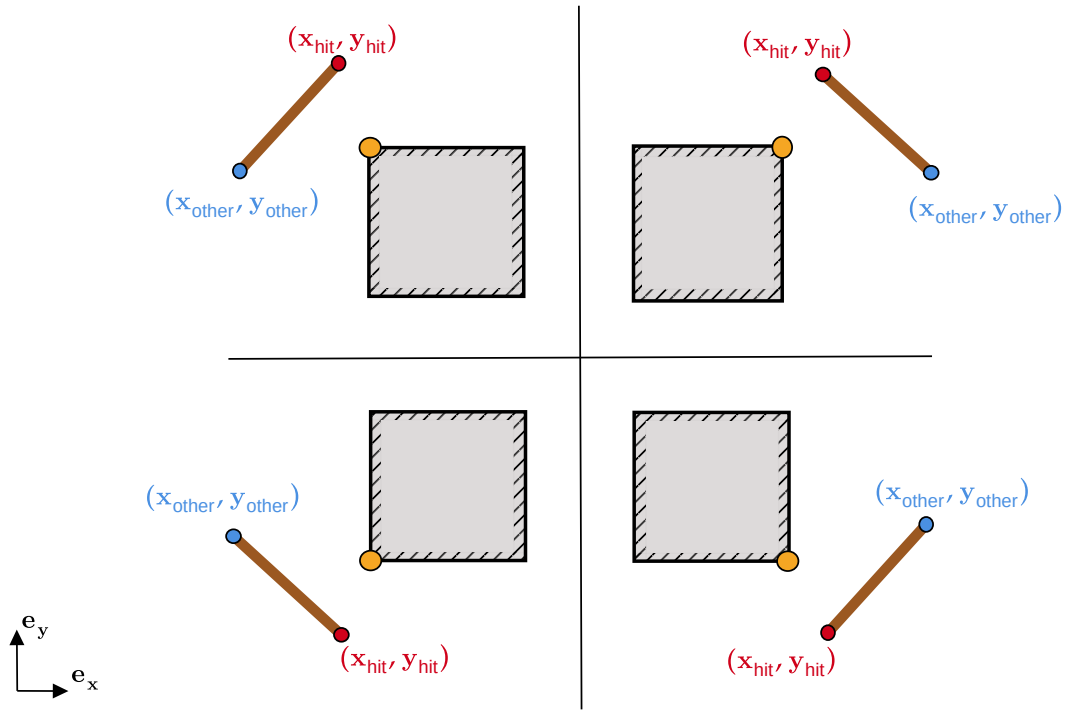

Figure 36: Different types of corner collision, with the definition of *hit* and *other* edges of the cylinder in each cases.

A **first condition** is that $x_{\text{hit}} \in [x_{\text{left}}, x_{\text{right}}]$). In other words, the cylinder must be on either side of the corner. The following reasoning applies to the corner up left case, and the results for the other corners are given directly. The corner is assumed to be at point P with known (x_P, y_P) coordinates. In view of the third assumption made in the preamble to this sub-section, the cylinder is considered to be a straight line. Since the coordinates of its extremities are known, it is possible to obtain its Cartesian equation via the basic equations Eq.(66) with m the slope, p the y-intercept and x_c and y_c the coordinate of the cylinder :

$$\begin{cases} y_c(x_c) & = mx_c + p, \\ m & = \dfrac{y_{\text{hit}} - y_{\text{other}}}{x_{\text{hit}} - x_{\text{other}}}, \\ p & = y_{\text{hit}} - mx_{\text{hit}}. \end{cases} \tag{66}$$

Then, the **second condition** consists in evaluating the function at the x_P point and check whether the cylinder protrudes from the corner, i.e. whether $y_P > y_c(x_c)$. The Fig.(37) illustrates the criterion. In both depicted situations, the condition on x is met ($x_{\text{hit}} \in [x_{\text{left}}, x_{\text{right}}]$ and $x_{\text{other}} < x_{\text{left}}$). On the left, $y_P < y_c(x_c)$ implies that there is no collision. On the right, $y_P > y_c(x_c)$ and a corner up left collision is detected.

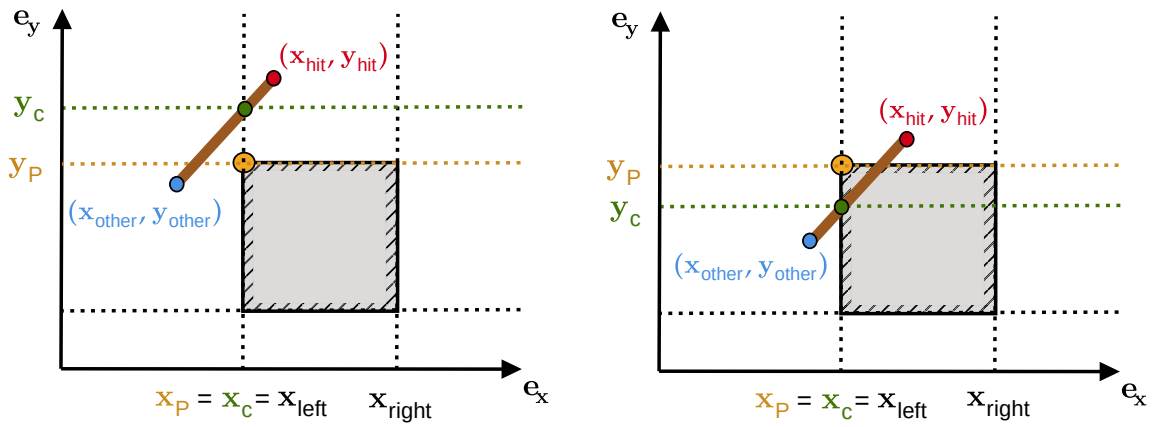

Figure 37: Determination of the collision condition for corner up left collision.

The reasoning can be replicated for the other corners, giving the corner collision criterion stated at the beginning.

4.1.3 Correction

For the correction part, whose aim is to calculate the impact of the collision on the object's dynamics, the results from the literature review in Eq.(56) are used. More specifically, the "Newton's Law of Restitution for Instantaneous Collisions with No Friction", detailed by Hecker (1997), is employed. That is why a frictionless assumption is applied. The strength of this correction model is that it is general, so it can be applied to any type of collision.

The application of the Eq.(56) is straightforward if the normal at the point of impact is known. Applied to this model, this gives Fig.(38).

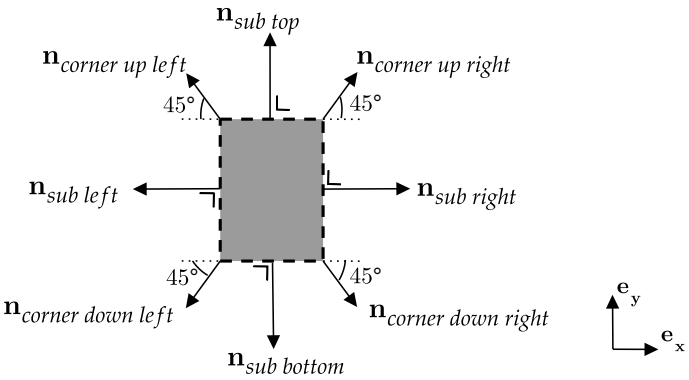

Figure 38: Definition of obstacle normals according to Hecker (1997) applied to selected obstacles.

The components of the presented normal vectors are reported in Tab.(13), note that the normal vector for the main walls top and down are the same as those of the sub-wall top and bottom.

normal	components (x,y)
$\mathbf{n}_{\text{sub top}}$	(0,1)
$\mathbf{n}_{\text{sub bottom}}$	(0,-1)
$\mathbf{n}_{\text{sub right}}$	(1,0)
$\mathbf{n}_{\text{sub left}}$	(-1,0)
$\mathbf{n}_{\text{corner up left}}$	$(-\sqrt{2}/2, \sqrt{2}/2)$
$\mathbf{n}_{\text{corner up right}}$	$(\sqrt{2}/2, \sqrt{2}/2)$
$\mathbf{n}_{\text{corner down left}}$	$(-\sqrt{2}/2, -\sqrt{2}/2)$
$\mathbf{n}_{\text{corner down right}}$	$(\sqrt{2}/2, -\sqrt{2}/2)$

Table 13: Components of the different normal vectors of the obstacles.

4.2 Recommended numerical approach

This subsection present the implementation nuances. Into more details, appendix A describes some very specific parts of the code.

Although each collision type is defined independently, special attention must be given to their hierarchy, specifically the order in which they are considered. Indeed, the correction of one type of collision should not replace another. A good practice revealed by this work is to treat first horizontal collisions (with a vertical wall), Achieving a precise geometric correction after the dynamic correction is essential to completely resolve the collision within a single case and to avoid the risk of unfortunate numerical calculation errors leading to additional collision detection for the same time step.

In addition, it is crucial to implement a smooth identification of *hit* and *other* edges to facilitate multiple corrections in scenarios where multiple edges collide with one or more obstacles. Furthermore, this approach should account for cases where resolving one obstacle collision might trigger the need for subsequent corrections in other obstacles.

Furthermore, collisions affect the entire dynamics of the moving object, through its position, linear and angular velocity and orientation. It is therefore crucial not to overlook a collision. That explains why it is essential to keep in mind that an appropriate timestep must be chosen to prevent object penetrations and to avoid situations where an object pass through an obstacle.

Finally, the practical way the obstacles are implemented is explained in the appendix A.4. However, the Fig.(39) shows simple obstacles creation as baffles or squared bridge piers and more complex discretized obstacles as a circle.

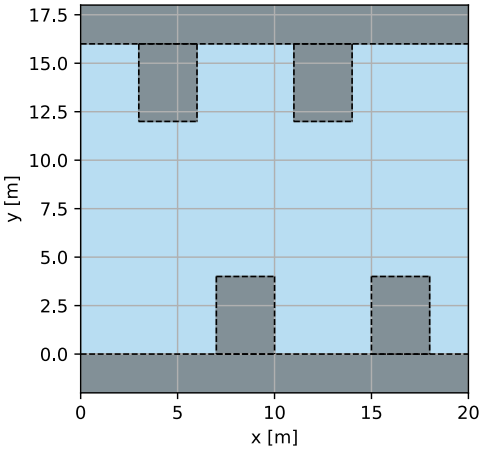

a) Baffles configuration.

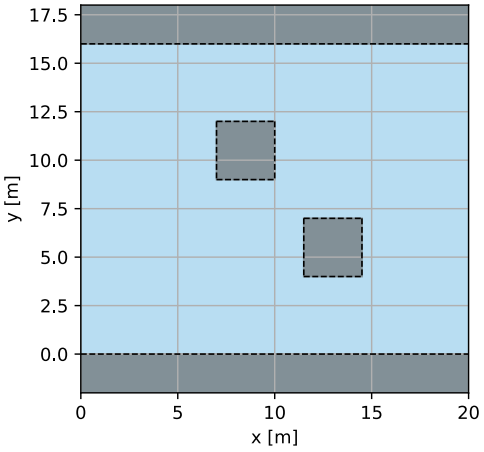

b) Piers configuration.

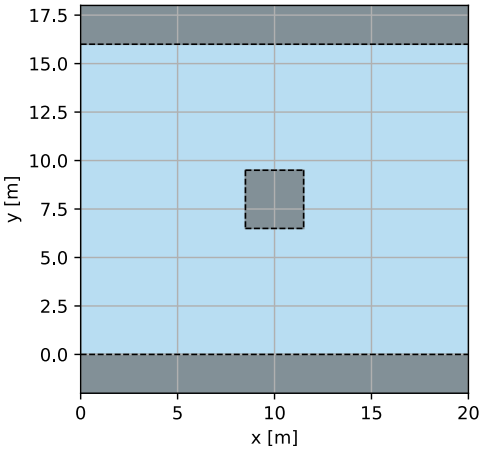

c) Discretized circle $N_r = 1$

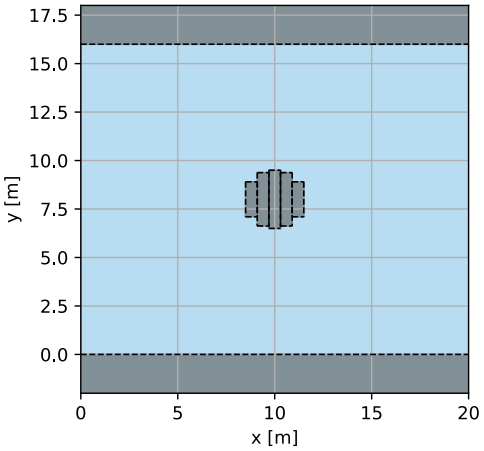

d) Discretized circle $N_r = 5$

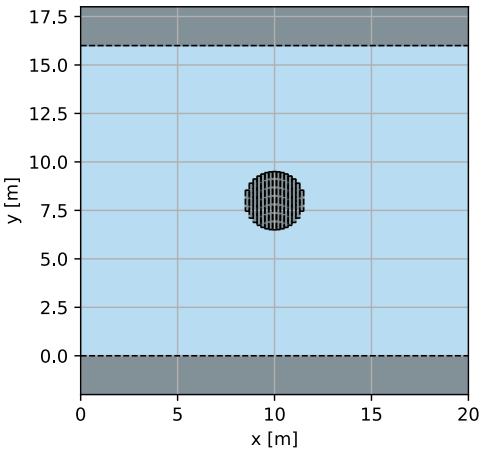

e) Discretized circle $N_r = 15$

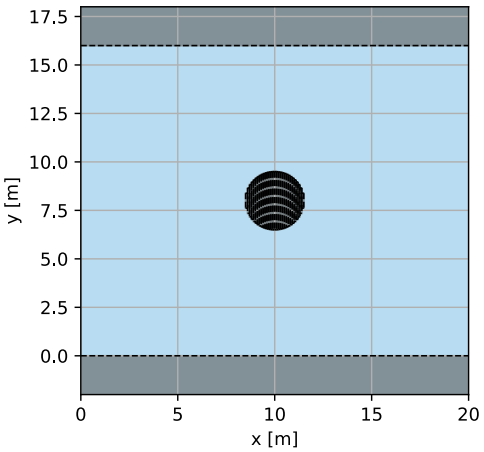

f) Discretized circle $N_r = 30$

Figure 39: Examples of different obstacles creation through the code.

4.3 Simulations

Each type of collision presented above is forced into a numerical simulation and the results are presented here. In particular for sub-walls collisions, the results are presented in detail for the collisions on the left and more briefly for those on the right, since they represent the same physics in the local frame, even if in the global frame the type of collision is different (e.g. horizontal collision with a *left* sub-wall or horizontal collision with a *right* sub-wall). The change has more to do with the practical side of how the code should detect the type of collision.

4.3.1 Vertical collisions

Main wall vertical collisions

First, collisions with *main walls* are presented. In particular, the study of a vertical collision with the *top main wall* is presented, and the equivalent results for the *bottom main wall* is given in the appendices. The cylinder type is based on the physical and geometric characteristics used previously, reported in Tab.(7). The simulation is run with the parameters of Tab.(14). In particular, uniform and stationary flow velocities with a positive vertical component was implemented to force the desired collision. About the configuration, no obstacles are implemented and only the two horizontal walls of the channel are set to $y = 0$ for the bottom wall and y=6 for the top wall.

flow [m/s]	$\mathbf{v_0}$ [m/s]	ω_0 [°/s]	θ_{u-v} [°]	(x_0, y_0) [m]	ϵ [−]	N [−]	h [s]	t_{phys} [s]
uniform stationnary $\mathbf{u} = (\mathbf{2}, \mathbf{1})$	(0,0)	0	60	(3,2)	0.1	1	0.01	15

Table 14: Parameters used for the simulation of vertical collisions with a top main wall.

For the following description, the model implemented without collisions is compared to the one with collisions. A direct way to visualize the impact of the model is to observe the cylinder's trajectory. Fig.(40) shows a simulation without collision model Fig.(40a) and with the model Fig.(40a). It seems the code is able to detect and physically correct the collisions (first of them at 10.5[m]). Vertical collisions with a top main wall appears to have been detected and corrected. The red dotted line is the trajectory of the center of mass, while the cylinder is represented by the brown straight segments. In the collision type classification reported by Ruiz-Villanueva et al. (2014), this is a sliding collision (cf. 2.4.3). Although the specific geometrical corrections of the latter model have not been followed, it is interesting to note that Hecker (1997)'s model is sufficient in itself.

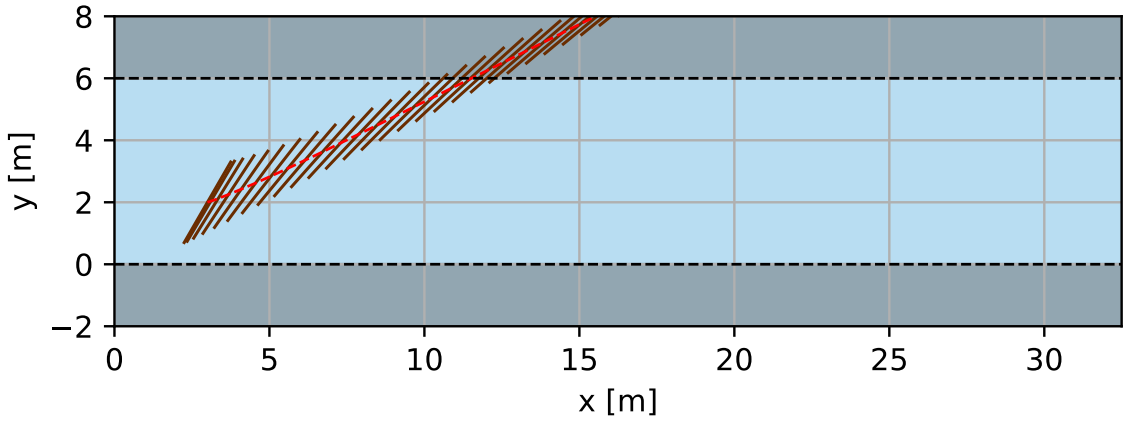

(a) Simulation without collisions.

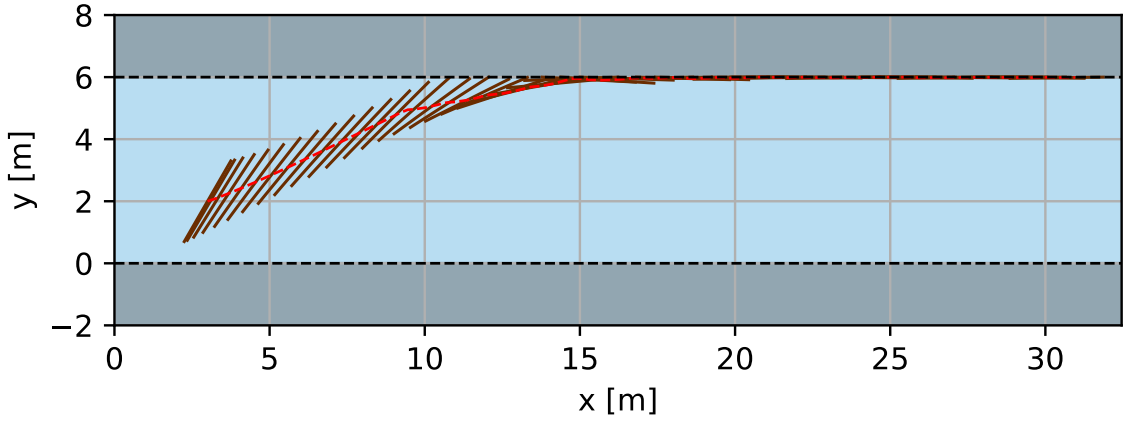

(b) Simulation with collisions.

Figure 40: Comparison of trajectories of floating cylinder with and without collision model.

It is necessary to ensure that the correction is not only geometric, but also based on the object's dynamics. To this end, the graphs of linear velocity, angular velocity and inclination of the cylinder with respect to the horizontal are shown below.

First of all, about the linear velocity in Fig.(41), it can be observed that the graph without any corrections (top graph) shows the convergence expected and presented in the previous section. On the other hand, the graph with the correction clearly shows discontinuities from 4.1[s], time that corresponds to the first collision. This is due to the introduction of the J impulse into the model, whose purpose is to instantaneously modify dynamic quantities (velocities). Overall, the velocity of the hypothetical flow being $\mathbf{u} = (2, 1)$ forces the cylinder to crash against the wall and move only towards positive x. In particular, an initial collision is observed that decreases velocity along x and y. Into more details, the linear velocity along x of the cylinder tends towards that of the flow, despite some corrections. The vertical component of the velocity cancels out with each collision, thus instantaneously halting the cylinder's vertical progression. The intensity with which velocities are modified depends on the restitution coefficient, set at 0.1 for these simulations. This results in collisions with a significant loss of kinetic energy on each impact. Since the impulse is calculated on the basis of linear velocities, it is understandable that the corrections gradually decrease. The fact that the cylinder progressively aligns with the wall also contributes to this reduction, since the collision angle appears in the impulse formula. Physically, this implies that the collision is less and less "violent" as the cylinder aligns with the wall. The impact of the value of the restitution coefficient is studied in detail at the end of this section.

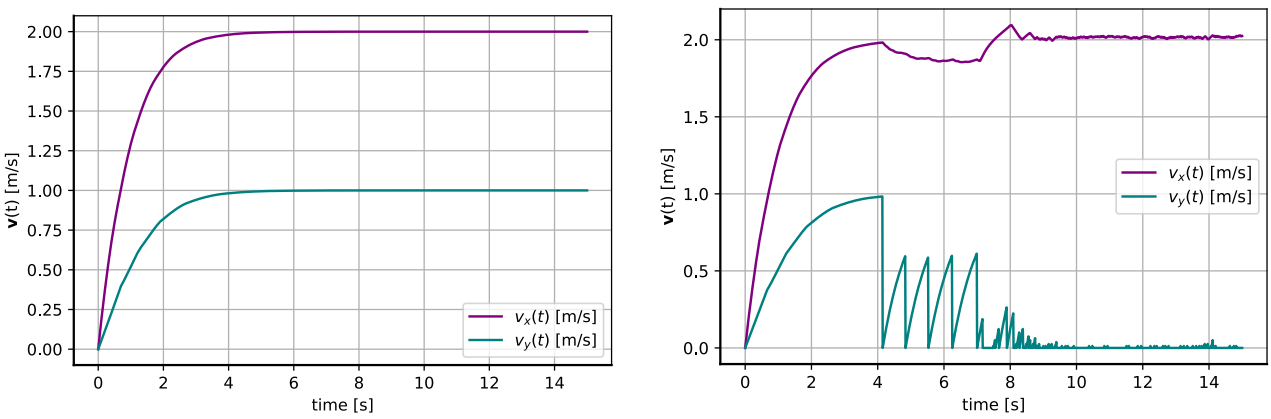

Figure 41: Linear velocity of the cylinder as a function of time, without (resp. with) collision model on the top (resp. bottom) figure, for vertical collisions with a top main wall.

To complete the study of the behavior after the first collision, the angular velocity must be studied (Fig.(42)). The first collision occurs at 4.1[s] before several others. This implies a change of orientation, giving rise to further collisions in the sequence. In addition, angular velocity correction allows to understand the change in cylinder orientation and how this dynamic correction affects its geometric correction.

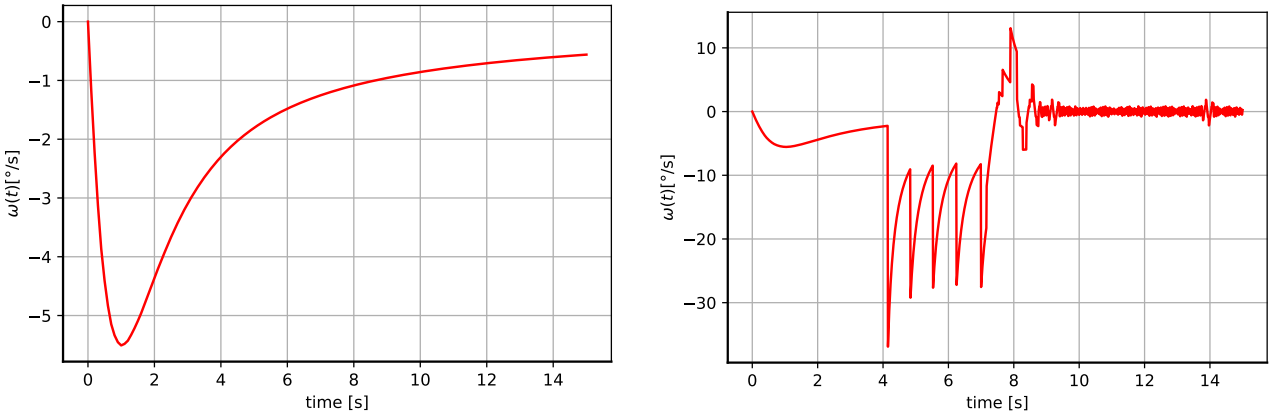

Figure 42: Angular velocity of the cylinder as a function of time, without (resp. with) collision model on the top (resp. bottom) figure, for vertical collisions with a top main wall.

To quantify the fact that the cylinder has a correction on its angle of inclination, the graphs in Fig.(43) are presented. The first collision appears at 4.1[s]. After a while, the cylinder is aligned with the horizontal wall. Indeed, the angle initially converging to an angle of 180[°] with the flow (corresponding for this flow to an angle of 26.46[°] with respect to x) tends towards 0[°] with the collision correction, corresponding to the alignment of the cylinder with the wall observed at the beginning of the sub-section. As the angle of inclination of the cylinder is the derivative of the angular velocity, the behavior of the angle is directly understandable in view of the preceding explanations.

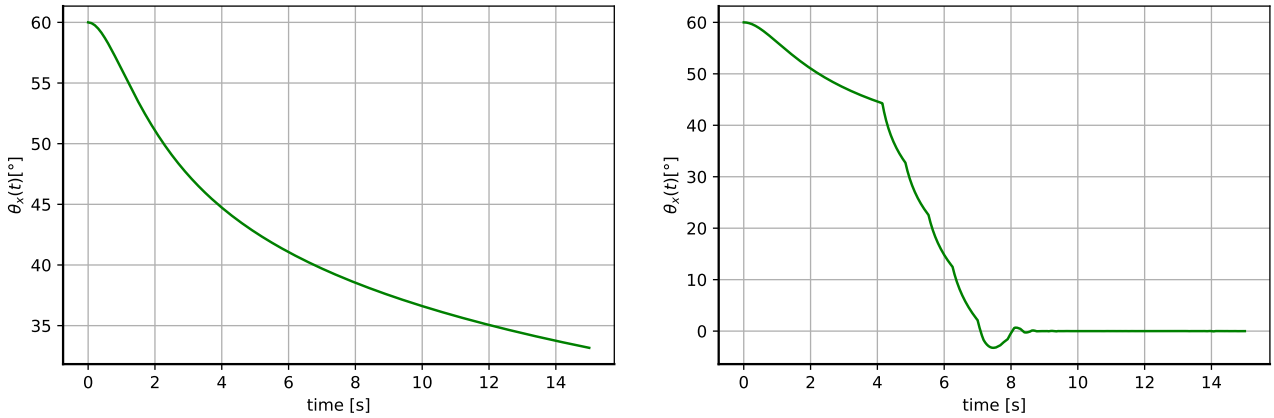

Figure 43: Angle of the cylinder inclination to horizontal as a function of time, without (resp. with) collision model on the top (resp. bottom) figure, for vertical collisions with a top main wall.

Sub wall vertical collisions

To show the results of code simulations for collisions with the horizontal walls of the obstacle, the *top sub-wall* case is presented (the other case, *bottom sub-wall)* is in the appendix). The analysis of collision dynamics is the same as above. The detailed study is no longer presented. However, the correction graphs is shown to check that the corrections made are only applied at impact. To do this, the channel is widened (the top wall is now at y=10[m]), and a rectangular obstacle (4 $\times$2.5[m]) is placed in the channel (corner up left at (4,7) [m]). The initial position and orientation of the cylinder is changed and imposed as indicated in Fig.(15).

flow [m/s]	$\mathbf{v_0}$ [m/s]	ω_0 [°/s]	θ_{u-v} [°]	(x_0, y_0) [m]	ϵ [−]	N [−]	h [s]	t_{phys} [s]
uniform stationnary $\mathbf{u} = (\mathbf{2}, \mathbf{1})$	(0,0)	0	100	(3,2)	0.1	1	0.01	15

Table 15: Parameters used for the simulation of vertical collisions with a bottom sub-wall.

The collision model produces the trajectory shown in Fig.(44). It can be seen that corrections are made, allowing the cylinder not to cross the obstacle and to return to its path once it has passed the obstacle. In addition, the correction with the top main wall that follows is still ensured.

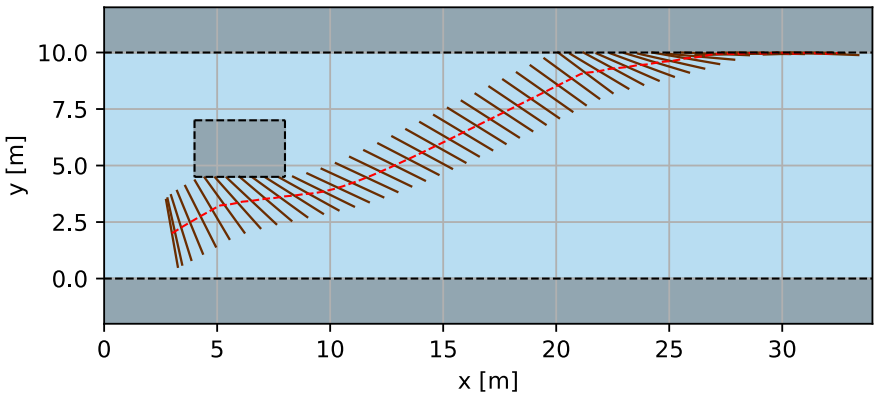

Figure 44: Trajectory of floating cylinder in horizontal plane (x, y). The red dotted line is the trajectory of the center of mass, while the cylinder is represented by the brown straight segments.

The interpretation of the graphs in Figs.(45) is similar to the discussion of the main wall and the trajectory. For each of the graphs, collisions with the obstacle are between 1.6 and 3.5[s] and collisions with the main wall after 9.6[s]. Between the two collision intervals, the cylinder reverts to the classic behavior studied for translation and rotation in the previous sections. Thus vertical collisions with a bottom sub wall appears to be detected and corrected.

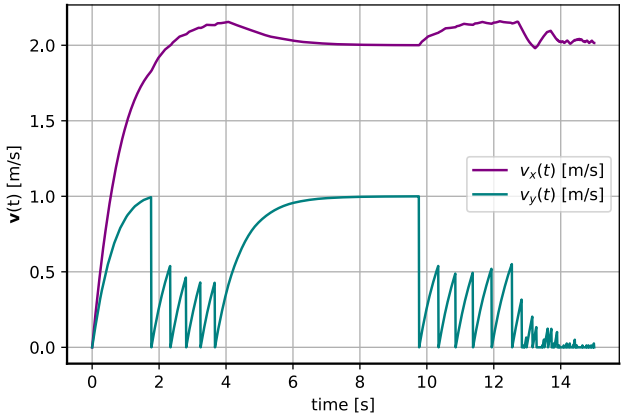

a) Linear velocities.

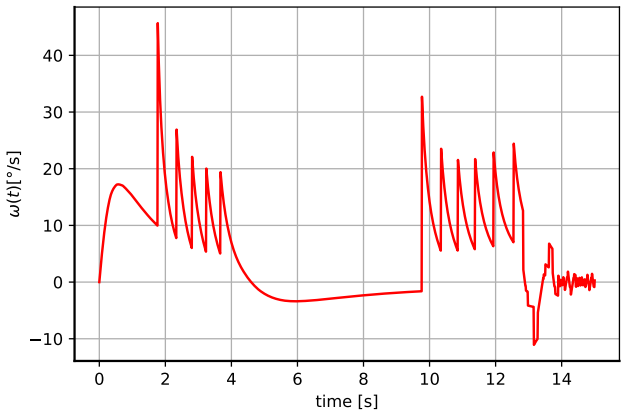

b) Angular velocity.

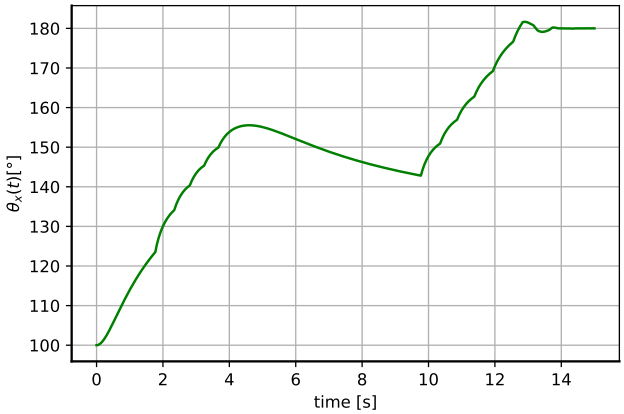

c) Angle of inclination (global frame)

Figure 45: Linear velocities, angular velocity and inclination angle of the cylinder as a function of time.

4.3.2 Horizontal collisions

As explained above, horizontal collisions refer to collisions with sub-walls. Emphasis is placed on the left-hand edge of the obstacle, while the right-hand edge is reserved for the appendix. With the imposed conditions of the simulations, this type of collision is often followed by *corner* collisions. That is why the flow velocity is here fixed to (2,0). Once again, this is a non-real-life situation, used only to check the effectiveness of the correction on a sub-wall collision with a pure left sub-wall. The used parameter are indicated in the Tab.(16). The main walls are placed $y = 0$ and $y = 10$ as before and the obstacle (4×5 [m]) is centered at (11.5, 3.5)[m].

flow [m/s]	$\mathbf{v_0}$ [m/s]	ω_0 [°/s]	θ_{u-v} [°]	(x_0, y_0) [m]	ϵ [−]	N [−]	h [s]	t_{phys} [s]
uniform stationnary $\mathbf{u} = (\mathbf{2}, \mathbf{0})$	(0,0)	0	20	(3,5)	0.1	1	0.01	15

Table 16: Parameters used for the simulation of vertical collisions with a left sub-wall.

Once again, the study begins on the trajectory shown in Fig.(46).

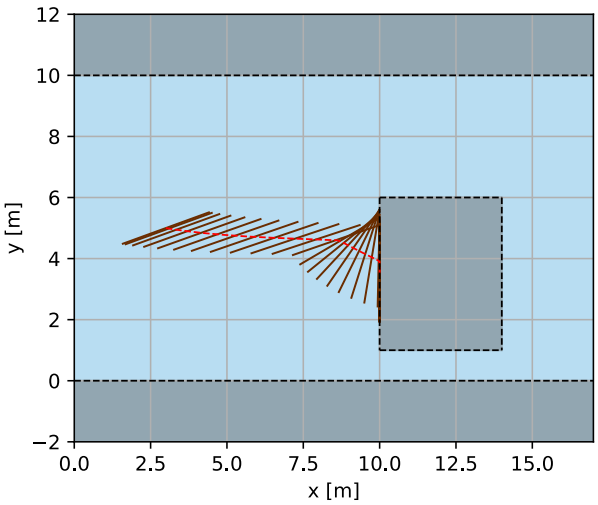

Figure 46: Trajectory of floating cylinder in horizontal plane (x, y) in a horizontal collisions with the left sub-wall. The red dotted line is the trajectory of the center of mass, while the cylinder is represented by the brown straight segments.

The interpretation of the graphs in Figs.(47, 48) is here again the same as before. For each of the graphs, collisions with the obstacle start at 4[s]. It is observed that the cylinder seems to rotate with its point of impact as a fixed point. As a result, its angular velocity varies greatly (positively, implying anti-clockwise rotation). This has an impact on its linear velocity, since hydrodynamic forces are modified by its change of orientation. Then, the linear velocity at x tends towards 0. However, an error of around 0.03[m/s] remains, even though physically the object should be stopped (assuming the flow is correct). This is not due to the restitution coefficient, since the error remains over the long term. One hypothesis would be that this is a numerical error, small enough to be neglected. What is more, it is enough to consider the correction acceptable, since in real-life simulations, the flow has re-circulations enabling the object not to be stopped as in this hypothetical case. Finally, as regards the very rapid oscillation in long-term post-collision behavior, this is explained by a succession of detection and correction. The hypothetical flow does not stop, forcing the object perpetually collide the obstacle and be corrected.

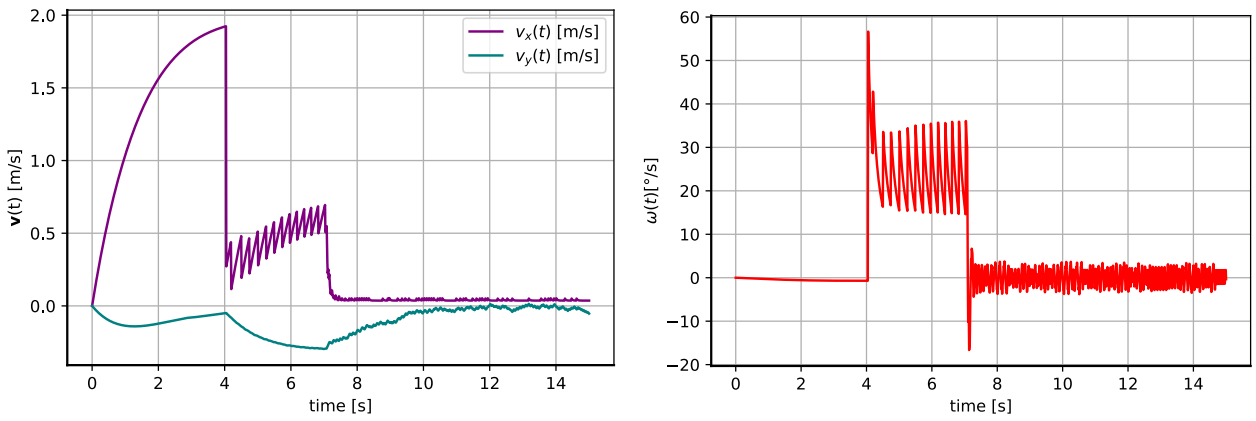

Figure 47: Linear and angular velocities of the cylinder as a function of time for horizontal collisions with the left sub-wall.

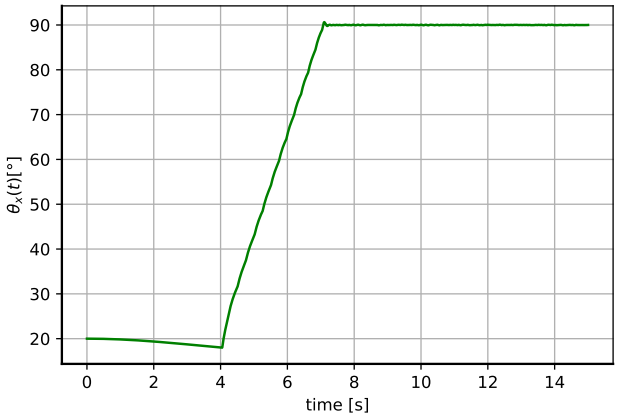

Figure 48: Angle of the cylinder inclination to horizontal as a function of time for horizontal collisions with the left sub-wall.

4.3.3 Corner collisions

Once again, only one of the cases referring to this same family is presented here, and that is the corner up left case. The associated appendix presents the corner down right case (only). As mentioned above, this type of collision is often linked to others. In this case, a simulation featuring a wall-left collision followed by a corner collision is presented. In simulations with real flows, this type of collision is the most common. The parameters used for this simulation are shown in Tab.(17) The geometry used is the same as before (rectangle of 4×2.5 [m^2] centered at (6, 4.25)).

flow [m/s]	$\mathbf{v_0}$ [m/s]	ω_0 [°/s]	θ_{u-v} [°]	(x_0, y_0) [m]	ϵ [−]	N [−]	h [s]	t_{phys} [s]
uniform stationnary $\mathbf{u} = (\mathbf{2}, \mathbf{0})$	(0,0)	0	70	(2,6)	0.1	1	0.01	15

Table 17: Parameters used for the simulation of corner up left collisions.

The trajectory calculated for this situation is shown in Fig(49). By analyzing the center of mass (whose trajectory is dotted in red) it can be seen that it goes around the corner. For the entire cylinder, it is observed that it rotates so that the corner represents a fixed point of rotation.

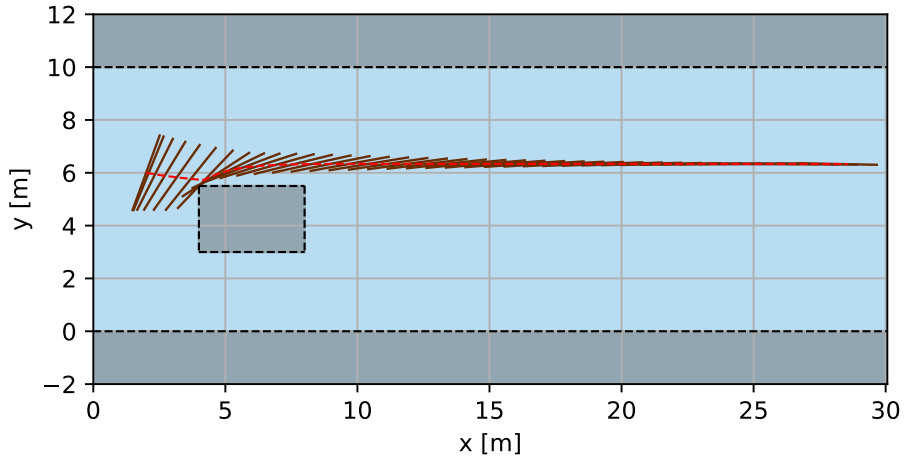

Figure 49: Trajectory of floating cylinder in horizontal plane (x, y) in the case of corner up left collisions. The red dotted line is the trajectory of the center of mass, while the cylinder is represented by the brown straight segments.

The interpretation of the graphs in Figs.(50) is here again the same as before. The collisions with the obstacle start at 2.3[s]. Linear velocities are affected over a shorter time interval. The angular velocity correction here is negative, implying rotation in the clockwise direction, as implied by the collision. Once again, the cylinder returns to a stable equilibrium position after its collisions.

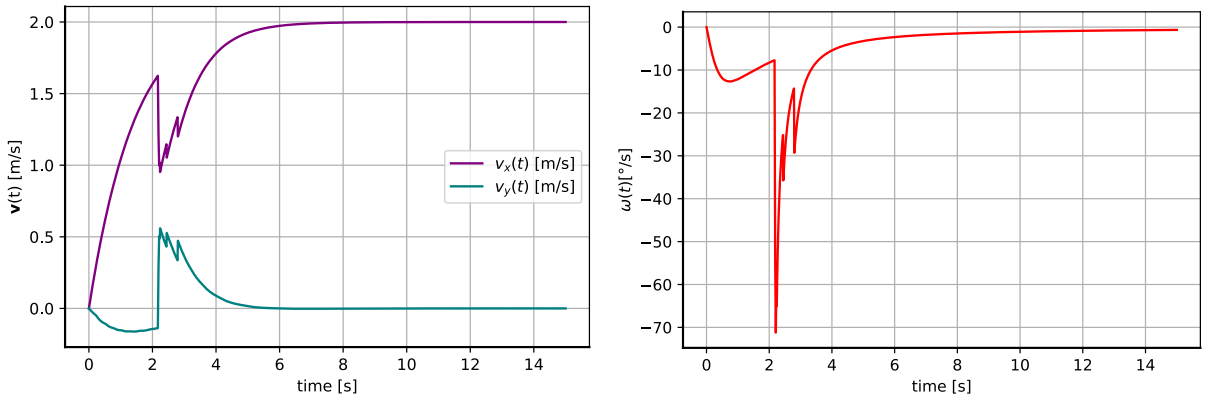

a) linear velocities.

b) angular velocities.

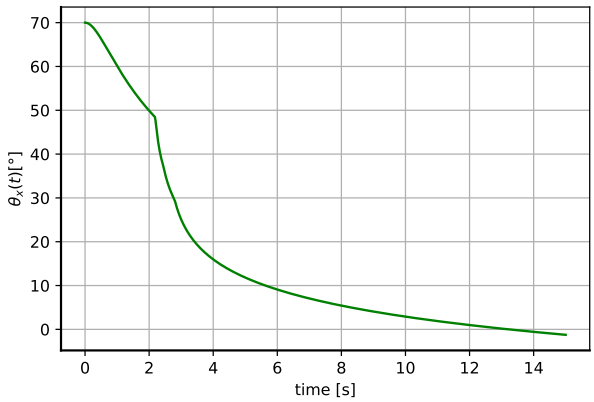

c) inclination angle.

Figure 50: Linear velocities, angular velocity and inclination angle of the cylinder as a function of time for corner up left collisions.

4.3.4 Multiple collisions (clogging prediction)

In addition to testing collision types, it is necessary to check that the code is capable of generating multiple collisions. This concerns collisions where several points on the cylinder collide with an obstacle. This is very important, for example, if the cylinder is blocked by two different obstacles. For this reason, a first simple case is shown. In the following, the focus is on trajectory graphs.

First example

The first example is the simplest case. The idea is to simulate clogging caused by two obstacles. First, a clogging resulting from the same type of collision (horizontal) is simulated. To do this, a purely horizontal flow is simulated ($\mathbf{u} = (\mathbf{2}, \mathbf{0})$), with a cylinder oriented perpendicular to the flow. Its inital position is (x_0, y_0)=(2,5). Two square-shaped obstacles (3 × 3 [m^2]) spaced at medium intervals (2 [m]) are placed in the flume. The simulation shown in Fig.(51) shows that clogging is predicted.

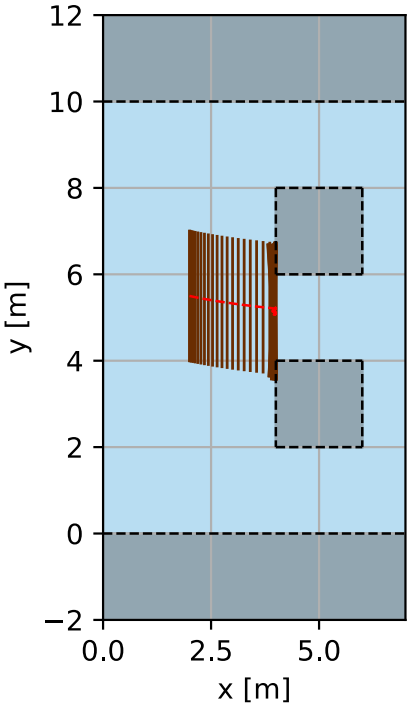

Figure 51: Trajectory of floating cylinder in horizontal plane (x, y), with two square-shaped obstacles (2 × 2 [m^2]) aligned and spaced vertically at medium intervals (2 [m]) in the flume.

Second example

As a second example, two square-shaped obstacles (3 × 3 [m^2]) spaced at medium intervals (1.5 [m]) are placed in the channel, one centered at (7.5,7.5) [m] and the other at (12, 3.5)[m]. Other parameters are reported in Tab.(18).

flow [m/s]	$\mathbf{v_0}$ [m/s]	ω_0 [°/s]	θ_{u-v} [°]	(x_0, y_0) [m]	ϵ [−]	N [−]	h [s]	t_{phys} [s]
uniform stationnary $\mathbf{u} = (\mathbf{2}, \mathbf{0})$	(0,0)	0	135	(6,2.5)	0.1	1	0.01	15

Table 18: Parameters used for the simulation of the second example of multiple collisions.

The cylinder trajectory calculated by the code is shown in Fig.(52). It can be seen that the cylinder remains trapped between the two obstacles for a short time lapse (about 6.5[s]). Two different ends of the cylinder collide with the obstacles during the same time step, and the code is able to take this into account.

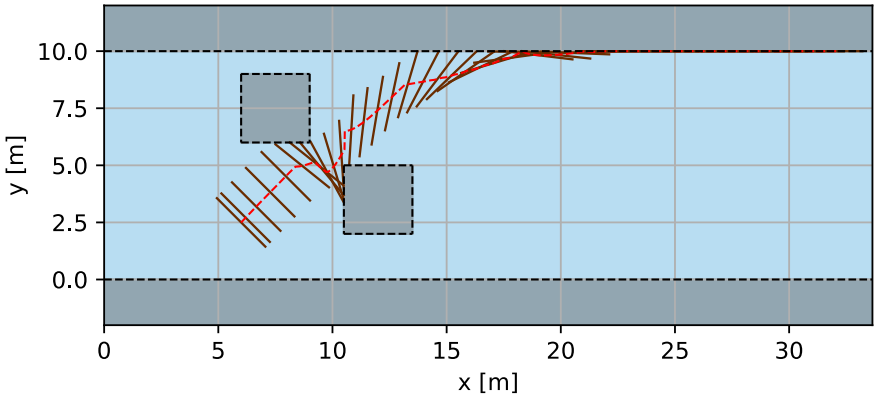

Figure 52: Trajectory of floating cylinder in horizontal plane (x, y), with two square-shaped obstacles (3×3 [m^2]) spaced at medium intervals (1.5 [m]) in the flume.

This effect is an important one to take into account in this master's thesis. Actually, when several floating objects are in this situation, their interaction can lead to a clogging.

It is possible to simulate, under the same conditions, the case where the cylinder strikes each obstacle at the same speed. The result is given in Fig.(53). This is a special case, but it demonstrates the code's ability to handle multiple collisions and predict clogging. For this purpose, a cylinder oriented at 45[°] to the horizontal is simulated. Unlike the previous example, the cylinder is permanently wedged between the two obstacles. This is a hypothetical case, given the flow under consideration (unsteady and uniform despite the obstacles). However, it is unlikely that simulations result in this type of clogging, given the difficulty of implementing it.

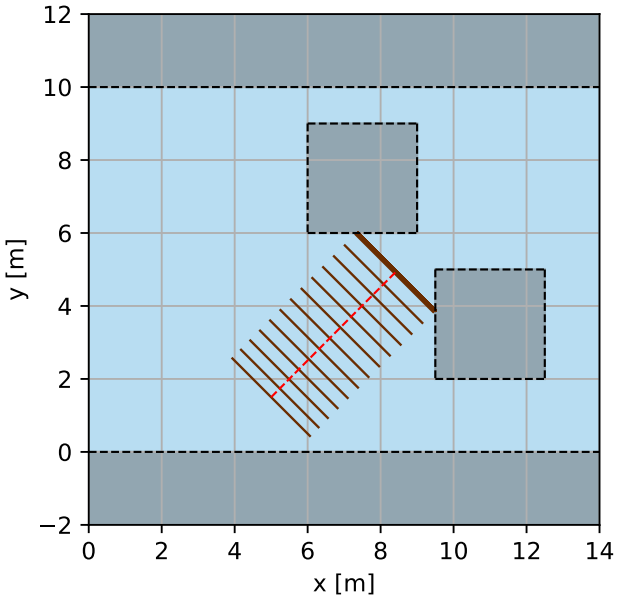

Figure 53: Trajectory of floating cylinder in horizontal plane (x, y), with two square-shaped obstacles.

Third example

The same concept as before is applied to a discretization involving two circular obstacles divided into 7 rectangles (Fig.(54)). In this simulation, achieving the cylinder's complete halt between the two obstacles proves even more challenging. The cylinder's edges consistently slide along either wall. Nevertheless, as previously indicated, the interaction between the cylinder and the two obstacles could potentially lead to clogging when multiple pieces of wood are considered.

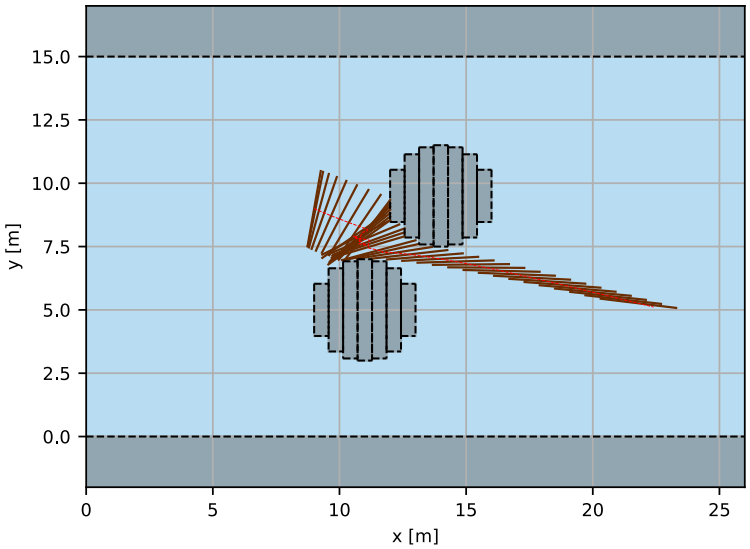

Figure 54: Trajectory of floating cylinder in horizontal plane (x, y), with two discretized circled obstacles.

4.3.5 Limitations and special cases

The purpose of this sub-subsection is to set out the limitations of the collision model, in terms of obstacles, their detection and correction.

Obstacles limits

When multiple obstacles are assembled together, sharing a boundary (e.g., two squares placed edge-to-edge) in a linear fashion (e.g., two squares placed at their corners), the object can sometimes be stuck on this boundary or pass through it if it is perfectly aligned. To address this issue, it is sufficient to introduce a small overlap between the created obstacles.

Time step and obstacle size

A significant constraint of the proposed collision detection model is related to the time step. If the time step is chosen too large, it may result in insufficient collision detection, leading to a situation where the cylinder appears to "cross" the obstacle. This situation is clearly unacceptable in a realistic dynamic model. Consequently, when the obstacle size is very small, accurate collision detection becomes impossible with a reasonable time step. An example of a collision with an object of reasonable size and another of smaller size is shown in the Figs.(55). It is observed for the small obstacle that the cylinder crosses the obstacle after a few first collisions. This is due to the fact that it gains velocity (linear and angular) as previously studied, but that the time step remains too small to correctly apply the detection criteria.

This problem also calls into question the generalization of the model, which is intended to be applicable to a variety of shapes (discretization into rectangles). Indeed, the more complex the shape to be discretized, the greater the number of rectangles required for accurate discretization, and consequently the smaller their size. This is particularly illustrated in Fig.(56). The correct resolution of collisions hinges upon the preservation of adequately sized sub-sections within the circles. This ensures that interactions are accurately managed. The top figure illustrates this concept, demonstrating a circle discretized into 21 segments. Similarly, the bottom figure shows the scenario with 7 segments. These visual representations emphasize the significance of maintaining a suitable granularity in circle discretization to achieve precise collision handling. In this simulation, collision corrections bring the cylinder to the other side of the obstacle, due to detection of the wrong type of collision, leading to a chain to a total mis-correction. With the current model (which has not improved on this problem) there is a balance between the accuracy of the discretization and the accuracy of the collision detection.

To remedy this, the implementation of a variable time step seems to be an unavoidable solution. This would enable the model to work reliably with a variety of obstacle sizes, while guaranteeing accurate collision detection.

However, this limitation is not be problematic for specific simulations of baffles in laboratory channels, which are the main focus of the current collision model. These simulations aim to reproduce the experimental conditions found in the literature, and this limitation has therefore no impact on the results of the Master's Thesis.

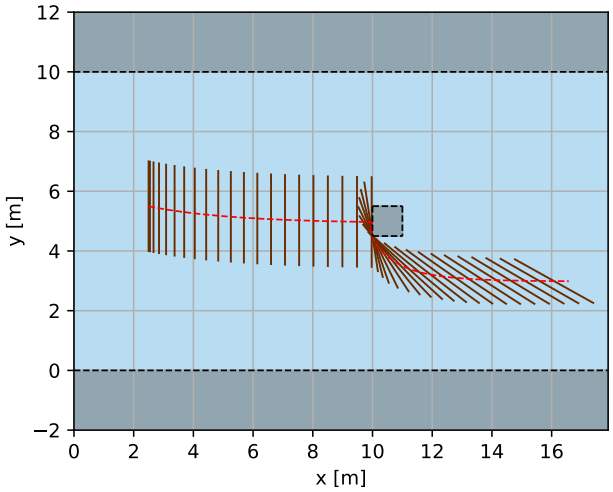

(a) Collision with medium obstacle compared to the cylinder.

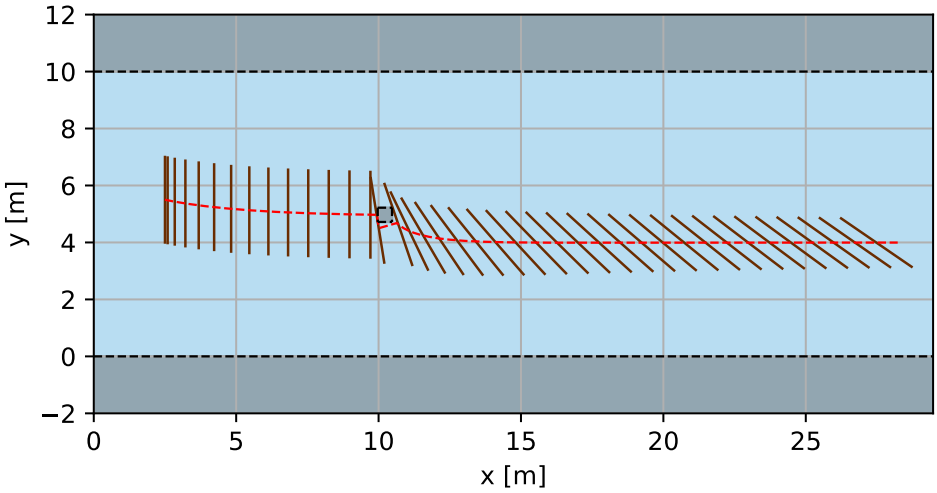

(b) Collision with very small obstacle compared to the cylinder.

Figure 55: Trajectory of floating cylinder in horizontal plane (x, y) with a collision with a smaller obstacle.

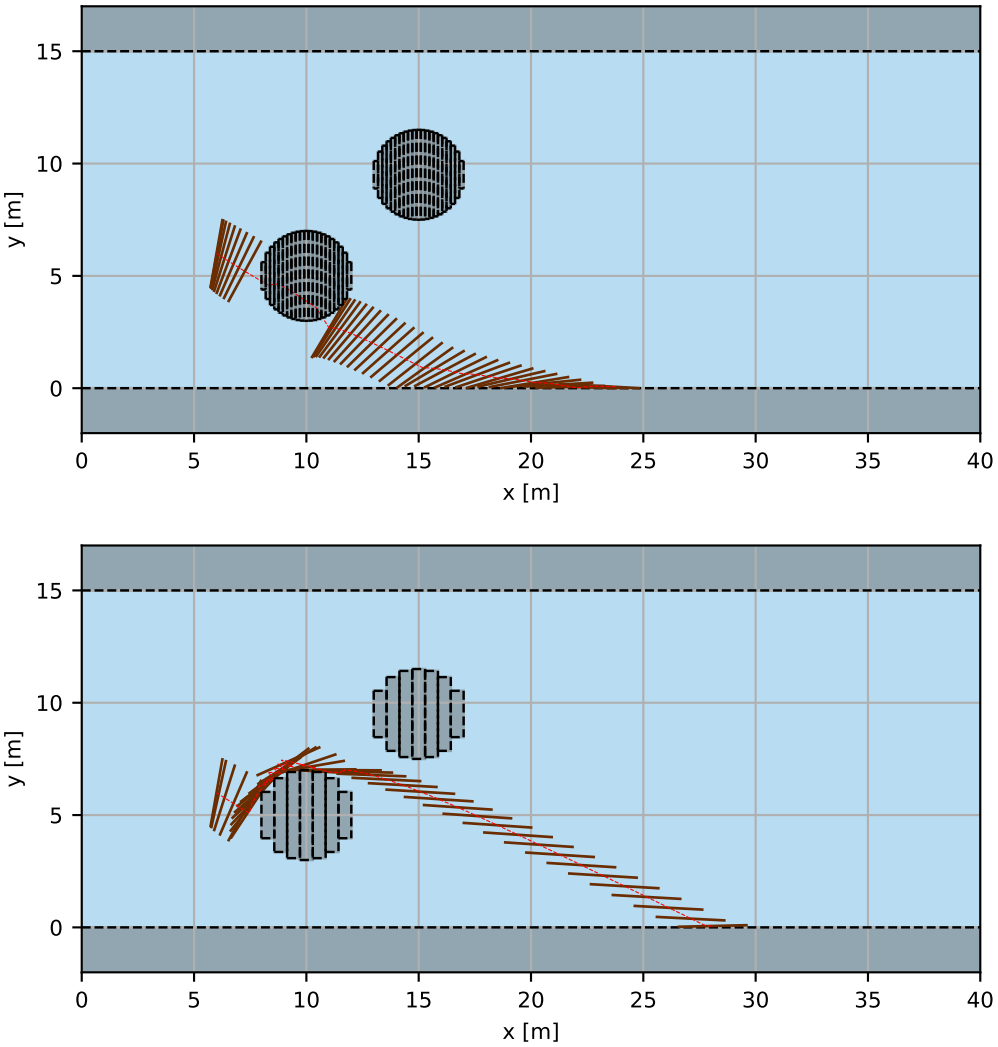

Figure 56: Trajectory of floating cylinder in horizontal plane (x, y) with a collision with a discretized circle $N_r = 7$ and 21).

Part III
Confrontation with established literature

This section encompasses several objectives. Firstly, it aims to demonstrate the code's capability to accommodate more complex flow input data than the steady flows used in the preceding sections. The second goal, which is crucial to this master's thesis, involves the comparison of simulation outcomes with laboratory experiments documented in the literature. This allows a validation of the model. Additionally, a comprehensive error analysis is undertaken.

1 Introduction to the validation

The algorithm simulates the flume experiences at scale 1:1.

2 Reproduction of laboratory experiments

The laboratory experiments of Ruiz-Villanueva et al. (2014) are chosen for this validation phase. The study encompassed a range of scenarios, involving five different cylinder sizes, three distinct initial dowel densities, three varied initial orientations, and five diverse channel geometries. In this section, the different geometries adopted, the resulting hydraulic and flow conditions, and the different cylinder types are presented.

2.1 Floating objects

The type of object used in the Ruiz-Villanueva et al. (2014) experiments are wooden cylinders. More specifically, the article uses 5 different types of object, the characteristics of which are reported in Tab.(19).The cylinder size plays a central role in the forthcoming study, given that the channel size used remains constant (with the exception of obstacle size, which varies according to geometry, as explained in the next section).

Properties \ Type	1	2	3	4	5
L_c [m]	0.1	0.2	0.2	0.5	0.2
r_c [m]	0.010	0.008	0.012	0.010	0.018
ρ_c [kg/m^3]	720	720	720	720	720

Table 19: Description of the five types of cylinder used in the experiments and simulations.

2.2 Eulerian flow field

WOLF[5] software, created by the HECE research group (ULiège), is used to generate the different velocity fields from experiments conducted in the literature. WOLF encompasses a comprehensive suite of numerical models (finite volume approach) designed for simulating both free surface and pressurized flows.

[5]More detailed description available at https://www.uee.uliege.be/cms/c_2383459/fr/wolf

The WOLF simulations were generated and supplied by Clément Delhez (ULiège). The spatial domain was discretized via a mesh of quadrangular elements.

Temporal resolution was achieved using a Runge-Kutta 21 scheme. The simulation was carried out in constant reconstruction until a stationary flow without turbulence model was obtained. This stationary flow was recorded as the initial condition for the flow with turbulence model. Subsequently, a turbulence model (k-epsilon model) is employed for simulation, using the previously explained initial conditions within a linear reconstruction framework. The outcomes are derived from stabilizing this latter flow configuration.

The different velocity data fields are reported in the following sub-subsections. It can be seen that the baffles disrupt the flow, causing variations in velocity across the channel. This non-uniformity in the velocity distribution is a direct result of the deflection and interaction of the fluid with the alternating baffles.

2.2.1 The spacial meshes

Since various geometries are being generated and simulated flow data as well as real flow data are utilized, encompassing various hydraulic conditions, a spatial mesh is needed. The following table (Tab.(20)) shows the different meshes used for each of the geometries presented above. As previously mentioned, a quadrangular element mesh is used. The spacing between two nodes along x (resp. y) is denoted dx (resp. dy). The number of elements along x (resp. y) is denoted nbx (resp. nby).

Charact / Geom	dx [m]	dy [m]	nbx [-]	nby [-]
1	0.01	0.01	1006	66
2	0.02	0.02	1008	36
3	0.02	0.02	1008	36

Table 20: Description of the three different meshes used. *Geom* stands for the geometry type and *Charact* for the characteristics of the mesh.

2.2.2 The geometries and flow fields

Different geometries are tested in the above-mentioned laboratory experiments. The addition of baffles of different sizes for each type of geometry makes it possible to create distinct two-dimensional velocity patterns. The different geometries are discussed below. The experimental setup utilized a flume measuring 0.6 meters in width and 20 meters in length. This flume featured a horizontal slope, which remained consistent across all investigated geometries. However, only the initial 6 meters upstream were employed for conducting the experiments.

Before describing the geometries in detail, the Tab.(21) shows the performed hydraulic conditions.

H.C. / Geom	inlet discharge [Ls^{-1}]	outlet boundary condition (Weir height) [cm]	water depth (max-min) [cm]
1	18	5.8	16-10
2	18	5.8	20-8
3	12	9.7	18-13

Table 21: Description of the hydraulic conditions for the three different geometries (in specific units indicated in square brackets). *H.C.* stands for hydraulic conditions and *Geom* for the different geometries.

The following descriptions present the different geometries. The appendix A.4 gives information about their implementation. In addition, a bilinear interpolation has to be made, as specified in 2.2.3. Its implementation and definition is given in appendix A.3

Geometry 1

The flume is 0.6[m] wide and 10[m] long, the obstacles dimension are 0.15[m] long and 0.2[m] width. They alternate periodically with an offset of the positions of the bottom obstacles, as shown in Fig.(57).

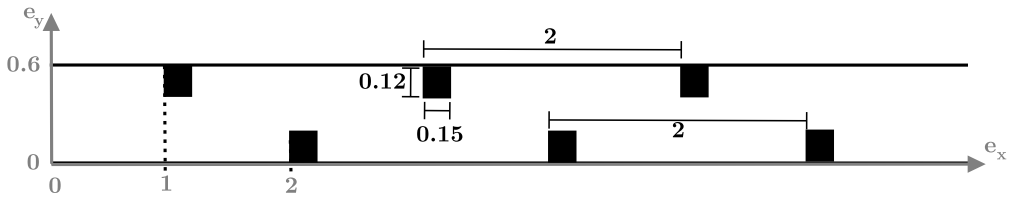

Figure 57: Flume and obstacles dimensions (in [m]) of the experiments in Ruiz-Villanueva et al. (2014) for geometry 1.

The fluid velocity field generated by WOLF with the mesh describe in the Tab.(20) and the conditions of the Tab.(21) is reported in Fig.(58). The white rectangles are the fixed baffles deflecting the flow.

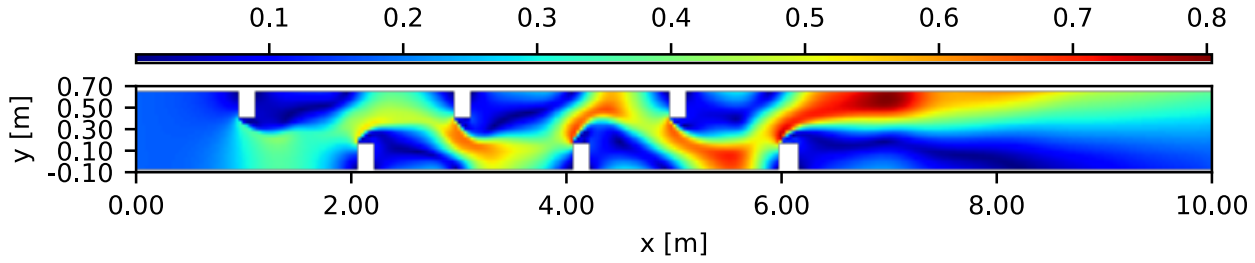

Figure 58: WOLF simulation of the flow velocity field from experiments of Ruiz-Villanueva et al. (2014) for geometry 1.

Geometry 2

The flume is 0.6[m] wide and 10[m] long, the obstacles dimension are 0.3[m] long and 0.12[m] width. They alternate periodically, with an offset between two on the bottom and top walls, as shown in Fig.(59).

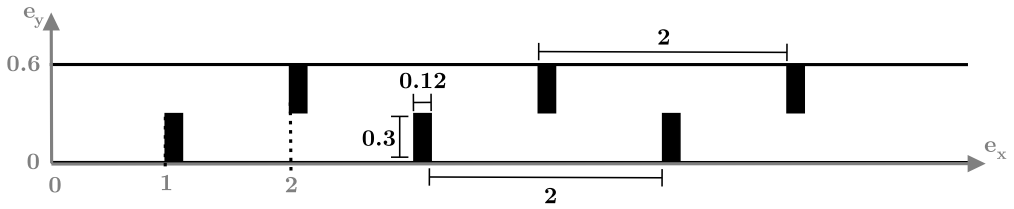

Figure 59: Flume and obstacles dimensions (in [m]) of the experiments in Ruiz-Villanueva et al. (2014) for geometry 2.

The fluid velocity field generated by WOLF with the mesh describe in the Tab.(20) and the conditions of the Tab.(21) is reported in Fig.(60). The white rectangles are the fixed baffles deflecting the flow.

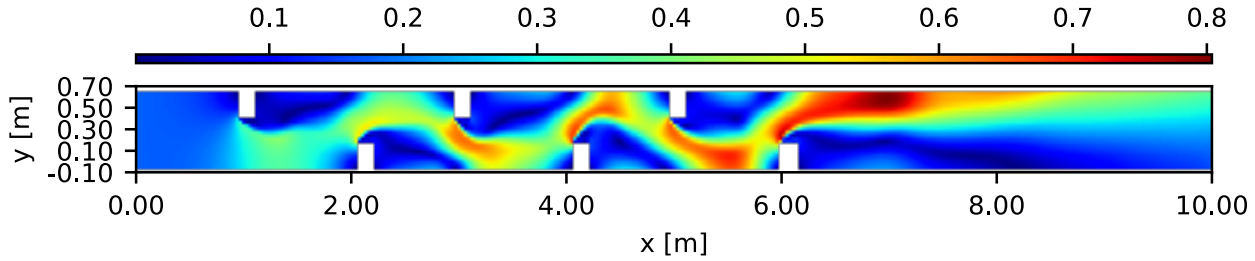

Figure 60: WOLF simulation of the flow velocity field from experiments of Ruiz-Villanueva et al. (2014) for geometry 2.

Geometry 3

The flume is 0.6[m] wide and 10[m] long, the obstacles dimension are 0.15[m] long and 0.4[m] width. They alternate periodically, with an offset between two on the bottom and top walls, as shown in Fig.(61).

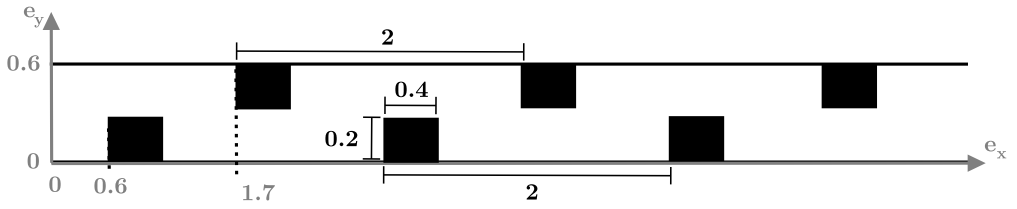

Figure 61: Flume and obstacles dimensions (in [m]) of the experiments in Ruiz-Villanueva et al. (2014) for geometry 3.

The fluid velocity field generated by WOLF with the mesh describe in the Tab.(20) and the conditions of the Tab.(21) is reported in Fig.(62). The white rectangles are the fixed baffles deflecting the flow.

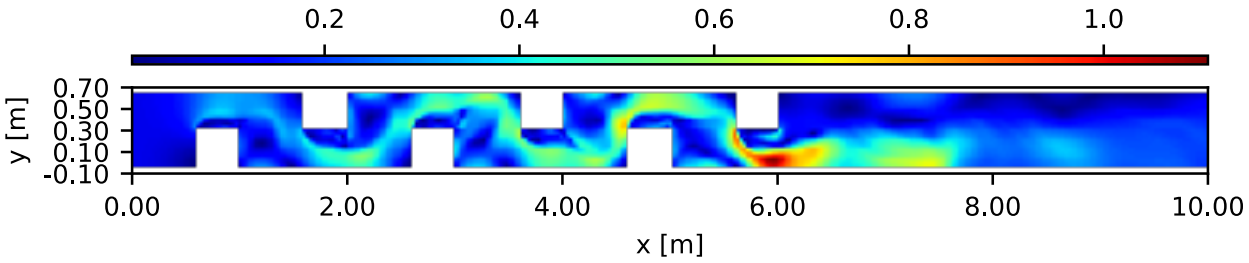

Figure 62: WOLF simulation of the flow velocity field from experiments of Ruiz-Villanueva et al. (2014) for geometry 3.

2.3 Numerical replication of experimental results

In this section, the experimental studies conducted by Ruiz-Villanueva et al. (2014) and confirmed by Persi (2015) are replicated. The choice of cylinder subdivision level is initially justified. Subsequent simulation tests are carried out to closely mimic the selected experiments, and a rigorous comparison of the results is conducted to quantify the level of agreement achieved. Through this assessment, a comprehensive evaluation of the computational model's ability to capture the floating cylinder dynamic is provided.

2.3.1 Choice of the parameters

This section presents the fixed parameters of the simulations. In particular, the choice of the number of cylinder subdisvision is studied.

Choice of N

Firstly, the choice of the cylinder subdivision count is crucial. To achieve this, a calibration based on literature results are performed. The trajectory of a cylinder type 2^6 within the geometry 1 is simulated and compared against the findings of Ruiz-Villanueva et al. (2014) and Persi (2015). A convergence of the trajectory is expected as N increases. Moreover, the error is anticipated to decrease as a decreasing function of N, since this parameter enables a more accurate assessment of the surrounding fluid. Finally, a balance must be found between the minimum error and the computation time needed to run the code within a respectable timeframe. First of all, the trajectories for different value of N are reported in the Fig.(63).

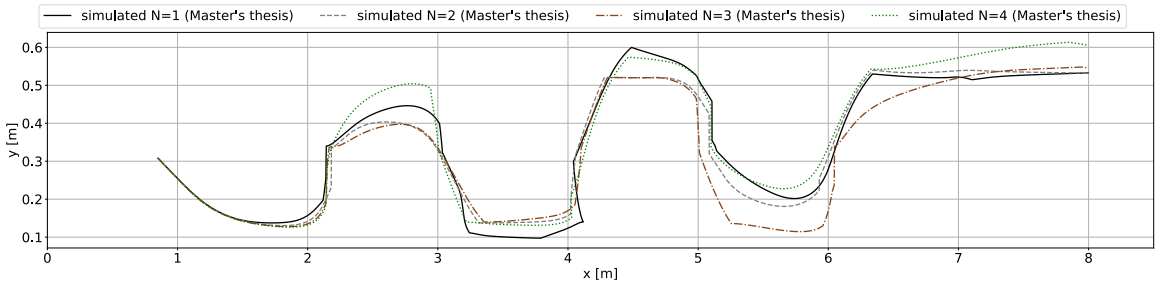

Figure 63: Computation time in function of the number of sub-parts.

[6] As a reminder, $L_c = 0.2$[m], $r_c = 0.008$[m] and ρ_c=720[kg/m^3]

To provide an additional criterion for selecting the number N, the calculation time is plotted as a function of this number in Fig.(64). It can be seen that favoring a large subdivision is more time-consuming.

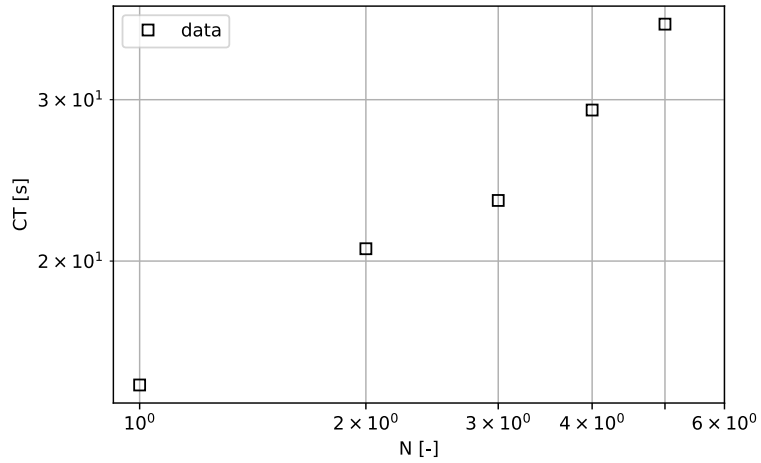

Figure 64: Computation time in function of the number of sub-parts. The more the cylinder is divided, the longer the calculation time.

Persi (2015), who suggests this subdivision method, advises choosing N equal to 4. This may seem a good choice, since the trajectory simulation seems to record the other cases of N and still keep the computation time reasonable.

Other parameters

Then, the coefficient of restitution ϵ is set at 0.1[-] for every simulations, in line with the value calibrated experimentally by Persi (2015). A sensitivity study of this parameter is presented later in the subsection 3. The, the time step is set to 0.01[1] for the same reasons as for Part 2. Finally, other parameters as the geometry, the geometrical and physical properties of the cylinders vary and are specified for each simulation.

2.3.2 Alignment validation

The initial validation tests were conducted to assess the accuracy of the simulation in the cylinder motion, encompassing both translational and rotational aspects. The trajectory is studied to see if cylinder alignment is well predicted. Then, for each case, a comparison with the simulated model of Ruiz-Villanueva et al. (2014) is performed. Finally, a RMS error analysis in the y-direction is provided. To do so, a cylinder was introduced in the flume, with various orientations : 45, 90 and 180 degrees. The initial position of the center of mass is set to (0.675,0.450)[m]. The trunks should tend towards their equilibrium position, i.e. the position parallel to the direction of flow. In addition, the trajectory is expected to follow the maximum velocity Ruiz-Villanueva et al. (2014). This test is performed with geometry 3 and a type 1 cylinder, discretized in 4 sub-parts.

Maximum initial alignment case

First of all, the cylinder is placed with no inclination to the flow. The obtained the trajectory is given in Fig.(65).

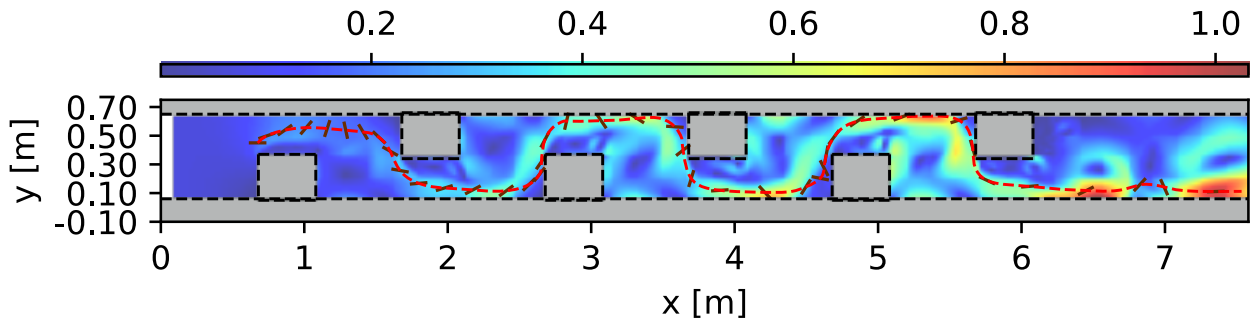

Figure 65: Trajectory in the (x,y) plane of a type 1 cylinder, in geometry 3, oriented initially at 180°.

By superimposing the velocity field on the trajectory, it can be confirmed that the cylinder does indeed follow the higher velocity streamlines. In particular, cylinder rotation is greater in higher-speed areas, since the torque applied to the cylinder is greater. For example, after 5[m] in x-direction (except in recirculation zones, far from the last obstacle), it is clear that good alignment is taking place. In addition, the cylinder, initially at rest, is driven away quite smoothly, since collisions only occur at the third obstacle.

By comparing these data to the study conducted by Ruiz-Villanueva et al. (2014), the graphs in Fig.(66) are computed. Overall, the trajectory has the same characteristics, with the exception of a greater vertical motion, where the cylinder is carried to higher positions. In addition, the RMS error in the y-direction has been estimated at 0.0095, confirming the differences between the simulations (order of magnitudes of 0.1 in the y-direction). These differences could arise from the flow, which appears to exhibit variations compared to the literature.

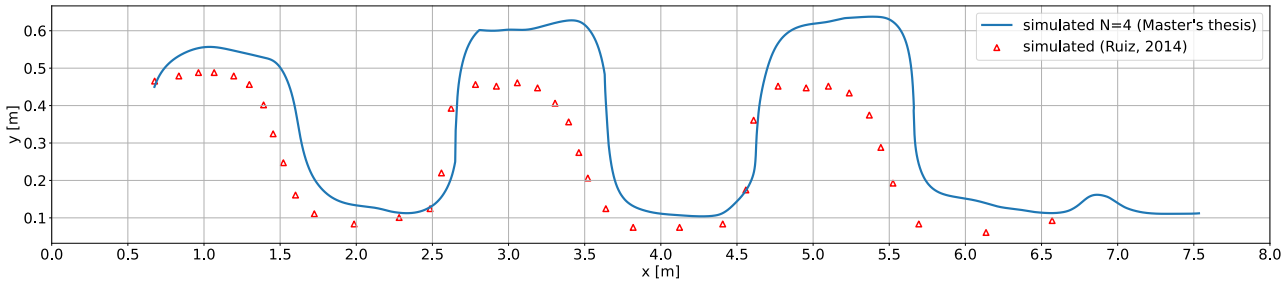

Figure 66: Comparison with the results of Ruiz-Villanueva et al. (2014) of the trajectory in the (x,y) plane of a type 1 cylinder, in geometry 3, oriented initially at 180°.

Minimum initial alignment case

Secondly, the same study was carried out for a cylinder initially perpendicular to the flow. The Fig.(67) shows that, unlike the previous case, the cylinder rotates quite fast on the first meter without reaching an equilibrium position. In fact, 90° corresponds to an unstable equilibrium, and the cylinder quickly begins to undergo an important torque, leading it to 180°. As it approaches 3[m] in x-direction, it reaches a position of equilibrium, which it maintains despite variations in flow velocity, as in the previous simulation.

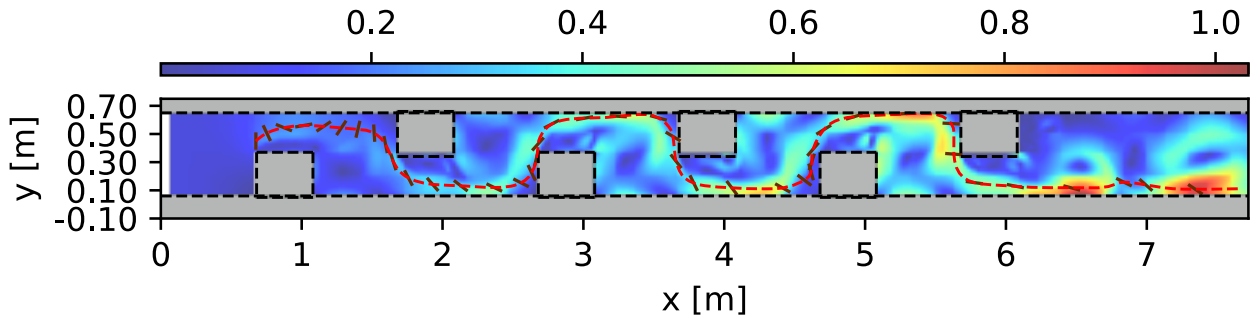

Figure 67: Trajectory simulated for the motion validation through the study of the trajectory in the (x,y) plane of a type 1 cylinder, in geometry 3, oriented initially at 90°.

Next, graphs equivalent to the first simulation are plotted in Fig.(68) to compare the simulated trajectory with that of the simulations of Ruiz-Villanueva et al. (2014). The RMS error in this case (in the y-direction) is 0.0182. The error is higher than before, probably because the motion is less stable, since the cylinder has to rotate more than in the previous case.

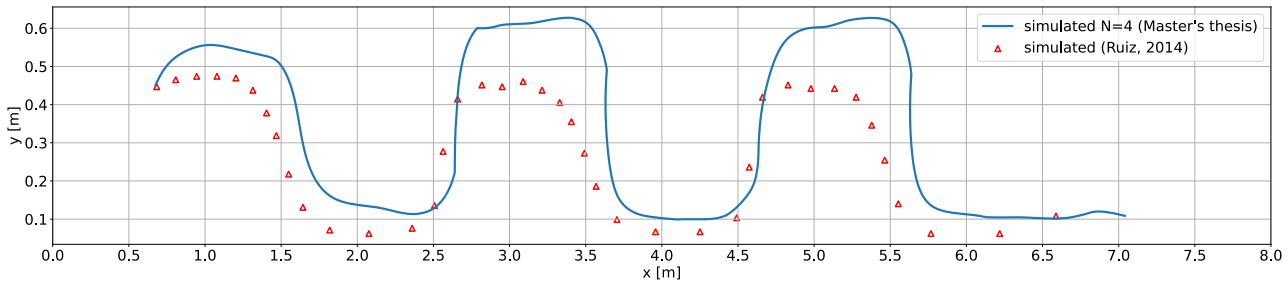

Figure 68: Motion validation through the study of the trajectory in the (x,y) plane of a type 1 cylinder, in geometry 3, oriented initially at 90°. Comparison with the results of Ruiz-Villanueva et al. (2014).

Intermediate alignment case

Finally, the same study was carried out for a cylinder initially oriented at 45° to the flow. The Fig.(69) shows the cylinder quickly begins to undergo torque as it is not initially at its stable equilibrium position. As it is less exposed to the flow than at 90°, the torque it undergoes is of lower intensity.

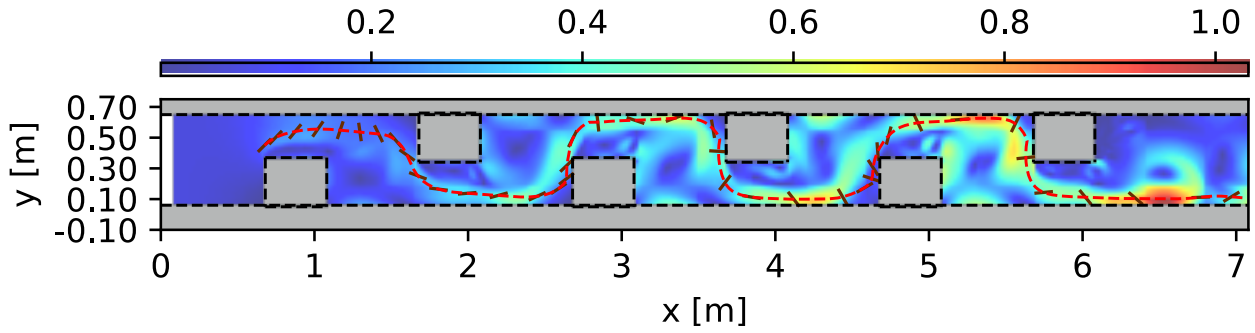

Figure 69: Trajectory simulated for the motion validation through the study of the trajectory in the (x,y) plane of a type 1 cylinder, in geometry 3, oriented initially at 45°.

A comparison with the Ruiz-Villanueva et al. (2014)'s simulation is shown in Fig.70. The calculated RMS error (in the y-direction) is 0.0112. The error is lower than that observed for the 90° scenario but greater than that for the 180° scenario. This outcome is reasonable, given that this represents the intermediary case where the cylinder necessitates a relatively intricate rotational adjustment to align with the flow, albeit to a lesser degree than in the 90° scenario.

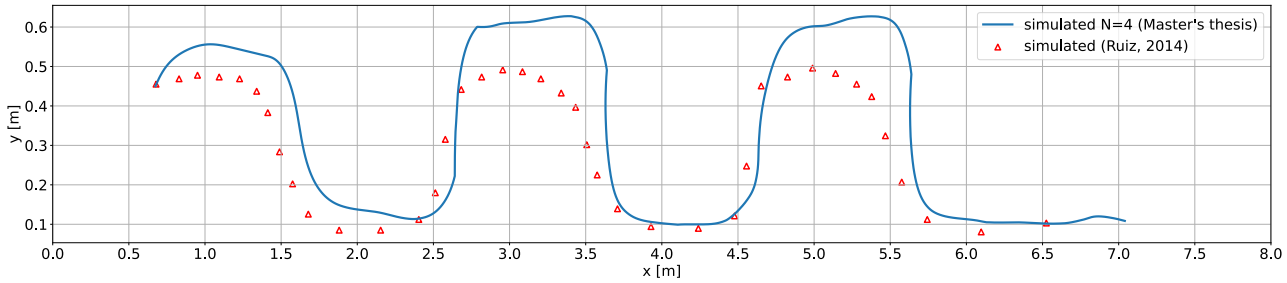

Figure 70: Motion validation through the study of the trajectory in the (x,y) plane of a type 1 cylinder, in geometry 3, oriented initially at 45°. Comparison with the results of Ruiz-Villanueva et al. (2014).

Conclusion

In all scenarios, the cylinder follows the line of maximum flow velocity. Cylinders positioned parallel to the flow direction maintain an equilibrium position more easily at the beginning of the motion than in other cases. In the latter case, the cylinder must first undergo torque to rotate until it eventually reaches its stability. Once equilibrium is attained, the cylinder tends to remain in that position, except during transitions (meanders) where torques disrupt its balance. Stability is regained when it enters a zone of maximum velocity. In conclusion, this test has confirmed that cylinder alignment is still well-managed, despite the introduction of more complex flow patterns.

2.3.3 Kinetics validation

The trajectory is studied again in this section, with an additional focus on time dependency. The aim of this test is to assess whether the object moves not according to the same trajectory, but within a time interval close to the literature. Geometry 1 and 2 are employed individually, with the utilization of cylinder type 2.

Geometry 1

First of all, the trajectory calculated in the previous section for N=4 is compared with Persi (2015)'s simulations and Ruiz-Villanueva et al. (2014)'s experiments and simulations. Fig.(71) shows the superposition of different trajectory predictions.

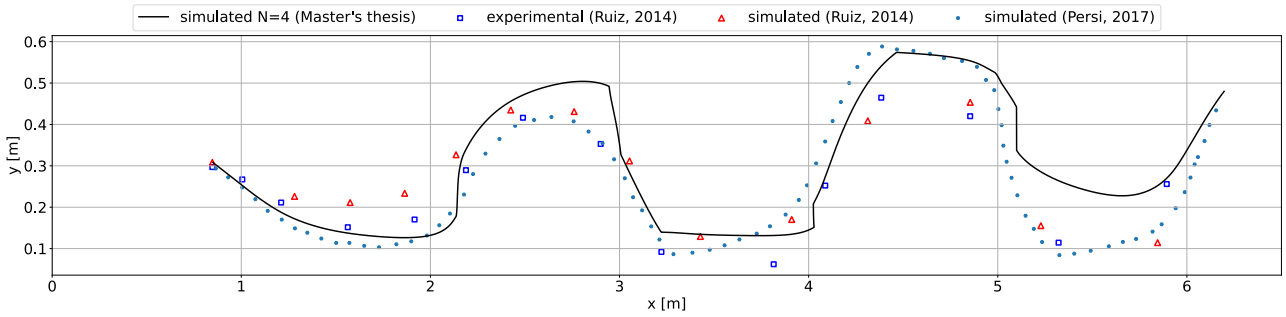

Figure 71: Comparison of the trajectories for geometry 1 with Persi (2015)'s simulations and Ruiz-Villanueva et al. (2014)'s experiments and simulations.

It can be observed that the trajectory calculated by the code seems to follow the one computed by Persi (2015)'s predictions, unlike a collision with the first obstacle of the bottom, which gives the simulated cylinder a different dynamic after 2[m]. Directly after this first collision, the code is closer to Ruiz's prediction. However, the consequence of the collision fades and joins the predictions of Persi (2015) again. Tab.(22) shows a study of the error in the y-direction, by using the definition given previously in Eq.(64). The code curve deviates most from the experimental curve, but the order of magnitude of the RMS error is acceptable. By way of comparison, the difference between the simulated model and Ruiz-Villanueva et al. (2014)'s experiments is 0.096.

Comparison	C-P	C-R lab	C-R sim
RMS	0.0111	0.0106	0.0005

Table 22: Root mean square error (RMSE) in the y-direction for the trajectory for geometry 1 predicted by the code (C), Ruiz-Villanueva et al. (2014)'s experiments (R lab) and simulations (R sim) and Persi (2015)'s simulation (P).

Then, the graphs of vertical position versus time can be compared. For this comparison, Persi (2015)'s data are not available. The comparison is shown in Fig.(72). A temporal shift is noticed at the end. The code simulates the cylinder taking more time to traverse the entire length of the channel compared to what is reported in the article. A plausible explanation would be the presence of a collision, visible at the sudden change of trajectory, that slows the object down when it is partly blocked by one of the obstacles. This problem is investigated when the second geometry is studied.

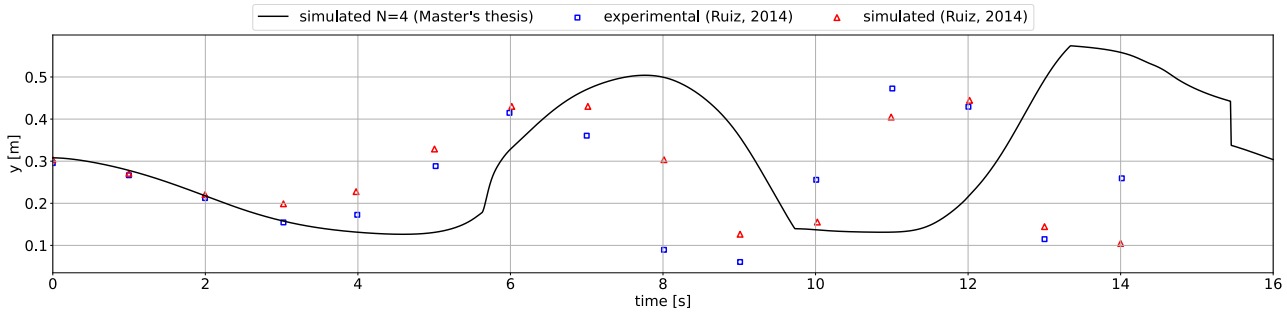

Figure 72: Comparison of the vertical position for geometry 1 in function of time with Ruiz-Villanueva et al. (2014)'s experiments and simulations. A time lag is noticeable.

Geometry 2

Secondly, the same tests are performed with the geometry 2. For this geometry, Persi (2015) does not perform any tests.

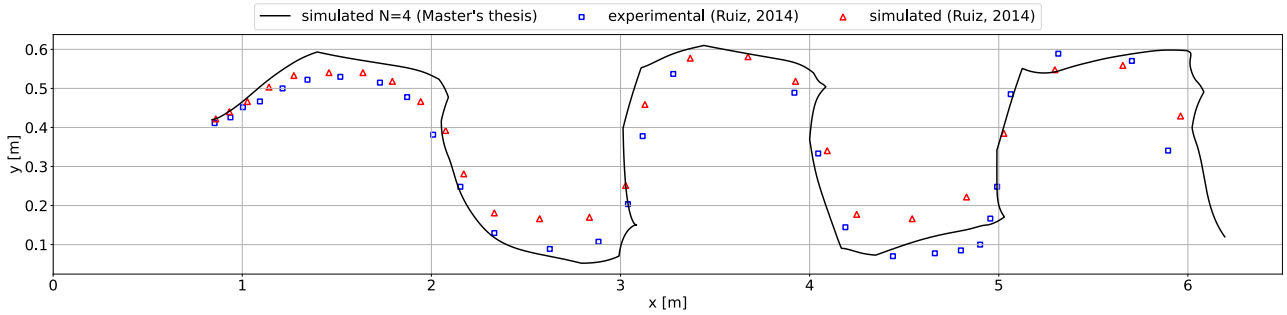

Figure 73: Comparison of the trajectories for geometry 2 with Ruiz-Villanueva et al. (2014)'s experiments and simulations.

The trajectory simulated by the code is fairly close to the laboratory experiments and simulations one. Once again, the RMSE in the y-direction is computed in Tab.(23).

Comparison	C-R lab	C-R sim
RMS	0.0090	0.0017

Table 23: Root mean square error (RMSE) in the y-direction for the trajectory predicted by the code (C), Ruiz-Villanueva et al. (2014)'s experiments (R lab) and simulations (R sim) for geometry 2.

As with geometry 1, the graphs in Fig.(74) are plotted. A time lag is once again noticeable. This observation is therefore common to both sets of available data and is investigated in the following discussion section.

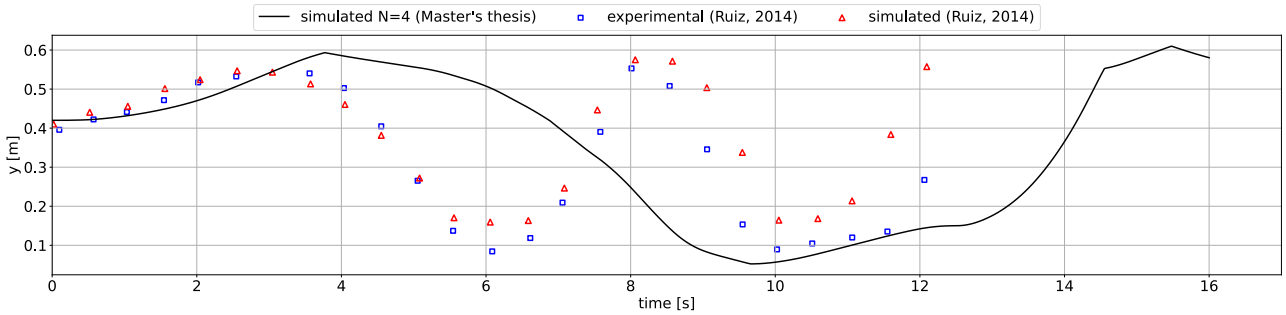

Figure 74: Comparison of the vertical position in function of time with Ruiz-Villanueva et al. (2014)'s experiments and simulations for geometry 2.

Discussion and hypothesis

The predicted trajectories generated by the code exhibit a certain resemblance to the curves documented in the literature. However, it is worth noting that divergences have emerged, notably due to the anticipation of additional collisions. These extra collisions have an impact on the total time required for the cylinder to traverse the channel.

These observations suggest that these divergences could be attributed to an approximate assessment of the forces at play. Specifically, this estimation of forces could suffer from a bias, either underestimating or overestimating their intensity. In the case of underestimation, the driving force applied to the object might be insufficient, leading to inadequate speed convergence and thus slower-than-expected displacement. Conversely, in the case of overestimation, collisions could occur more frequently compared to the comparative models. Based on the collisions observed in the trajectories, the second option appears to be the most plausible one. Indeed, the repeated collisions encountered along the trajectory seem to indicate an excessive estimation of forces, which would contribute to the observed differences compared to other reference models.

The source of this poor estimation could arise from the drag and side coefficients used. In fact, the literature lacks of documentation on these coefficients. Those from Persi (2015) were employed, assuming a semi-submerged object. This assumption was made to align with the coefficient sets of the latter article. They encompass coefficients for fully submerged objects (both deep and shallow) as well as semi-submerged ones. The chosen cylinder density was 720 [kg/m^3], rendering this assumption plausible. However, since the article does not provide a temporal study, it is impossible to verify its predictive consistency. The following section studies the impact of such coefficients.

However, an area of investigation concerns collisions detection. Given that the trajectory largely mirrors those in the literature, it's conceivable that post-collision adjustments overly affect the object's dynamics. The following section also studies the effect of the coefficient of restitution parameter, in order to explore this hypothesis in greater detail.

3 Original studies

The aim of this section is to study some parameters such as the cylinder's coefficient of restitution, its size or its coefficients.

3.1 Study of the restitution coefficient

This subsection aims to make an analysis of the restitution coefficient. To investigate this, the coefficient of restitution ϵ, set at 0.1 as in Persi (2015), is altered to 0.1, 0.25, 0.5, 0.75 and 1 to assess its impact. First, the impact of the temporal aspect of the object's drift is sought. To quantify it, the Tab.(24) is provided, indicating the time required for the cylinder to cover a distance of 6.03[m] in the x-direction (corresponding to the end of the last obstacle), denoted $t_{x=6.03}$. The largest discrepancy concerns the value of 0.1, which corresponds to the value chosen in the models. However, the deviations are of the order of a second, which doesn't seem to have too much impact on the temporality of the drift.

ϵ [-]	**0.1**	**0.25**	**0.5**	**0.75**	**1**
$t_{x=6.03}$ [s]	19.21	23.07	21.62	21.69	21.31

Table 24: Time required for a type 2 cylinder to cover the distance une the last obstacle (6.03[m]) in the x-direction in geometry 2.

Then, the trajectory graphs are shown in Fig.(75).

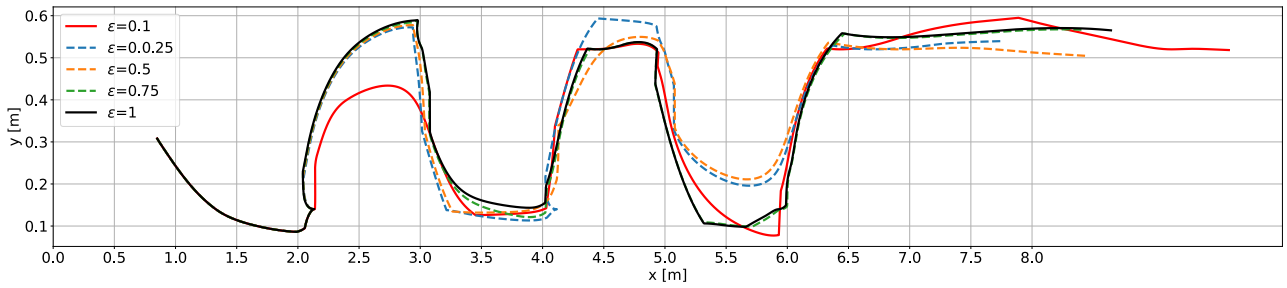

Figure 75: Trajectory in the (x, y) place of a cylinder type 2, in geometry 2 during 25[s].

Here, the trajectory is really affected by the coefficient of restitution. In particular, it has been observed that the more elastic the collision, the more the object bounces off obstacles and the more its trajectory is modified. In particular, the collision with the first obstacle changes drastically for $\epsilon = 0.1$. Another example is the collision at 3[m] in the x-direction. With $\epsilon = 1$ the object bounces off and then collides at a corner with the obstacle, whereas other values of ϵ avoid the corner collision by simply sliding.

In summary, it is evident that that the restitution coefficient has an impact on the object's dynamics, its trajectory and, to a lesser extent, its temporality. The larger the coefficient of restitution, the greater the deviation of the cylinder. Increasing the value of this coefficient has an impact on its temporality of the order of a second for this simulation. As the observed discrepancy in the preceding section within the Figs.(72, 74) were in the order of the order of ten seconds, this cannot be attributed to the coefficient of restitution.

3.2 Effect of the cylinder's size

From the outset, the size of the cylinder has never been studied. In Part II, it was set at L_c =3[m] and r_c =0.25[m]. In Part 3, only Ruiz-Villanueva et al. (2014)'s types 1 and 2 were used. In this subsection, a study of cylinder size is carried out. First, the trajectories of the five different types of cylinder are simulated in geometry 1. Then, the largest cylinder (type 4) used by Ruiz-Villanueva et al. (2014) is simulated.

3.2.1 Study of different sizes

For this study, Geometry 1 is maintained throughout, and the trajectories of all cylinder types listed in Table (19) is depicted in Fig.(76). The simulation encompasses a time span of 25[s]. As intuitively anticipated, for a given flow and geometry, the size of the cylinder yields markedly distinct trajectories. Particularly noteworthy is that type 2 exhibits the longest travel distance, while type 5 becomes trapped near the obstacle at 3.5[m] in the x-direction. The largest cylinder, type 4, covers approximately the same distance as its neighboring types, despite more frequent collisions. Additionally, some trajectories reach lower heights than others. This can be explained either by the fact that, for instance, type 1 more readily floats, whereas for type 4, its size prevents its center of mass from reaching the boundary.

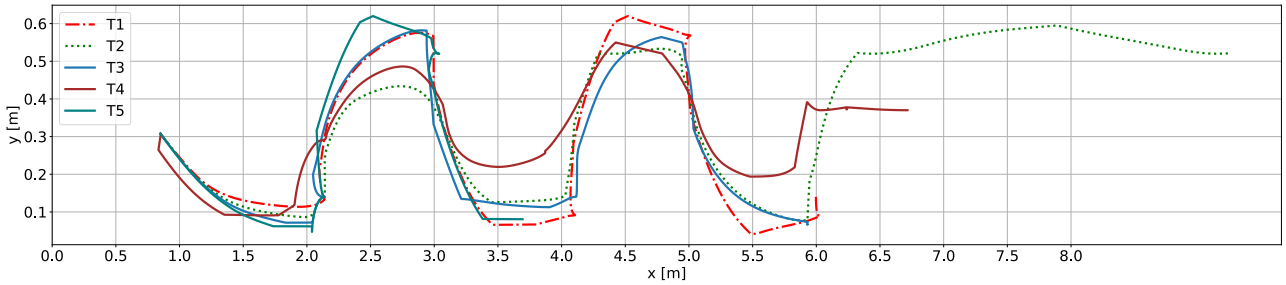

Figure 76: Trajectories of type 1,2,3,4 and 5 in geometry 1 during 25[s]. T stands for type. Given a specific flow and geometry, the cylinder's size results in significantly varied trajectories.

3.2.2 Study of a larger cylinder

In practice, the initial position of the cylinder's center of mass is always set to (0.85,0.3), at rest and inclined at 45°. The simulations lasts 25[s]. The first geometry gives the Fig.(77). It can be observed that length, greater than half the width of the flume, implies particularly numerous collisions. Its trajectory is constantly impacted by these. This observation never applied to smaller cylinder types.

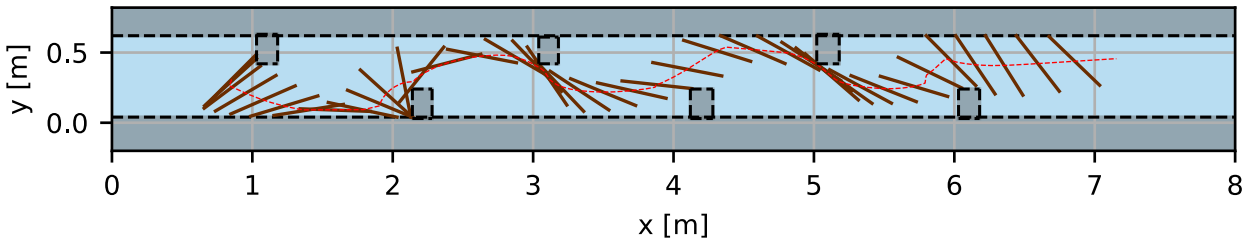

Figure 77: Simulation of geometry 1 for a larger type of cylinder (type 4). Its trajectory is entirely dictated by the correction of its collisions.

For the geometry 2, the trajectory is depicted in Fig.(78). For the first time using Ruiz-Villanueva et al. (2014)'s geometries, the object is unable to navigate through the obstacles. It is entrapped within the fluid recirculations and repeatedly collides.

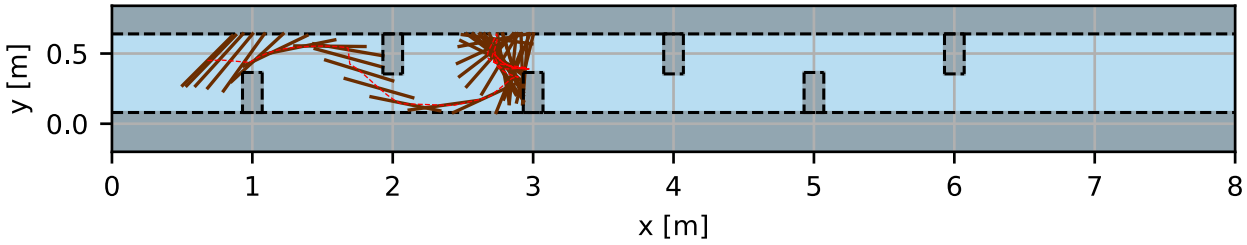

Figure 78: Simulation of geometry 2 for a larger type of cylinder (type 4). Its trajectory is entirely dictated by the correction of its collisions.

The third geometry, simulating even larger obstacles, seems an interesting one to study in view of the simulation on geometry two. The calculated trajectory is shown in Fig.(79). The observation here is markedly distinct. The object becomes wedged between the fluid propelling it and the obstacle restraining it. Indeed, its position dictates an upward and rightward push, while in its path lies the obstacle. This represents the first and sole simulated instance of clogging using the geometries from the article.

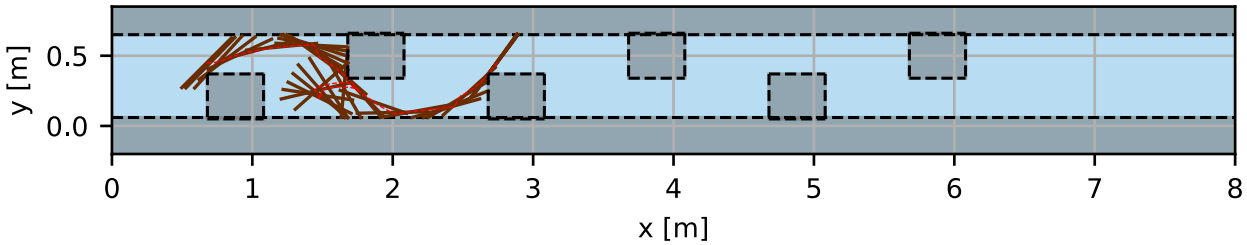

Figure 79: Simulation of geometry 3 for a larger type of cylinder (type 4). Its trajectory is entirely dictated by the correction of its collisions.

4 Conclusion and future prospects

A comparison of the simulation by the developed code with simulated and experimental results from the literature was carried out. Similarities between the results were highlighted, with an error analysis showing a fairly reliable model. Cylinder orientation could not be directly compared, due to a lack of data in the literature. However, the fundamental results of the dynamics of a floating cylinder were found, such as the fact that it generally follows the current lines at higher speeds and aligns itself with the flow. This confirms the effectiveness of the dynamic model, including the discretization of the spatial domain for procedure subdivision.

In addition, this comparison made it possible to simulate the collision model on a real flow. All collisions appear to be detected and corrected, thus impacting the object dynamics. A study was carried out to see the impact of these collisions on the object's dynamics, both spatially and temporally, as well as on the effect of certain parameters such as the coefficient of restitution.

The simulated laboratory experiments were not specifically designed to simulate clogging. Therefore, additional simulations were performed using a longer cylinder, for example. The results showed pure clogging situations, where the cylinder gets stuck between two obstacles, but also situations where it perpetually collides and is caught in the fluid's recirculation cells, making it impossible to pass certain obstacles.

These latest results are encouraging for the prospects of globalizing the code to model several cylinders. Indeed, clogging is most often caused by the accumulation of several pieces of floating debris (Ruiz-Villanueva et al., 2014). So it is optimistic to think that results where the cylinder is slowed down in its overall motion, trapped before an obstacle or simply stuck, could lead to realistic clogging simulations with multiple cylinders.

However, the code still operates under important assumptions such as unaccounted turbulence and stationary flows. Removing these assumptions could in future give the code the opportunity to get closer to reality.

Conclusion

In conclusion, this master's thesis constitutes an initial contribution to the two-dimensional numerical modeling of the drift of large floating objects on rivers. The fundamental objective of this study was to investigate the involved physical phenomena and to develop a model incorporating them. Particular attention was paid to predict clogging due to the object being blocked by various obstacles.

The study was divided into three parts. The first involved a review of the literature, allowing to study the various existing models and justifying the hypothesis of the model to develop. The latter was presented in the second part, both for object dynamics and collisions. This part presented complete original approach for representing obstacles, as well as for detecting collisions and simulating them. Finally, the third part validated the model and studied the behavior of a floating cylinder under numerically reproduced laboratory conditions.

Two simulation phases were performed. The first phase concerned simulations under a hypothetical flow to study the object's dynamics, before and after collisions. The second aimed to simulate flows from laboratory experiments. They have shown multiple results. First, clogging situations were analyzed in both phases. Then, the simulations showed that the algorithm reproduces experimental results and literature simulations with fidelity. In addition to validating the object dynamics, this part showed the effectiveness of the code in handling collisions, despite more complex geometries and flows.

As a final application, collision simulations were used to study clogging. The simulations have demonstrated the code's ability to handle multiple collisions with various obstacles, which is a key result for clogging simulation. This event was studies under different flows and geometries but also with different cylinders. In particular, relationship between the geometry through which the flow passes and the size of the object is a key factor for obstructions. In addition to direct clogging, simulations with multiple obstacle geometries have shown temporary blocking of the object.

With regard to the model's limitations, the code's performance could be improved. Indeed, this limits the collision detection model, which would require a variable time step for greater accuracy. It also severely limits the model's generality in generating obstacles of complex shapes dicretized through the developed obstacle model. Another limitation is concerns the collision model that requires precise knowledge of the terrain, limiting applications of the code to a local scope.

In terms of future prospects, a generalization of the code to the simulation of several floating objects could be a direct further study. Indeed, clogging situations occur more often when several floating objects interact with each other, as shown by the experiments in Ruiz-Villanueva et al. (2014). It is quite optimistic to expect that this kind of clogging will be possible to simulate. Indeed, the code is already capable of simulating temporary clogging. Ultimately, application to real flooding scenarios could be sought, in particular for a systematic study of clogging around bridges.

Extending the study may require the use of laboratory simulations, for which data are rarely available in the literature. Indeed, while the study of floating object's drift has been explored by different research teams, such as (Ruiz-Villanueva et al., 2014), (Mandø and Rosendahl, 2010) and (Persi, 2015), it still lacks an exhaustive collection of experimental data.

Continuing to explore these research paths, accounting for current limitations and identified areas of improvement, this study could potentially represent a first step towards a code capable of aiding the management of scenarios involving the drift of floating objects in real and potentially hazardous environments.

Appendix

A Algorithm overview

The aim of this small section is to present the structure of the code provided. It follows the general outline shown in Fig.(19) in the introduction, and requires a hierarchy in the steps presented. The programming language used is `Python`[7].

A.1 Algorithm modules overview

Each of the files created and its specific features is detailed here. The code was built around 5 files. Each of them is presented briefly.

The definition files

This refers to the part of the code that processes the data and defines functions for the processing part. In this code, it includes `definitions_functions.py` and `Read_Wolf_results.py`.

`definitions_functions.py` encodes all functions and definitions relating to the cylinder's geometric (e.g L, r_c) and physical properties (e.g ρ_c, I_c, S_d). It also includes the definitions of the different flumes (macroscopic one and Ruiz-Villanueva et al. (2014)'s experiment flume) and obstacles (e.g baffles, circles and square obstacles). Finally, it gives all the definitions of force, torque and equations required for the model. In particular, it writes the right-hand members to be solved via RK2.

`Read_Wolf_results.py` It extracts and processes data simulated by `WOLF` from the actual velocity field of the flow from Ruiz-Villanueva et al. (2014) experiments. It returns the stationary field data in a three-dimensional array.

`collision.py` takes as input the cylinder's position and orientation and its dynamic variables (e.g. linear and angular velocities). It then applies collision detection and corrections if necessary. It returns its updated input parameters.

The processing

Processing refers to the file that performs the actual calculations. It is called `main.py`. It calls on all the other files to provide it with the parameters and functions it needs to function. It then solves the model equations via RK22 within the specified time interval, and saves the parameters to be processed in postprocessing.

The postprocessing

Postprocessing refers to the treatment of data acquired by processing. It's simply the `plots.py` file that gathers the functions of the desired plots and GIFS.

[7] This choice is not driven by any particular reason other than the opportunity to learn and explore this language through this Master's thesis

A.2 RK22 implementation

This subsection present the Runge-Kutta order 2, 2 iterions method used for the time resolution of the equations. Using the following simplified writing, where RHS_T (resp. RHS_F) stands for right-hand-side of Eq.(2) (resp.Eq.(1)), the system rewrites as in Eq.(67).

$$\begin{cases} \dfrac{d\theta}{dt} = \boldsymbol{\omega}, \\ \dfrac{d^2\theta}{dt^2} = \dfrac{d\boldsymbol{\omega}}{dt} = RSH_T(\mathbf{v},\boldsymbol{\omega},\theta), \\ \dfrac{d\mathbf{v}}{dt} = RSH_F(\mathbf{v},\theta). \end{cases} \tag{67}$$

By denoting the time step h and t_{phys} the physical time (time at which the code must stop solving the equation), each RSH is evaluated at the initial time as

$$k_1^{\theta} = h \cdot \boldsymbol{\omega}, \tag{68}$$
$$k_1^{\omega} = h \cdot RSH_T(\mathbf{v},\boldsymbol{\omega},\theta), \tag{69}$$
$$k_1^{v} = h \cdot RSH_F(\mathbf{v},\theta). \tag{70}$$

This correspond to the evaluation of the initial slopes. Then, the intermediate values are computed as

$$\theta_{\text{inter}} = \theta_i + wk_1^{\theta}, \tag{71}$$
$$\boldsymbol{\omega}_{\text{inter}} = \boldsymbol{\omega}_i + wk_1^{\omega}, \tag{72}$$
$$\mathbf{v}_{\text{inter}} = \mathbf{v}_i + wk_1^{\mathbf{v}}, \tag{73}$$

to allow the computation of the second evaluation

$$k_2^{\theta} = h \cdot \boldsymbol{\omega}_{\text{inter}}, \tag{74}$$
$$k_2^{\omega} = h \cdot RSH_T(\mathbf{v},\boldsymbol{\omega}_{\text{inter}},\theta_{\text{inter}}), \tag{75}$$
$$k_2^{v} = h \cdot RSH_F(\mathbf{v},\theta_{\text{inter}}). \tag{76}$$

The solution at the next time step is thus given by

$$\theta_{i+1} = \theta_i + wk1^{\theta} + (1-w)k_2^{\theta}, \tag{77}$$
$$\boldsymbol{\omega}_{i+1} = \boldsymbol{\omega}_i + wk1^{\omega} + (1-w)k_2^{\omega}, \tag{78}$$
$$\mathbf{v}_{i+1} = \mathbf{v}_i + k_2^{\mathbf{v}}, \tag{79}$$

where indices i and $i+1$ refer to the current and next time steps, respectively, which gives the method its explicit characterization.

The implemented algorithm uses $w = 0$ to retain the RK22 method and keep superior precision

A.3 Bilinear interpolation

Interpolation

A bilinear interpolation is used to interpolate a velocity field (u_x, u_y) at a given position (x_{CM}, y_{CM}). As a reminder, the mesh uses quadrangular elements. The spacing between two nodes along x (resp. y) is denoted dx (resp. dy). The number of elements along x (resp. y) is denoted nbx (resp. nby).

The first step consists in finding neighboring node indices i and j by using the Eq.(80). If the operation $\texttt{int}(\cdot)$ truncates the result to unity, one has

$$i = \texttt{int}\left(\frac{x_{CM}}{dx}\right), \quad j = \texttt{int}\left(\frac{y_{CM}}{dy}\right). \tag{80}$$

Then, the Eq.(81) ensures that the indices stay within the valid range by constraining :

$$i = \texttt{max}(0, \min(i, \text{nbx} - 1)), \quad j = \texttt{max}(0, \min(j, \text{nby} - 1)). \tag{81}$$

The second step computes the interpolation weights w for each neighboring node based on the inverse of the distances d_{N_k}. The distance is trivially computed through the Eq.(82). By denoting trough N_k the k-th node, one has

$$d_k = \sqrt{(x_{CM} - x_{N_k})^2 + (y_{CM} - y_{N_k})^2}. \tag{82}$$

Then, the Eq.(83) computes the weight w for the interpolation. By denoting by τ a small threshold value to avoid division by zero for very small distances, one has

$$w_k = \begin{cases} \frac{1}{d_k}, & \text{if } d_k \geq \tau \\ 0, & \text{otherwise.} \end{cases} \tag{83}$$

The third step is given by the Eq.(84) that normalizes the weights as

$$\begin{cases} w_k^{(1)} = \dfrac{w_k}{w_{\text{tot}}} \\ w_{\text{tot}} = \displaystyle\sum_k w_k. \end{cases} \tag{84}$$

Finally, the interpolated velocity components $(u_{x,\text{interp}}, u_{y,\text{interp}})$ is computed in Eq.(85) as a weighted sum of the velocity components at neighboring nodes. If $(u_{x,N}, u_{y,N})$ the velocity components at node N one has

$$\begin{cases} u_{x,\text{interp}} = \displaystyle\sum_k (w_k^{(1)} \cdot u_{x,N}), \\ u_{y,\text{interp}} = \displaystyle\sum_k (w_k^{(1)} \cdot u_{y,N}). \end{cases} \tag{85}$$

A.4 Implementation of the geometries

The validation phase required additional specificities.

First of all, a function `type_Ruiz5(rho_w)` was created in the file `param_cylinder.py` to output the geometric and physical characteristics of the trunks used in the experiment (density, volume, length, diameter). Next, the channel configuration was created in the `definitions_functions.py` file as a `wall_obstacle_RUIZ_geomN` function (where `N` is replaced by the number of the desired geometry). Finally, the trajectory graphs presented in this section superimposes the trajectory graphs calculated by the code and the velocity profile representation.

Finally, the main difference with previous simulations is the way flow velocity is selected. Indeed, in view of the subdivision method, it is necessary to have as input data the flow velocity at the center of mass of each of the cylinder's sub-parts. As the domain has been discretized, the velocity field is finite. So a function `bilinear_interpolation_velocity` was created to bilinearly interpolate the velocity field at the desired points, at each time step.

There were a few subtleties to put the previous facts into practice. In fact, the data provided for the flow was slightly offset. There is, in fact, a null-value frame around the velocity matrix provided. For this reason, particular care had to be taken to ensure that the data and the various reference points were perfectly superimposed, both when reading the data and when creating the geometry and plots. An effective test to verify proper superimposition is to disable collision detection and correction, and to place the cylinder within an obstacle (including edges). Indeed, in that position the flow velocity is zero. If the cylinder does not move, the test is passed.

B Collision simulations

The purpose of this appendix is to present the implementation of the obstacles and to extend the presentation of numerical collision simulations to other cases. There are no different conclusions, the corrections are applied 'in mirror' between 'right' or 'left' collisons, or 'up' or 'down'.

B.1 Obstacles and flume configurations implementation

A key point is the implementation of the channel configuration with its various obstacles. As mentioned in the description of the model, the code must be able to store obstacle positions in an efficient way, allowing simple use of the data. As a reminder, the collision model requires the use of coordinates for corners, sub-walls, and main walls.

For the main walls, the y-coordinate of the 2 main walls are stored in a 1D array `y_wall_updown[k]`, where `k=0` stores the bottom main wall and `k=1` the top main wall. For the sub-walls, a three-dimensional array has been adopted and implemented as `geom[n][i][j]`. Its first dimension `[n]` refers to the index of the obstacle and goes from 0 to `N_obstacle-1`, where `N_obstacle` is the total number of obstacles. Thereafter, the order in which the obstacles are numbered is of no importance. The second dimension `[i]` refers to the coordinate with `i=0,1`. `[0]` stands for y and `[1]` for x. The third dimension `[j]` is defined for `j=0,1`. `geom[n][0][0]` indicates the y-coordinate of the top sub-wall of the obstacle `n` and `geom[n][0][1]` the y-coordinate of the bottom sub-wall. Then, `geom[n][1][0]` gives the x-coordinate of the left-sub-wall and `geom[n][1][1]` of the right sub-wall. Finally, a function `wall_obstacle` is created. It does not take anything as input, and has `geom`, `y_wall_updown` and `N_obstacle` as output. Fig.(39) shows some examples of the channel and obstacle created. Seven different pre-encoded configurations lie in the `IC_config.py` file, distinguished by letter A to G as `wall_configurationA` until `wall_configurationG`. More specifically, the function that allows the discretization according to the desired parameters (e.g. sizes, number of sub-parts) is the function code in the configuration `wall_configurationD` (one circle) and `wall_configurationE` (two circles).

B.2 Supplement to section 4.3.1

The section presented before vertical collisions with the *top main wall*. In the following, collisions with the *bottom main wall* will be presented. First of all, the simulation parameters are kept the same as in Tab.(14) with the exception of the flow velocity, which is set at $\mathbf{u} = (2, -1)$. The cylinder's trajectory is reported in Fig.(80) shows that the model is able to detect and physically correct the collisions (first of them at 3.4[m]).

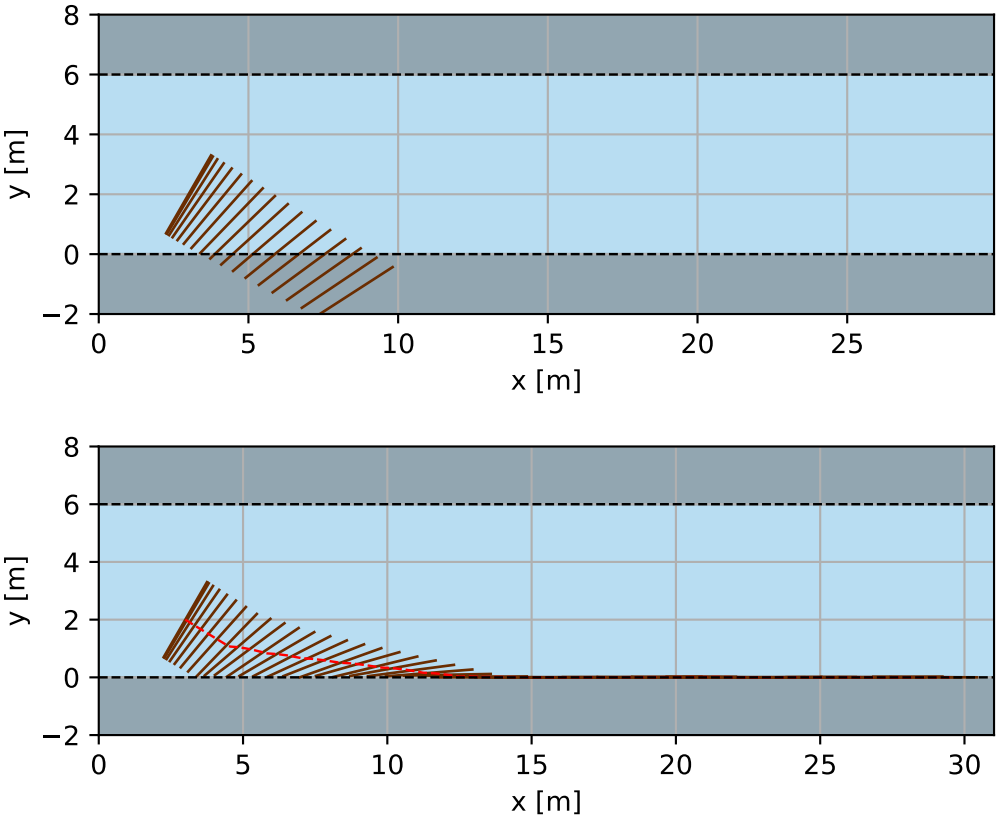

Figure 80: Trajectory of floating cylinder in horizontal plane (x, y), without (resp. with) collision model on the top (resp. bottom) figure. Vertical collisions with a bottom main wall appears to have been detected and corrected. The red dotted line is the trajectory of the center of mass, while the cylinder is represented by the brown straight lines.

The linear velocity is plotted in Fig.(41), the angular velocity on Fig.(42) and the angle inclination of the cylinder in Fig.(83).

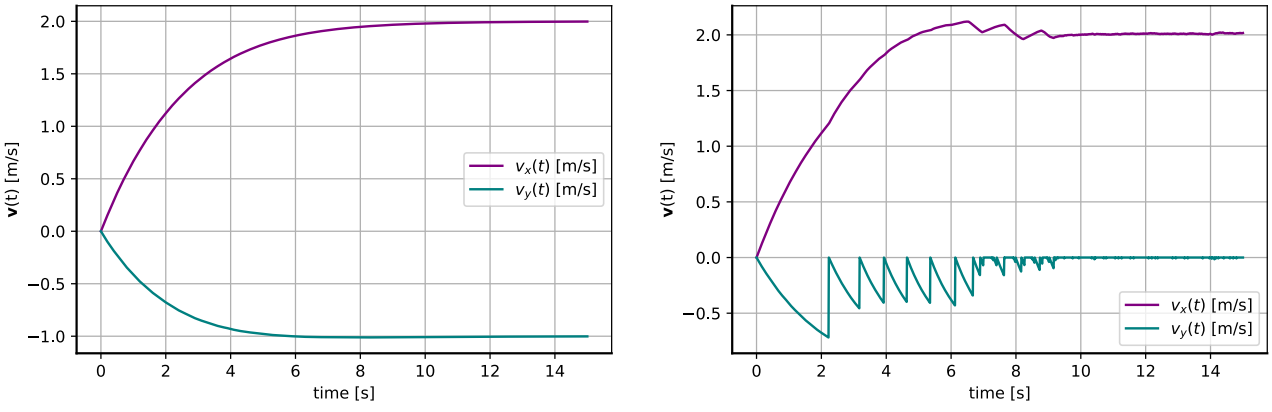

Figure 81: Linear velocity of cylinder as a function of time, without (resp. with) collision model on the top (resp. bottom) figure. Vertical collisions with a bottom main wall appears to have been detected and corrected (first collision at 2.2[s]).

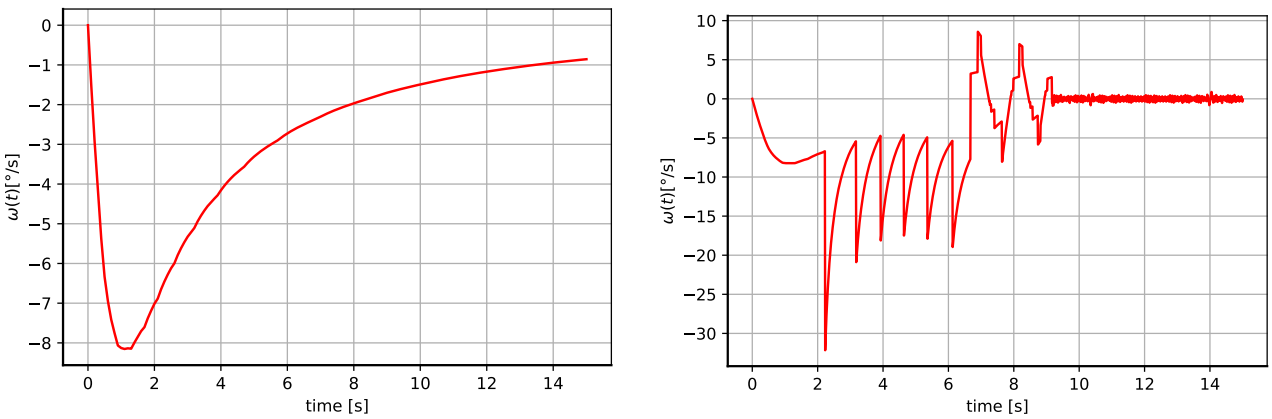

Figure 82: Angular velocity of cylinder as a function of time, without (resp. with) collision model on the top (resp. bottom) figure. Vertical collisions with a bottom main wall appears to have been detected and corrected (first collision at 2.2[s]).

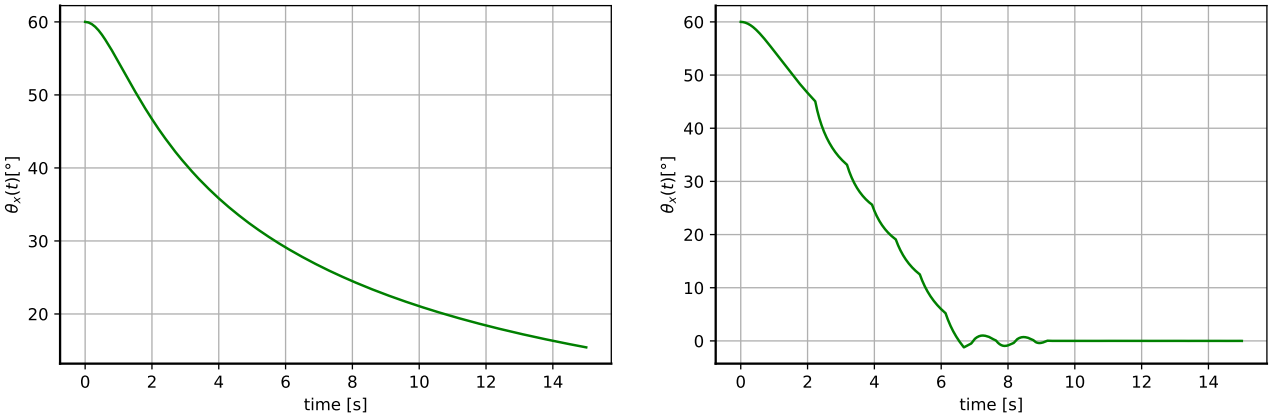

Figure 83: Angle of cylinder inclination to horizontal as a function of time, without (resp. with) collision model on the top (resp. bottom) figure. Vertical collisions with a bottom main wall appears to have been detected and corrected (first collision at 2.2[s]). After a while, the cylinder is aligned with the horizontal wall.

B.3 Supplement to section 4.3.1

In addition, this appendix shows the results for the case of vertical collision with a top sub-wall. The parameters of the sub-subsection 4.3.1 remains the same, except the initial position of center of mass of the cylinder (placed at (3,7.5)[m]) and the position of the obstacle (same size, but Corner down right placed at (4,5.5)[m]) The collision model produces the trajectory shown in Fig.(84). Same observation as for the *top* cas can be made.

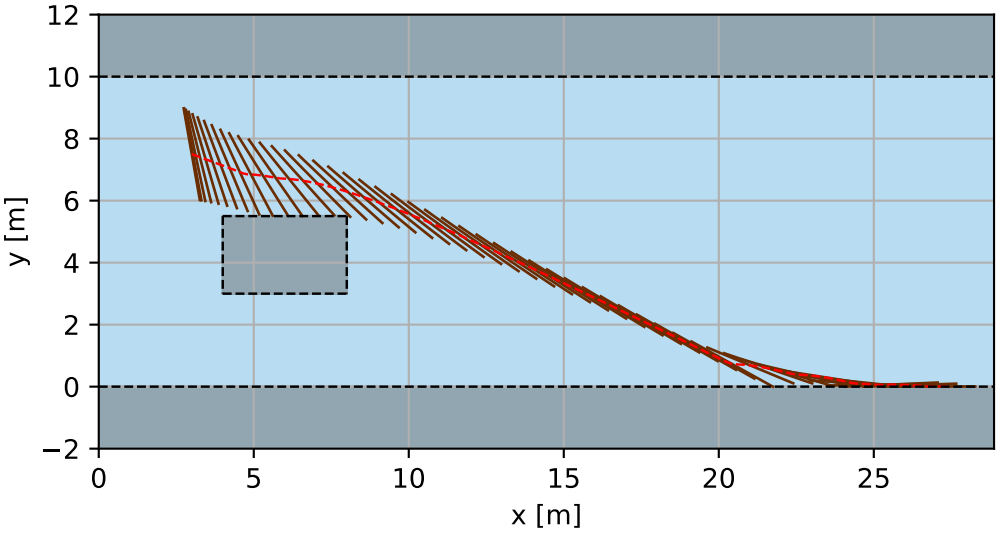

Figure 84: Trajectory of floating cylinder in horizontal plane (x, y), without (resp. with) collision model on the top (resp. bottom) figure. Vertical collisions with a top sub wall appears to have been detected and corrected. The red dotted line is the trajectory of the center of mass, while the cylinder is represented by the brown straight segments.

In view of the discussion of the main wall and the trajectory above, the interpretation of the graphs in Figs.(85, 86) is obvious. For each of the graphs, collisions with the obstacle are between 2.6 and 3.4[s] and collisions with the main wall after 11.4[s]. Between the two collision intervals, the cylinder reverts to the classic behavior studied for translation and rotation in the previous sections.

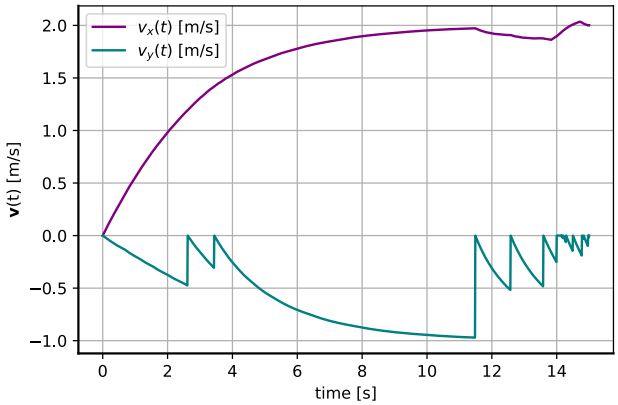

Figure 85: Linear velocity of cylinder as a function of time. Vertical collisions with a top sub-wall appears to have been detected and corrected (first collision at 2.6[s]).

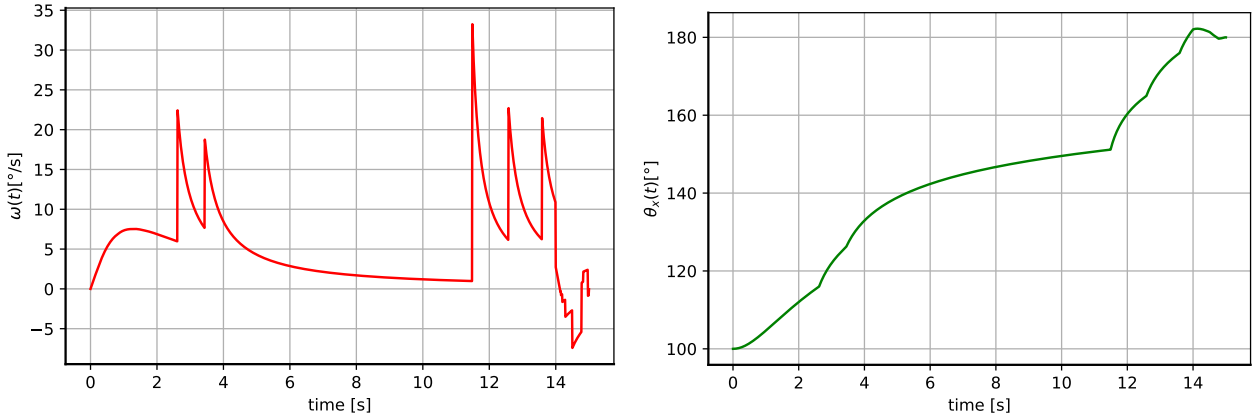

Figure 86: Angular velocity (on the left) and Angle of inclination to horizontal (on the right) of cylinder as a function of time. Vertical collisions with a top sub-wall appears to have been detected and corrected (first collision at 2.6[s]).

B.4 Supplement to section 4.3.3

To complement the section on corner collision results, an example of a down-right collision will be shown. First of all, the simulation parameters are presented in Tab.(25).

flow $[m/s]$	$\mathbf{v_0}$ $[m/s]$	ω_0 $[deg/s]$	θ_{u-v} $[deg]$	(x_0, y_0) $[m]$	ϵ $[-]$	N $[-]$	h $[s]$	t_{phys} $[s]$
constant stationnary $\mathbf{u} = (-\mathbf{2}, \mathbf{0})$	(0,0)	0	70	(16,5)	0.1	1	0.01	8.5

Table 25: Parameters used for the the simulation of Corner down right collisions.

The trajectory calculated for this situation is shown in Fig(87).

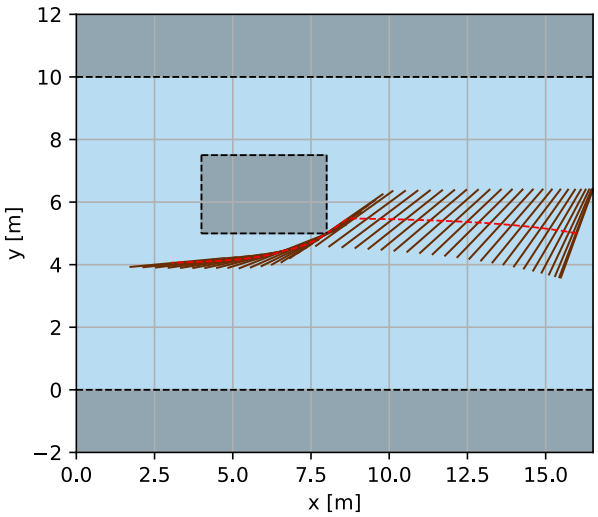

Figure 87: Trajectory of floating cylinder in horizontal plane (x, y). Corner down right collisions appear to have been detected and corrected. The red dotted line is the trajectory of the center of mass, while the cylinder is represented by the brown straight segments.

The interpretation of the graphs in Figs.(88, 89) is here again the same as in the section about corner collisions.

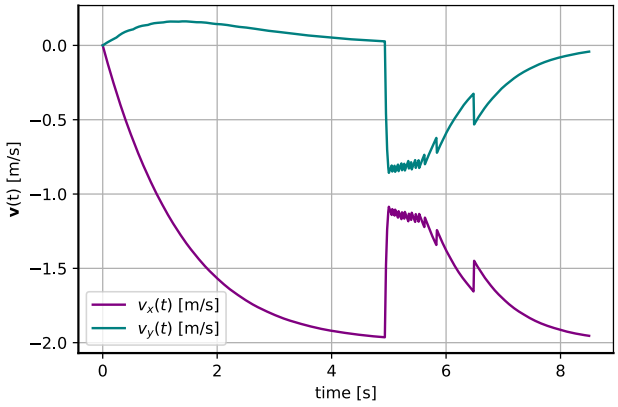

Figure 88: Linear velocity of cylinder as a function of time. Corner down right collisions appear to have been detected and corrected (first collision at 4.94[s]).

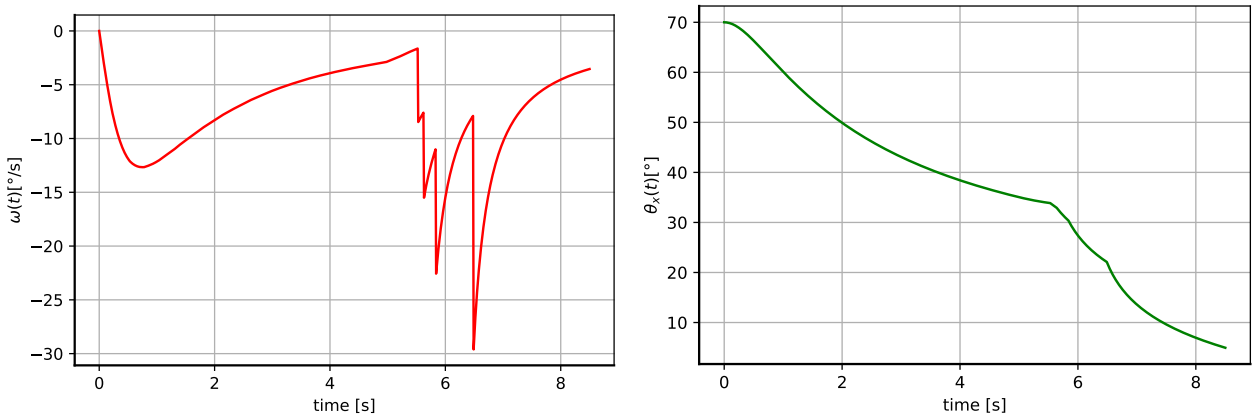

Figure 89: Angular velocity and angle of inclination to horizontal of cylinder as a function of time. Corner down right collisions appear to have been detected and corrected (first collision at 4.94[s]).

References

G. Batchelor. *An introduction to fluid dynamics*. Cambridge University Press, Cambridge, UK, 1967.

D. Bocchiola, M. C. Rulli, and R. Rosso. Flume experiments on wood entrainment in rivers. *Adv. Water Resour.*, 29(8):1182–1195, Aug. 2006.

G. E. Braudrick, Christian A.; Grant. When do logs move in rivers? *Water Resources Research*, 36(2): 571–583, Feb. 2000.

B. Dewals, P. Archambeau, S. Erpicum, and M. Pirotton. Flood risk in liege area: A transnational perspective. *Hydrolink*, pages 87–89, 2015.

A. J. Dorgan and E. Loth. Efficient calculation of the history force at finite reynolds numbers. *Int. J. Multiph. Flow*, 33(8):833–848, Aug. 2007.

H. Ghaffarian, D. Lopez, E. Mignot, H. Piegay, and N. Riviere. Dynamics of floating objects at high particulate reynolds numbers. *Phys. Rev. Fluids*, 5(5), May 2020.

H. Haga, T. Kumagai, K. Otsuki, and S. Ogawa. Transport and retention of coarse woody debris in mountain streams: An in situ field experiment of log transport and a field survey of coarse woody debris distribution. *Water Resour. Res.*, 38(8):1–1–1–16, Aug. 2002.

C. Hecker. Collision response. *Part 3 : Game Developer Magazine*, page 11–18, 1997.

J. Journée and W. Massie. *Offshore Hydromechanics*. Delf University of Technology, jan 2001.

E. A. Keller and F. J. Swanson. Effects of large organic material on channel form and fluvial processes. *Earth Surf. Process.*, 4(4):361–380, Oct. 1979.

Z. W. Kundzewicz, N. Lugeri, R. Dankers, Y. Hirabayashi, P. Döll, I. Pińskwar, T. Dysarz, S. Hochrainer, and P. Matczak. Assessing river flood risk and adaptation in europe— review of projections for the future. *Mitig. Adapt. Strateg. Glob. Chang.*, 15(7):641–656, Oct. 2010.

F. Macchione and M. Lombardo. Roughness-based method for simulating hydraulic consequences of both woody debris clogging and breakage at bridges in basin-scale flood modeling. *Water Resour. Res.*, 57(12), Dec. 2021.

J. Magnaudet and I. Eames. The motion of high-reynolds-number bubbles in inhomogeneous flows. *Annu. Rev. Fluid Mech.*, 32(659):659–708, 2000.

M. Mandø and L. Rosendahl. On the motion of non-spherical particles at high reynolds number. *Powder Technol.*, 202(1-3):1–13, Aug. 2010.

E. K. Marchildon, A. Clamen, and W. H. Gauvin. Drag and oscillatory motion of freely falling cylindrical particles. *Can. J. Chem. Eng.*, 42(4):178–182, Aug. 1964.

R. Mei and R. J. Adrian. Flow past a sphere with an oscillation in the free-stream velocity and unsteady drag at finite reynolds number. *J. Fluid Mech.*, 237(-1):323–341, Apr. 1992.

E. E. Michaelides. A novel way of computing the basset term in unsteady multiphase flow computations. *Phys. Fluids*, 4(7):1579–1582, July 1992.

M. Parmar, A. Haselbacher, and S. Balachandar. Generalized Basset-Boussinesq-Oseen equation for unsteady forces on a sphere in a compressible flow. *Phys. Rev. Lett.*, 106(8):084501, Feb. 2011.

E. Persi. *Eulerian–Lagrangian modelling of large floating debris transport during floods*. PhD thesis, University of London, 2015.

E. Persi, G. Petaccia, and S. Sibilla. Large wood transport modelling by a coupled Eulerian–Lagrangian approach. *Nat. Hazards (Dordr.)*, Apr. 2017.

E. Persi, G. Petaccia, S. Sibilla, P. Brufau, and J. I. García-Palacin. Experimental dataset and numerical simulation of floating bodies transport in open-channel flow. *J. Hydroinformatics*, 22 (5):1161–1181, Sept. 2020.

Rayleigh. On the resistance of fluids. *Lond. Edinb. Dublin Philos. Mag. J. Sci.*, 2(13):430–441, Dec. 1876.

L. Rosendahl. Using a multi-parameter particle shape description to predict the motion of non-spherical particle shapes in swirling flow. *Appl. Math. Model.*, 24(1):11–25, Jan. 2000a.

L. Rosendahl. Using a multi-parameter particle shape description to predict the motion of non-spherical particle shapes in swirling flow. *Appl. Math. Model.*, 24(1):11–25, Jan. 2000b.

V. Ruiz-Villanueva, E. Bladé, M. Sánchez-Juny, B. Marti-Cardona, A. Díez-Herrero, and J. M. Bodoque. Two-dimensional numerical modeling of wood transport. *J. hydroinformatics*, 16 (5):1077–1096, Sept. 2014.

R. Saucier. *Resolving the orientation of cylinders and cuboids from projected area measurements*. ARL-TN. US Army Research Laboratory, 2016.

S. Shyamcharan. *Forces on bodies in an oscillatory flow*. PhD thesis, University of London, 1979.

S. P. Singh and S. Mittal. Flow past a cylinder: shear layer instability and drag crisis. *Int. J. Numer. Methods Fluids*, 47(1):75–98, Jan. 2005.

S. L. Soo. *Multiphase Fluid Dynamics*. Avebury Technical, London, England, Sept. 1990.

World Meteorological Organization (WMO). Climate and water - floods, 2023. URL https://public.wmo.int/en/resources/world-meteorological-day/previous-world-meteorological-days/climate-and-water/floods. Accessed: 07/21/2023.

C. Yin, L. Rosendahl, S. Knudsen Kær, and H. Sørensen. Modelling the motion of cylindrical particles in a nonuniform flow. *Chem. Eng. Sci.*, 58(15):3489–3498, Aug. 2003.